JOINT TRANSPORTATION
RESEARCH PROGRAM
INDIANA DEPARTMENT OF TRANSPORTATION
AND PURDUE UNIVERSITY

Shear and Bearing Capacity of Corroded Steel Beam Bridges and the Effects on Load Rating

Deven Kanakamedala, Jungil Seo, Amit H. Varma, Robert J. Connor, Anna Tarasova

SPR-4527 • Report Number: FHWA/IN/JTRP-2023/11 • DOI: 10.5703/1288284317634

RECOMMENDED CITATION

Kanakamedala, D., Seo, J., Varma, A. H., Connor, R. J., & Tarasova, A. (2023). *Shear and bearing capacity of corroded steel beam bridges and the effects on load rating* (Joint Transportation Research Program Publication No. FHWA/IN/JTRP-2023/11). West Lafayette, IN: Purdue University. https://doi.org/10.5703/1288284317634

AUTHORS

Deven Kanakamedala
Graduate Research Assistant
Lyles School of Engineering
Purdue University
(781) 277-1211
dkanakam@purdue.edu
Corresponding Author

Jungil Seo
Senior Principal Research Scientist
Lyles School of Civil Engineering
Purdue University

Amit H. Varma, PhD
Karl H. Kettelhut Professor of Civil Engineering
Director of Bowen Laboratory of Large-Scale CE Research
Lyles School of Civil Engineering
Purdue University

Robert J. Connor, PhD
Jack and Kay Hockema Professor in Civil Engineering
Director of CAI and S-BRITE
Lyles School of Civil Engineering
Purdue University

Anna Tarasova
Graduate Research Assistant
Lyles School of Engineering
Purdue University

JOINT TRANSPORTATION RESEARCH PROGRAM

The Joint Transportation Research Program serves as a vehicle for INDOT collaboration with higher education institutions and industry in Indiana to facilitate innovation that results in continuous improvement in the planning, design, construction, operation, management and economic efficiency of the Indiana transportation infrastructure. https://engineering.purdue.edu/JTRP/index_html

Published reports of the Joint Transportation Research Program are available at http://docs.lib.purdue.edu/jtrp/.

NOTICE

TECHNICAL REPORT DOCUMENTATION PAGE

1. Report No. FHWA/IN/JTRP-2023/11	**2. Government Accession No.**	**3. Recipient's Catalog No.**
4. Title and Subtitle Shear and Bearing Capacity of Corroded Steel Beam Bridges and the Effects on Load Rating		**5. Report Date** April 2023 **6. Performing Organization Code**
7. Author(s) Deven Kanakamedala, Jungil Seo, Amit H. Varma, Robert J. Connor, and Anna Tarasova		**8. Performing Organization Report No.** FHWA/IN/JTRP-2023/11
9. Performing Organization Name and Address Joint Transportation Research Program Hall for Discovery and Learning Research (DLR), Suite 204 207 S. Martin Jischke Drive West Lafayette, IN 47907		**10. Work Unit No.** **11. Contract or Grant No.** SPR-4527
12. Sponsoring Agency Name and Address Indiana Department of Transportation (SPR) State Office Building 100 North Senate Avenue Indianapolis, IN 46204		**13. Type of Report and Period Covered** Final Report **14. Sponsoring Agency Code**

15. Supplementary Notes

Conducted in cooperation with the U.S. Department of Transportation, Federal Highway Administration.

16. Abstract

Corrosion in the girders of steel girder bridges often occurs due to the deicing salts, water, and other debris that leak through the deck joints into the web and bottom flange at the girder ends. Corrosion causes loss of cross-sectional area leading to a reduction in section properties of the member, which eventually results in a reduction in structural resistance against shear and bearing. In this study, seven full-scale tests were performed on decommissioned steel girders acquired from bridges scheduled for demolition in Indiana. Two of the four girders had severe corrosion with cracks and holes in the bottom of the web induced by corrosion, while four girders had moderate section loss induced artificially. All seven girders were subjected to shear loading to determine the residual shear and bearing capacity. Test results revealed a reduction in strength due to section loss compared to nominal sections. Failure modes observed during these four large-scale experiments were shear buckling, shear rupture, and web local crippling. Finite element models were developed and benchmarked to the experimental results. Parametric studies were performed for unstiffened and stiffened girders and included different corrosion scenarios by varying parameters such as corrosion height, length, and thickness loss. Results were analyzed to investigate the effect of each parameter and a modification factor was developed to estimate the residual shear and bearing capacity of corroded girders.

17. Key Words steel girders, corrosion, section loss, shear buckling, shear capacity, web local crippling, parametric study, modification factor	**18. Distribution Statement** No restrictions. This document is available through the National Technical Information Service, Springfield, VA 22161.

19. Security Classif. (of this report) Unclassified	**20. Security Classif. (of this page)** Unclassified	**21. No. of Pages** 81 including appendices	**22. Price**

Form DOT F 1700.7 (8-72) Reproduction of completed page authorized

EXECUTIVE SUMMARY

Introduction

Corrosion in steel girders causes loss of cross-sectional area and leads to a reduction in the section properties of the member, which eventually results in a reduction in structural resistance against shear and bearing. This project investigated the effects of the section loss on the residual shear and bearing capacity of the corroded steel girders. Naturally, corroded girders were identified and procured from the North-Split Reconstruction Project in Indiana for this study. Seven full-scale experiments were performed, and the developed numerical models were benchmarked to the experimental results. In addition, two parametric studies were conducted on a $W24 \times 68$ section using the benchmarked numerical modeling approach to include different corrosion scenarios and predict corresponding residual shear and bearing capacity. Finally, results from the parametric studies were utilized to develop reduction factors to estimate the residual shear and bearing capacities.

Findings

Seven full-scale experiments were performed on the steel girders with section loss subjecting them to shear loading. Four out of the seven specimens were stiffened girders with full-depth stiffeners at the bearing and loading region, while the remaining three were unstiffened girders. In addition, all the specimens except Specimen 5 had a pair of partial depth transverse stiffeners. During the service life, these partial depth transverse stiffeners were used to connect the diaphragm to the girder, and they were retained during the experiment except for Specimen 5. From the experiments it was found that web local crippling is the governing failure mode for unstiffened corroded girders. Moreover, partial depth transverse stiffeners contributed to the web local crippling strength.

Two failure modes were observed from the experiments performed on the stiffened girders—shear web buckling and shear rupture. Shear rupturing was initiated at the bottom of the web at one of the cracks in the corroded region and was then extended longitudinally along the web bottom. Based on this observation, it is recommended to arrest the cracks in the corroded region of a stiffened steel girder.

The parametric study found that thickness loss in the web and the length of the corroded region has a strong influence on the residual bearing capacity of an unstiffened corroded girder, but the height of the corroded region does not have a strong influence on the residual bearing capacity of an unstiffened corroded girder. However, for a stiffened girder, the corroded region's height, thickness loss in the web, and the length of the corroded region have a strong influence on the residual shear capacity.

Implementation

The proposed reduction factors provide a method to estimate the residual bearing capacity of the unstiffened steel girders and the residual shear capacity of the stiffened steel girders. Incorporating these residual capacities calculated by the proposed reduction factors will result in more accurate load ratings. For immediate incorporation of this study into AASHTOWare BrR software for load rating purposes, an available alternative approach is briefly described at the end of this study.

CONTENTS

LIST OF TABLES

LIST OF FIGURES

1. INTRODUCTION

According to the ASCE *2021 Report Card for America's Infrastructure* (ASCE, 2021), the estimated total number of bridges in the United States is about 617,000, and 7.5% of those bridges are considered structurally deficient as per a recent estimate. Structural deficiency is often caused by the deterioration of steel beams due to corrosion, especially in steel beam bridges. Corrosion of steel girders on bridges often occurs due to the deicing salts, water, and other debris that leak through the deck joints onto the web and bottom flange at the girder ends. Corrosion causes loss of cross-sectional area leading to a reduction in section properties of the member which eventually results in a reduction in structural resistance against bearing and shear.

In this study, seven full-scale tests were performed on decommissioned steel girders acquired from bridges scheduled for demolition in the state of Indiana. Failure modes observed included shear web buckling, web local crippling, flexural yielding, and shear rupture, with the most drastic reduction in strength occurring in unstiffened corroded girders that failed in web local crippling. A parametric study with over 10,000 numerical models was completed to analyze the influence of various corrosion pattern parameters on the residual capacity of the corroded girders. Finally, two modification factors were developed to estimate the residual web local crippling capacity of an unstiffened corroded girder and the residual shear capacity of a stiffened corroded girder.

One of the first studies in the US of the effect of corrosion on the residual capacity and reliability of steel bridges was conducted in the University of Michigan in 1988. Kayser (1988) in his study discovered that the environment in which the bridge is located drastically influenced its performance, with the marine environment having the largest (up to 100%) reduction in safety index. Plate theory was used to evaluate the effect of corrosion on flexural, shear and bearing capacities, with the bearing and shear failures usually governing due to the thin web. The stiffeners could help significantly improve the bearing capacity of the girder and have the biggest impact on short span bridges, because they were usually built using members with thinner webs. Capacity curves were developed for W24 × 76, W30 × 116, W36 × 182, W36 × 230 girders with and without stiffeners showing both linear and nonlinear correlation between the surface loss and the residual capacity. In this study, a corrosion damage model was formulated by incorporating information about form of corrosion and rate of corrosion in various environments. On top of that, theories of reliability and structural analysis were implemented in this model to estimate the residual load-carrying capacity and safety of the structure.

Kayser and Nowak (1989) discussed the capacity loss due to corrosion in steel girder bridges. In this study the correlation between residual moment capacity and flange loss was developed for composite and non-composite sections. Similar curves were developed for shear and bearing capacities. Bearing capacity has a linear correlation with surface loss for girders with stiffeners and nonlinear for unstiffened girders. However, correlation between shear capacity and surface loss is always nonlinear regardless the presence of stiffeners. One of the conclusions that was made in this study is that the stiffened girders are more tolerable towards section loss due to corrosion. The bearing failure governs in the thinner webs (short span bridges), therefore bearing stiffeners will provide a higher corrosion tolerance for the structure.

In Sugimoto et al. (2006) corroded riveted railway steel girders were studied by conducting experiments in the laboratory and nonlinear numerical analysis in Abaqus to determine the correlation between residual capacity and the remained plate thickness. The whole demolished bridge was used for bending strength testing and upper flange's residual thickness was measured using laser displacement sensor. In railway bridges the upper flange is more prone to corrosion with the largest amount of corrosion located at sleeper locations. During the experimental testing girder no. 1 (G1) failed in upper flange local buckling, at the location with the lowest residual thickness, whereas the girder no. 2 (G2) undergone bottom flange yielding first. The experimental testing was followed by the numerical analysis and curve representing the relationship between bending strength ratio and minimum section ratio was developed. The curve turned out to have 45-degree slope. To investigate the effect of corrosion on residual shear capacity, six girders were evaluated, five of them had artificially induced corrosion by grinding and spraying salts (accelerated corrosion) and one girder did not have any section loss at all. The experimental investigation was again followed by FE analysis resulting in the curve representing the relationship between shear strength ratio and average plate thickness ratio. The proposed method of evaluating the remaining bending strength included measuring the minimum plate thickness at the midspan; for the shear capacity evaluation it was proposed to measure the average plate thickness near the support. Once the section loss is determined, the developed curves could be used to evaluate the residual flexural and shear capacities.

Rahgozar (2009) developed minimum curves to predict the residual capacity of corroded steel girders for various levels of deterioration. The thicknesses of four girders (305 × 165 UB 40 kg) were thoroughly measured to evaluate the severity of the section loss due to corrosion, with the highest thickness loss in the flange being approximately 40% (Beam 3). The four girders were delivered from the chemical plant ICI Ltd that was being demolished and spillage of the chemicals was one of the main reasons for corrosion. In this study the minimum curves for shear capacity were developed for the two categories (C1 and C2) based on the

slenderness ratio and they are given Equation 1.1 and Equation 1.2.

$$\text{Category 1 (C1): } \frac{d}{t} \leq 63\varepsilon = 63\sqrt{275/P_y} \quad \text{(Eq. 1.1)}$$

$$\text{Category 2 (C2): } \frac{d}{t} > 63\varepsilon = 63\sqrt{275/P_y} \quad \text{(Eq. 1.2)}$$

Where,
P_y = design strength, MPa.
d = depth of the web, mm.
t = thickness of the web, mm.

British standard BS 5950 was used for the development of the minimum curves for the residual shear capacity. Theoretical calculations were later followed by experimental testing of four deteriorated girders, which showed the effectiveness of the minimum curve, even though the approximation using these curves is conservative. There were three major research projects in the United States over the last 5 years that were studying deterioration of the steel girders due to corrosion and its effect on the residual shear and bearing capacity.

Tzortzinis et al. (2019) analyzed 216 bridge inspection reports that contained 808 beam ends to categorize typical corrosion patterns for unstiffened steel beams. As a result, eighteen patterns were finalized for beams with and without diaphragms, with the strong influence of diaphragm presence on the corrosion pattern. Tzortzinis (2021) and Tzortzinis et al. (2021a, 2021b) conducted a study, where six naturally corroded beams were tested in the laboratory, because no previous research considered naturally corroded beams specifically. By comparing the capacity predictions calculated following the Mass-DOT *2019 Bridge Manual* and the test results, it was noted that in some cases the manual underestimated the actual capacity and, in some cases, overestimated it. On top of that, initial lateral imperfection severely affects the capacity of the beam, and current procedures described in the manual do not account for it. Once finite element models were validated with the experimental data, more than 2,000 models were analyzed during the phase of the parametric study. One of the most important findings was that the size of the hole in the web has almost no effect on the bearing capacity if the hole is located just above the bearing. Finally, equations for calculating the bearing capacity of the deteriorated girders were developed (Gerasimidis et al., 2021). They considered various imperfections (0.1 tw, 0.5 tw, 1 tw) as well as the N/d ratio, where N—bearing length and d—depth of the beam. Those equations consider web buckling as well as web crippling as potential failure modes. The formula (Equation 1.3) for the calculation of the remaining average thickness of the web is provided below which shows that initial imperfections and bearing length affect the average thickness calculation of the web containing holes.

$$t_{ave} = \frac{(N + md - H)}{(N + md)} t_w \quad \text{(Eq. 1.3)}$$

Where,
N = bearing length, in.
d = beam depth, in.
H = length of the longest hole in web, in.
t_w = remaining web thickness.
m = factor depending on initial imperfection and bearing length.

Javier et al. (2021a, 2021b) conducted seventeen full-scale flexural tests on unstiffened hot-rolled steel beams that were delivered to the laboratory from decommissioned bridges in Virginia. Shear failure was purposefully induced close to the bearing region, and strain, displacement, and load were measured throughout testing. The strain was recorded using a digital image correlation system (DIC), displacement using string potentiometers, and the load was determined using a pressure transducer. The results obtained during testing were later compared with the calculations for shear capacity using equations from the following documents: AISC 360-16, AASHTO LRFD (AISC, 2016) as well as equations derived by other researchers from the literature review. On top of that, it proved that AASHTO-Ware Bridge Rating (BrR) can determine the residual capacity of a corroded beam relatively accurately when the remaining web thickness is calculated accounting for section loss.

The flowchart for determining the shear capacity was developed for cases with and without holes in the web due to corrosion. For the cases of the webs with holes, the reduction factor presented in MassDOT *LRFD Bridge Manual* 2020, Part I, Section 7.2.9.2 was implemented. The formula Equation 1.4) for the calculation of the remaining thickness of the web with holes is provided below.

$$t_{w,holes} = \frac{(N + 5k - H)}{(N + 5k)} t_{w,3in} \quad \text{(Eq. 1.4)}$$

Where,
N = bearing length, in.
k = distance from flange to web toe fillet, in.
H = length of the longest hole in web, in.
$t_{w,\ 3\ in}$ = remaining average web thickness.
$t_{w,\ holes}$ = modified web thickness to account for holes in the web.

Tzortzinis et al. (2022) post-processed inspection reports provided by MassDOT that contained 210 corroded stiffened beam ends. Based on that examination, two groups of girders were identified: girders with two and only one stiffener at the bearing area, and corrosion patterns were provided in every configuration. In this study, the deterioration of stiffeners due to corrosion was also considered. Two specimens were experimentally tested with a 3D laser scan taken for every specimen prior to testing to obtain point cloud data. Point cloud data was later post-processed using MATLAB script to obtain a contour map for the corroded region. Both specimens failed due to large lateral displacements of the web and the experiments were terminated. After the experimental part of the

project, a parametric study was also conducted. Three different corrosion patterns were considered during the parametric study that contained 1,000 high-fidelity finite element models where the deterioration of the bearing stiffener (30%, 50%, and 70% of stiffener section loss) was also accounted for. As a result of the study, it was found that section loss of the stiffener has a detrimental effect on the bearing capacity of the beam and therefore should be inspected and documented more carefully. A set of equations (Equation 1.5–Equation 1.7) was proposed to calculate the residual capacity of the beams that were in good correlation with the parametric study results. Overall, current procedures were found to overestimate the capacity of corroded stiffened girders. It was found that if the corroded area is greater than the bearing length plus 10% of the web depth, then it does not decrease the bearing capacity any further.

$$R_n = aF_yA_{stif} + b(F_yA_{web})^c \qquad \text{(Eq. 1.5)}$$

Where,

$$A_{web} = t_w(N + 0.1d) - \sum Web\ hole\ areas \qquad \text{(Eq. 1.6)}$$

$$A_{stiff} = 2t_{stif}b_s - \sum Stiffener\ hole\ areas \qquad \text{(Eq. 1.7)}$$

a, b, c = new constants.
N = bearing length (in).
d = beam depth (in).
t_{web} = remaining web thickness within the 4-bottom in.
t_{stif} = remaining stiffener thickness within the 4-bottom in.

In AISC 360-16 (2016) equations for calculating shear and bearing capacity for non-corroded I-shaped members (Section G2.1) could be found. Equation 8.1 is used to calculate the shear capacity without considering tension field action (TFA). When TFA needs to be taken into consideration, Section G2.2 must be used. It is important to mention, that the equation was developed to calculate the capacity of the section without any section loss due to corrosion. Therefore, it cannot be used to predict the capacity of the corroded girder.

$$V_n = 0.6F_yA_wC_{v1} \qquad \text{(Eq. 1.8)}$$

Where,
F_y = specified minimum yield stress of the type of steel being used, ksi.
A_w = area of web, the overall depth times the web thickness, in^2.
C_{v1} = the web shear strength coefficient.

In most cases, $C_{v1} = 1$ for hot-rolled W shapes with a few exceptions that could be found in Section G2 as well as detailed guidelines on how to calculate web shear strength coefficient otherwise. To calculate the bearing capacity such limit states as web local crippling (Section J10.3) and web local yielding (Section J10.2) should be considered. For web local yielding, the nominal strength will depend on the location of the applied compressive force—greater than the full nominal depth of the member (Equation 1.9), or less or equal (Equation 1.10). Those equations are located in Section J10 of the steel manual.

$$R_n = F_{yw}t_w(5k + l_b) \qquad \text{(Eq. 1.9)}$$

$$R_n = F_{yw}t_w(2.5k + l_b) \qquad \text{(Eq. 1.10)}$$

Where,
F_{yw} = specified minimum yield stress of the web material, ksi.
k = distance from outer face of the flange to the web toe of the fillet, in.
l_b = length of bearing (not less than k for end beam reactions), in.
t_w = thickness of web, in.

The applicable equation for web local crippling capacity will depend on the distance from the girder end at which compressive load is applied, as well as the ratio of the bearing length over full nominal depth of the member. For example, if the compressive load is applied at a distance greater or equal than half of the nominal depth of the member, the Equation 1.11 will be used. To conclude, AISC 360-16 equations have limited applicability and could be used only to accurately predict shear and bearing capacity of girders without any section loss.

$$R_n = 0.8t_w^2\left[1 + 3\left(\frac{l_b}{d}\right)\left(\frac{t_w}{t_f}\right)^{1.5}\right]\sqrt{EF_{yw}t_f/t_wQ_f} \qquad \text{(Eq. 1.11)}$$

Where,
d = full nominal depth of the member, in.
Q_f = 1.0 for wide-flange sections.
t_w = thickness of flange, in.

AASHTO *LRFD Bridge Design Specifications* (AASHTO, 2020) contains similar equations to AISC 360-16 (2016) with a slightly different notations and is mostly used in transportation industry. Section 6.10.9 in. AASHTO LRFD contains all the necessary equations for shear resistance calculations. Equation 1.12 is used to calculate the shear capacity of the unstiffened webs without considering tension field action (TFA). It is important to mention, that the equation was developed to calculate the capacity of the section without any section loss due to corrosion. Therefore, it cannot be used to predict the capacity of the corroded girder.

$$V_n = 0.58CF_{yw}Dt_w \qquad \text{(Eq. 1.12)}$$

Where,
F_{yw} = specified minimum yield stress of the type of steel being used, ksi.
D = total web depth, in.

C = ratio of the shear-buckling resistance to the shear yield strength determined in Section 6.10.9.3.2 of AASHTO LRFD.
t_w = thickness of flange, in.

Section D6.5 is concerned with the concentrated loads applied to webs without bearing stiffeners. Therefore, to investigate the nominal resistance to concentrated load that is applied at the distance greater than the full nominal depth of the member Equation 1.13 should be used, with Equation 1.14 being applicable to every other case. The location of the compressive force is vital for calculation, since the load is assumed to be distributed at the 2.5 slope and if there is not enough space on both sides of the applied load, the resistance of the web to local yielding will be smaller (Equation 1.14).

$$R_n = (5k + N)F_{yw}t_w \qquad \text{(Eq. 1.13)}$$

$$R_n = (2.5k + N)F_{yw}t_w \qquad \text{(Eq. 1.14)}$$

Where,
F_{yw} = specified minimum yield stress of the web material, ksi.
k = distance from the outer face of the flange resisting the concentrated load or bearing reaction to the web toe of the fillet, in.
N = length of bearing, in. N shall be greater than or equal to k at end bearing locations.
t_w= thickness of web, in.

To prevent crippling of the web, or instability due to high compressive stresses additional checks must be done. The nominal resistance of the web to crippling will depend on the location of the load and on the ratio of the bearing length over full nominal depth of the member. For example, if the compressive load is applied at a distance greater or equal than half of the nominal depth of the member, Equation 1.15 shall be used. To conclude, AASHTO LRFD as well as AISC 360-16 equations have limited capability and could be used only to accurately predict shear and bearing capacity of girders without any section loss.

$$R_n = 0.8t_w^2\left[1 + 3\left(\frac{N}{d}\right)\left(\frac{t_w}{t_f}\right)^{1.5}\right]\sqrt{EF_{yw}t_f/t_w} \qquad \text{(Eq. 1.15)}$$

Where,
d = full nominal depth of the member, in.
t_w = thickness of flange, in.

2. IDENTIFICATION AND PROCUREMENT OF CORRODED BEAMS

This study focuses on investigating the effects of corrosion on the residual shear and bearing capacity of steel girders experimentally and numerically. The experimental investigation consists of studying the deterioration in the girders due to corrosion and performing full-scale tests to determine their residual capacity. The most important aspect of the investigation was the procurement of the naturally corroded girders, and this chapter describes the process of identification and procurement of the naturally corroded girders.

Bridge inspection reports of several bridges (presented in Table 2.1) were accessed through BIAS (Bridge Inspection Application System) of INDOT and reviewed to identify bridges with deteriorated steel girders due to corrosion. The North-Split Reconstruction Project consisted of 42 downtown Indianapolis bridges scheduled for either rehabilitation or replacement. Inspection reports of the 42 bridges were reviewed and shortlisted nine bridges for site inspection based on the condition rating of the superstructure and inspection photographs. In conjunction with a team from INDOT, the research team visited each of the nine bridges and selected two bridges that had deteriorated girders with varying degrees of corrosion. The remaining seven bridges have girders primarily deteriorated due to fatigue and fracture.

From the selected two bridges, 21 steel girders deteriorated due to corrosion were identified and marked with paint to distinguish them from the remaining beams, as shown in Figure 2.1. This would help the construction team to salvage these girders carefully and avoid damage during demolition.

After demolition, girders were stored on-site and inspected by the research team for any damage (Figure 2.2 through Figure 2.5). While most of the girders were salvaged without any damage, four girders had damage that occurred either during concrete deck saw cutting or during concrete deck demolition Figure 2.5. The girders were then transported to Bowen Laboratory on a trailer. The first lot of 11 girders was received around October 11, 2021, while the second lot consisting of the remaining 10 girders was received on January 14, 2022 and stored at Bowen Laboratory, as shown in Figure 2.6 and Figure 2.7.

Section details of the 21 received girders and the level of corrosion are provided in Table 2.2. Out of the 21 received girders, 11 had severe corrosion, holes, and cracks in the web, and the remaining nine had light to moderate corrosion.

TABLE 2.1
Bridges selected for inspection

No.	Structure No.	Feature
1	I-65-112-05749 A	I-65 Ramp 3E-W over College Ave
2	I-70-083-02432 CEBL	I-70 EB and Ramp 3W-E over Lewis Street and Monon Trail
3	I-65-112-05742 BNB	I-65 NB over Abandoned Ramp
4	I-65-112-05748 ANB	I-65 NB over College Ave
5	I-65-112-05745 A	I-65 SB and Ramp 3W-E (to I-70 EB) over College Ave
6	I-65-111-05731 B	I-65, I-70, and CD over Vermont Street
7	I-65-111-05730 B	I-65, I-70, and CD over New York Street
8	I-65-111-02431 A	I-65/I-70 SB over CSX Railroad and Ohio Street
9	I-65-111-05725 A	I-65, I-70, and CD over Washington Street

TABLE 2.2
Details of the procured 21 corroded girders

No.	Beam Section	Beam Length	Corrosion Level (Visual Inspection)
1	W24 × 68	22 ft.	Light Corrosion
2	W24 × 68	22 ft.	Severe Corrosion, Holes, and Cracks
3	W24 × 68	22 ft.	Severe Corrosion, Holes, and Cracks
4	W24 × 68	22 ft.	Light Corrosion
5	W24 × 68	22 ft.	Light Corrosion
6	W24 × 68	22 ft.	Severe Corrosion, Holes, and Cracks
7	W24 × 68	22 ft.	Light Corrosion
8	W24 × 68	22 ft.	Light Corrosion
9	W24 × 68	22 ft.	Light Corrosion
10	W24 × 68	22 ft.	Light Corrosion
11	W24 × 68	22 ft.	Medium Corrosion with Holes
12	W24 × 68	22 ft.	Medium Corrosion
13	W24 × 68	22 ft.	Severe Corrosion, Holes, and Cracks
14	W24 × 68	22 ft.	Medium Corrosion with Holes
15	W24 × 68	22 ft.	Medium Corrosion
16	W24 × 68	22 ft.	Medium Corrosion with Cracks
17	W21 × 62	18 ft.	Severe
18	W21 × 62	18 ft.	Medium Corrosion with Holes
19	W21 × 62	18 ft.	Severe Corrosion with Holes
20	W21 × 62	18 ft.	Severe Corrosion with Holes
21	W36 × 135	22 ft.	Medium Corrosion

(a) (b)

Figure 2.1 Corroded girders identification and marking.

Figure 2.2 Concrete deck saw cutting (courtesy of HNTB).

Figure 2.3 Concrete deck demolition (courtesy of HNTB).

Figure 2.4 Girders temporarily stored on-site (courtesy of HNTB).

(a) (b)

Figure 2.5 Damage to corroded girders during demolition: (a) damage to the top flange during concrete deck saw cutting, and (b) damage to the entire top flange due to excavator during concrete deck breaking (courtesy of HNTB).

Figure 2.6 Corroded girders being stored at Thomas A. Page Pavilion at Purdue University.

Figure 2.7 Corroded girders being stored on the north side of the Bowen Laboratory at Purdue University.

3. SECTION LOSS MEASUREMENTS AND CORROSION PATTERN

This chapter describes the process involved in measuring and quantifying the section loss due to corrosion in the naturally corroded steel girders described in Chapter 2. This process was essential to understand the amount of section loss in the web and the topology of the corroded region. The remaining thickness of the web was measured using an ultrasonic thickness gauge. This chapter describes the methodology adopted and the challenges identified during the process. In addition, recommendations regarding the deduction of paint thickness from the thickness measurements were also presented in this chapter.

3.1 Section Loss Measurement Using Ultrasonic Thickness Gauge

Because of natural corrosion, steel girders salvaged from the decommissioned bridges had section loss, predominantly at the bottom of the web. Ultrasonic thickness gauge (T-Mike BTM manufactured by GE Inspection Technologies) was used to measure the remaining thickness of the web after section loss due to corrosion, consistent with the practice by bridge inspectors during field inspection to spot-check the residual thickness of steel girders. Ultrasonic thickness gauge measured the remaining thickness of the steel based on the time taken by the ultrasonic sound wave to travel from the side of the web, where ultrasound waves were generated to the opposite side and reflected the source.

This method of measurement of residual thickness faced two challenges. Firstly, it was observed that the presence of paint was affecting the measured thickness. This could be due to the variation in the speed of ultrasound waves as they travel through different mediums. In other words, when measuring the thickness of a steel section with paint, the ultrasound waves first travel through the paint (first medium) to the steel (second medium) and then through the paint on the opposite side (third medium). After passing through the third medium, it would reflect and travel through these three mediums back to the source. The speed of ultrasound would be influenced by the change in mediums, thus

affecting the thickness measured. At the interface of every medium, there would be partial refractions and partial reflections occurring at every medium's interface, possibly affecting the measurements. Overall, the measurements do not consider the influence of the thickness of the paint on the thickness measured.

In Table 3.1 the measurements for residual web thickness of the specimens were taken using UT gauge for three different cases (A) paint retained on both sides (B) paint was removed on one side (C) paint was removed on both sides. Additionally, the difference between cases A and C was calculated. As it can be seen from Table 3.1, measuring the thickness of the web with paint gives an average of additional 0.023 in., which does not accurately reflect residual thickness of the web and may result in overestimating the section loss.

Secondly, the paint used on the specimens contained lead which was confirmed through testing with 3 M lead check swabs. Working on the specimens with lead-based paint was unsafe, and hence they were sandblasted at a different facility to remove and handle the lead-based paint safely. After sandblasting, full-depth section loss measurements in the web were obtained from the girder end up to a length of 5 ft. as shown in Figure 3.2.

The web of the specimens was divided into a grid of size 1 in. $\times$ 1 in., and the remaining thickness was measured at each grid point using the ultrasonic device (T-Mike BTM), as shown in Figure 3.1, Figure 3.4 and Figure 3.7. Contour plots of remaining web thickness measurements of Specimens 1, 2, and 3 were developed and are shown in Figure 3.3 through Figure 3.8. The color bar on the right side in Figure 3.3 through Figure 3.8 indicates the color scale corresponding to the remaining thickness of the web, where light orange corresponds to light section loss, and the dark brown color corresponds to severe section loss.

3.2 Typical Section Loss Profile

The remaining thickness measurements of the web of Specimens 1, 2, and 3 measured by ultrasonic thickness gauge were analyzed in detail by developing contour plots and four observations were made. Firstly, Specimen 1 does not have significant section loss and the remaining thickness is close to the nominal thickness shown in Figure 3.3. In contrast, Specimen 2 and Specimen 3 had severe section loss due to corrosion at the bottom of the web just above the location of the bearing and the top of the web (between the girder end and partial depth transverse stiffener) as shown in Figure 3.5 and Figure 3.8. Secondly, corrosion in the web was non-uniform and had pitting corrosion. Thirdly, Specimens 2 and 3 had holes resulted because of complete section loss of the web due to corrosion. In Specimen 2, two holes were present at the bottom of the web as shown in Figure 3.4 while Specimen 3 has one

Figure 3.1 Section loss measurements using an ultrasonic thickness gauge.

TABLE 3.1
Spot-check for residual web thickness with paint existing on both sides, after removal of paint on one side, and after removal of paint on both sides

	Ultrasonic Thickness Gauge Measurements			
Nominal Web Thickness (in)	**Steel Web Section with Paint Existing on Both Sides A (in.)**	**Steel Web Section with Paint Removed on One Side B (in.)**	**Steel Web Section After Removal of Paint on Both Sides C (in.)**	**Differences in Measurements Due to Paint on Both Sides (C–A) (in.)**
0.415	0.437	0.421	0.402	0.035
	0.438	0.426	0.407	0.031
	0.429	0.428	0.415	0.014
	0.434	0.425	0.418	0.016
	0.428	0.428	0.417	0.011
	0.433	0.417	0.414	0.019
	0.440	0.427	0.413	0.027
	0.438	0.424	0.415	0.023
	0.442	0.425	0.414	0.028
	0.436	0.422	0.412	0.024
Average	*0.436*	*0.424*	*0.413*	*0.023*

Figure 3.2 Girders sandblasted up to 5 ft. from the girder end.

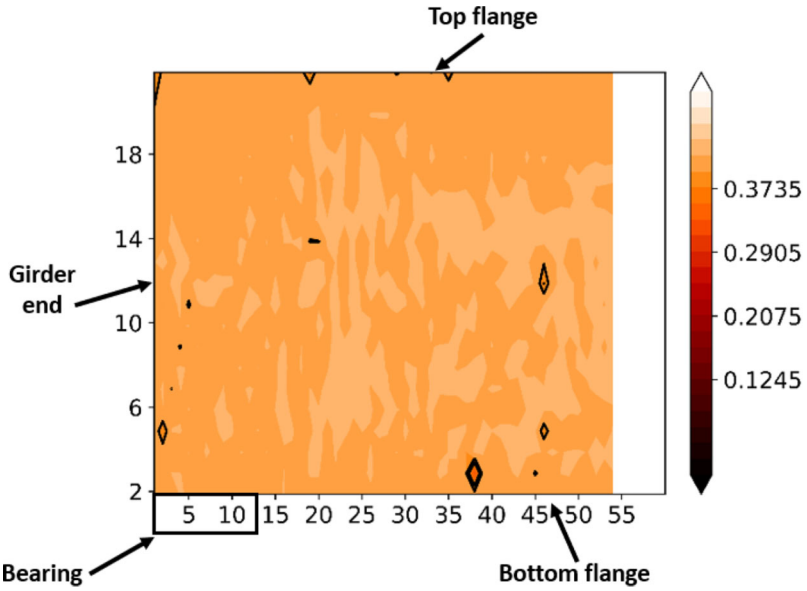

Figure 3.3 Contour plot of remaining thickness of Specimen 1.

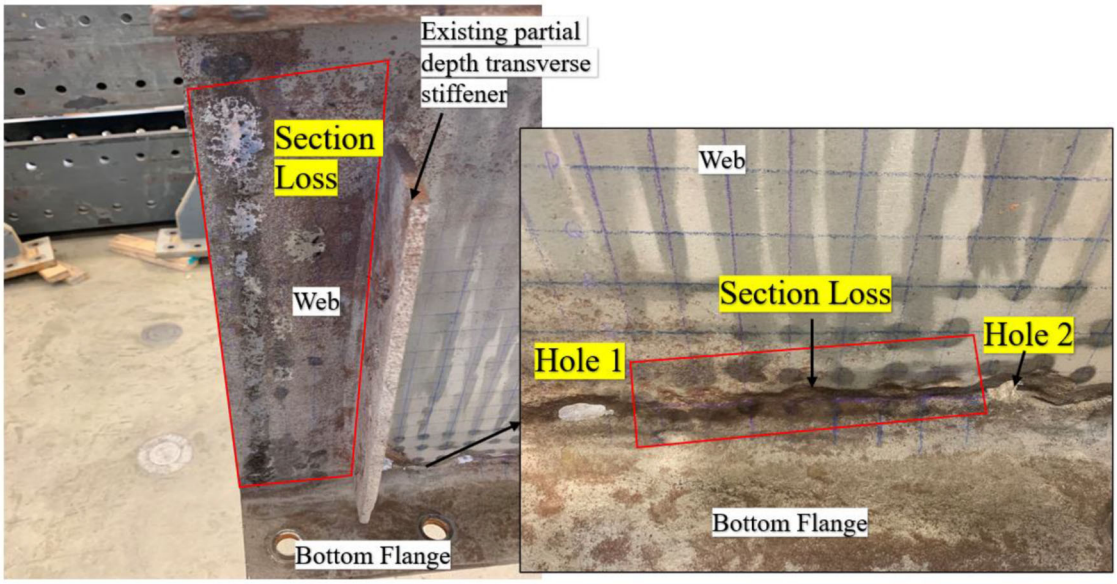

Figure 3.4 Specimen 2 corrosion details and grids on the web where remaining thickness is measured.

hole at the bottom web and another hole at the top of the web, between the girder end and existing partial depth transverse stiffener as shown in Figure 3.6 and Figure 3.7. Overall, section loss in the web of the specimens varied significantly from complete section loss (100%) at the location of holes to nominal thickness with no section loss.

Contour plots developed consisted of section loss varying from 0 to 100% and were modified to focus on regions with section loss greater than 10% (regions with

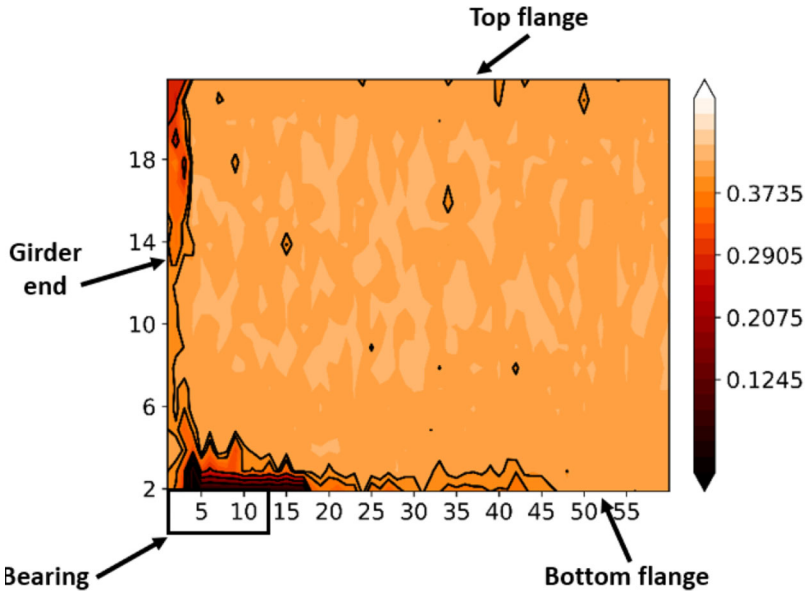

Figure 3.5 Contour plot of remaining thickness of Specimen 2.

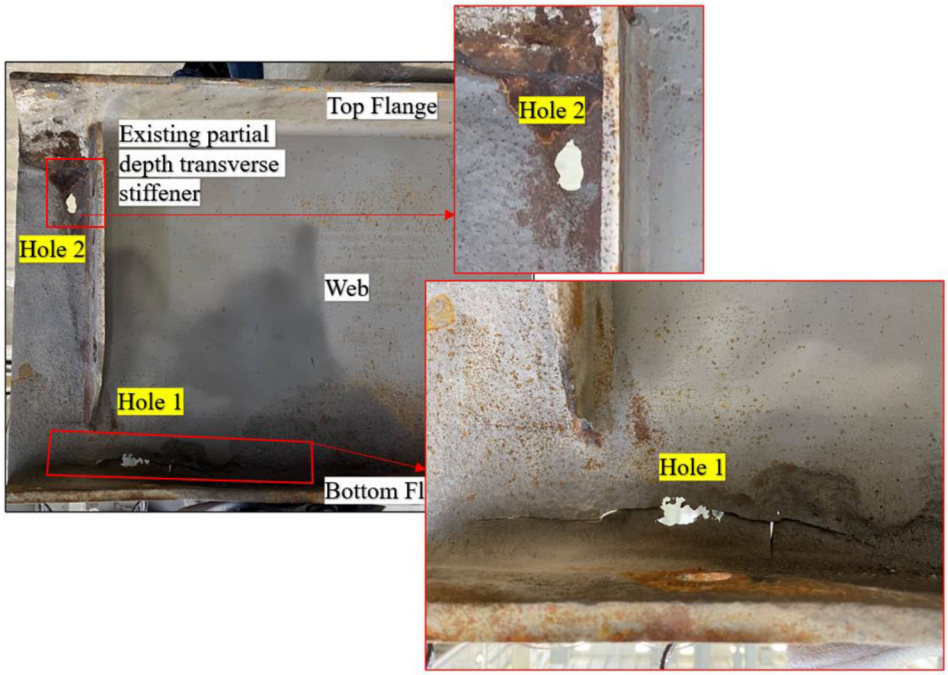

Figure 3.6 Specimen 3 corrosion details.

a remaining thickness less than $0.9_{tw\_nominal}$) as shown in Figure 3.9. The shape of the section loss was quite complex, and the shape of the section loss can be approximately assumed to be a trapezoidal shape. The shape of the corroded region for Specimen 2 can be approximated to be triangular in shape and rectangular in shape for Specimen 3. However, the trapezoidal shape was more realistic in a more general scenario where the corrosion is more significant in the web closer to the girder end due to the leakage from the expansion joint at the girder end as shown in Figure 3.10.

3.3 Artificial Section Loss

Among obtained corroded girders only seven were severely corroded, while the remaining 14 had light or moderate corrosion. Two out of seven severely corroded girders were selected for the experimental program, while the rest of the severely corroded girders were saved for conducting large-scale experiments after performing the repair, which is the scope of ongoing project SPR-4635. Five girders out of seventeen girders that were light to moderately corroded girders were

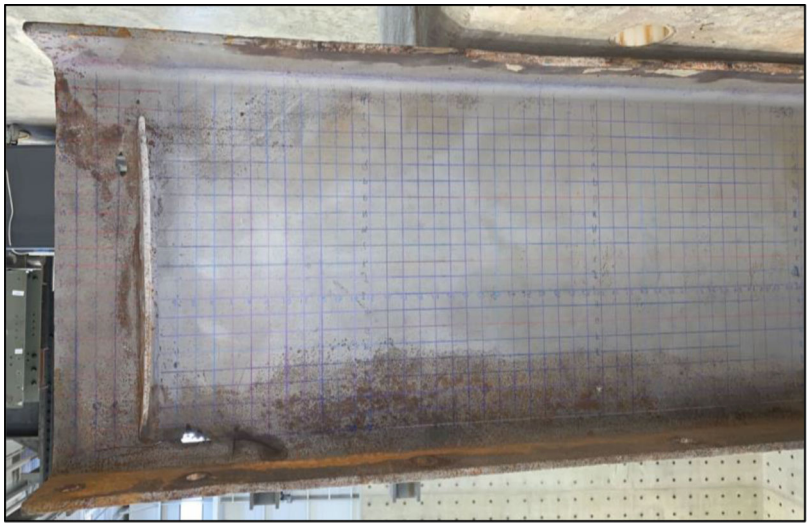

Figure 3.7 Specimen 3 and grids on the web where the remaining thickness is measured.

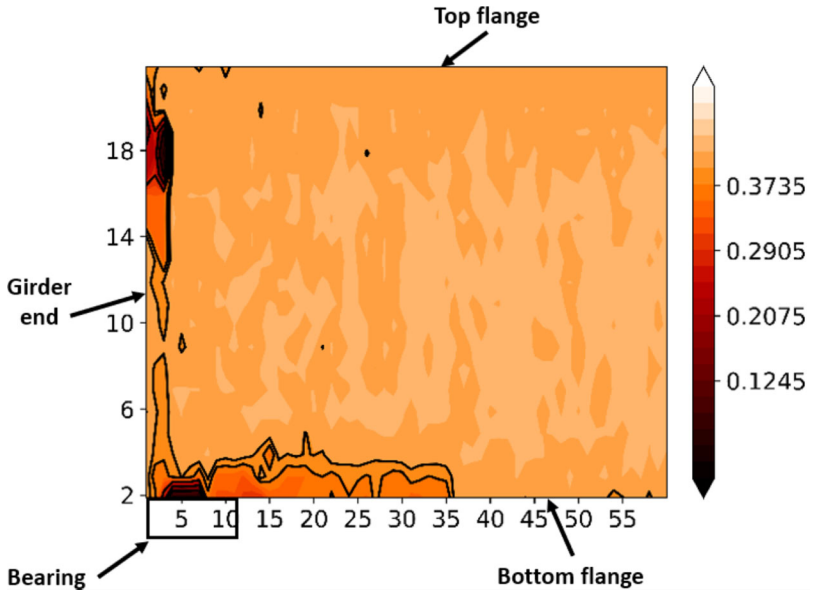

Figure 3.8 Contour plot of remaining thickness of Specimen 3.

selected. Two of the five girders with light to moderate corrosion damage are shown in Figure 3.11 and Figure 3.12.

The section loss profile observed in Specimens 2 and 3 was approximately trapezoidal in shape and with majority of section loss concentrated towards the girder end (Figure 3.9, Figure 3.10). Based on this observation a typical section loss profile was developed as shown in Figure 3.13. This section loss profile is trapezoidal in shape, with 70% section loss in Region 1, towards the girder end and 30% section loss in Region 2. A transition region of 2 in. was provided when there was a change in the remaining thickness. This section loss profile was induced artificially in Specimens 4, 5, 6, and 7 through grinding as shown in Figure 3.14 through Figure 3.21.

3.4 Recommendation for Deduction of Paint Thickness from Thickness Measurements

Steel sections with regions that have localized corrosion may not have any paint remaining in that region. However, during maintenance operations, there is a possibility for a girder having uniform or localized corrosion to be cleaned and painted to prevent further deterioration. When inspecting the residual thickness of girders with paint, it would not be practical to remove the paint while measuring the thickness and repainting

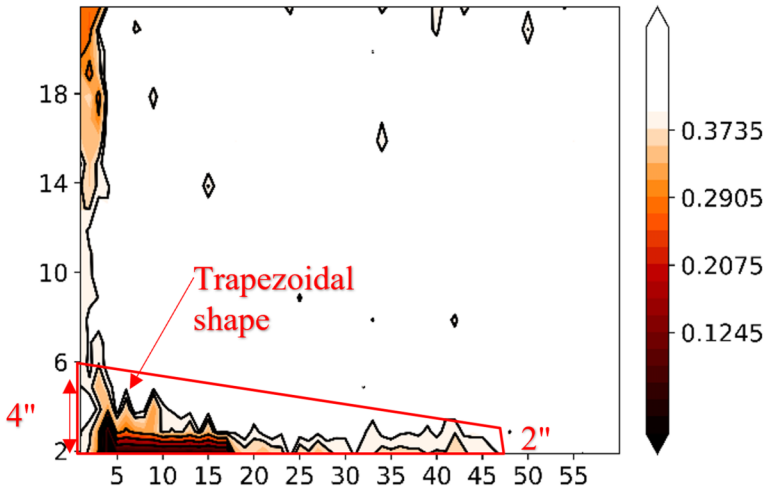

Figure 3.9 Specimen 2 contour plot of remaining thickness less than 0.9 $t_{w\_nominal}$.

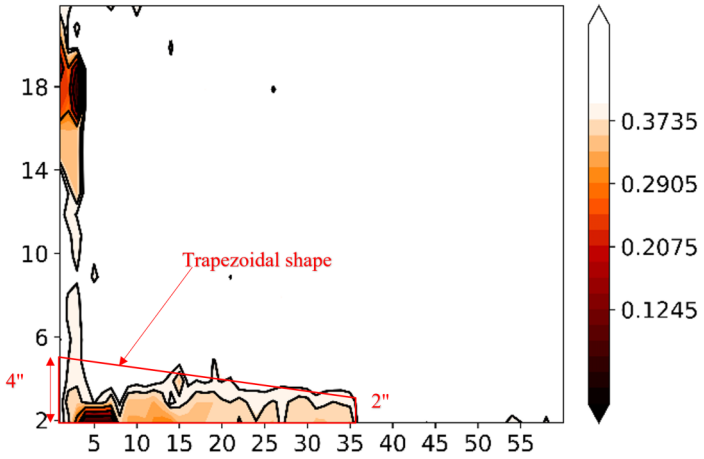

Figure 3.10 Specimen 3 contour plot of remaining thickness less than 0.9 $t_{w\_nominal}$.

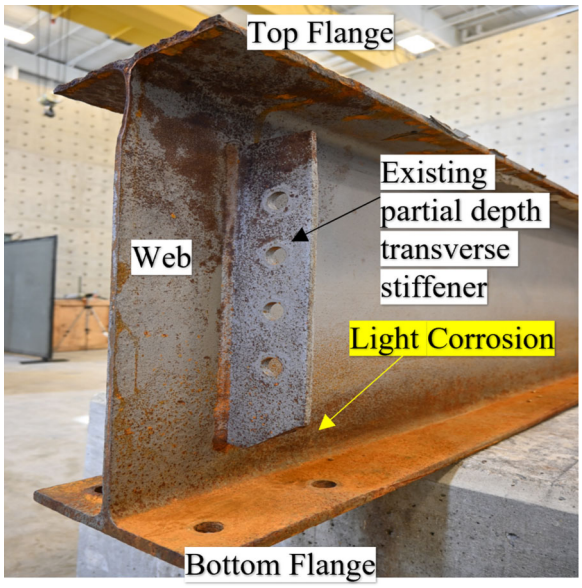

Figure 3.11 Specimen 5 girder with light corrosion.

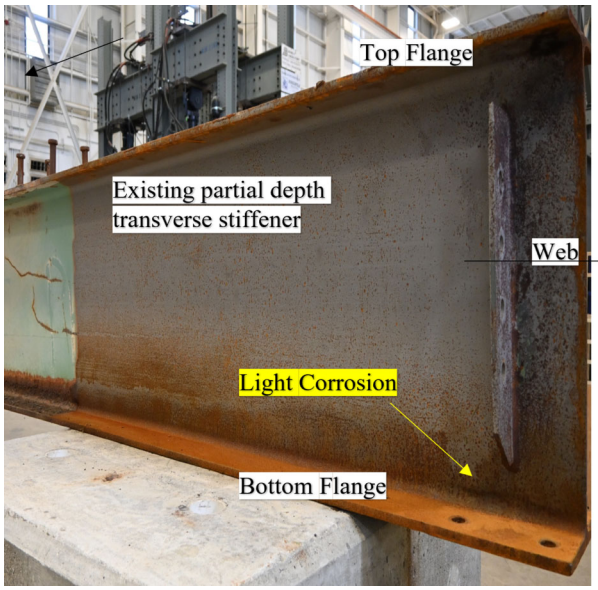

Figure 3.12 Specimen 6 girder with light corrosion.

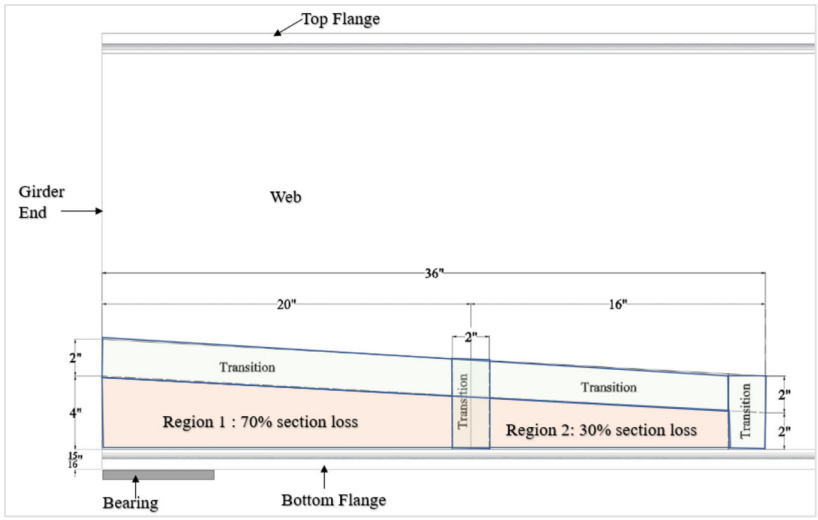

Figure 3.13 Section loss profile induced artificially in Specimens 4, 5, and 6.

Figure 3.14 Specimen 4 after inducing section loss artificially through grinding.

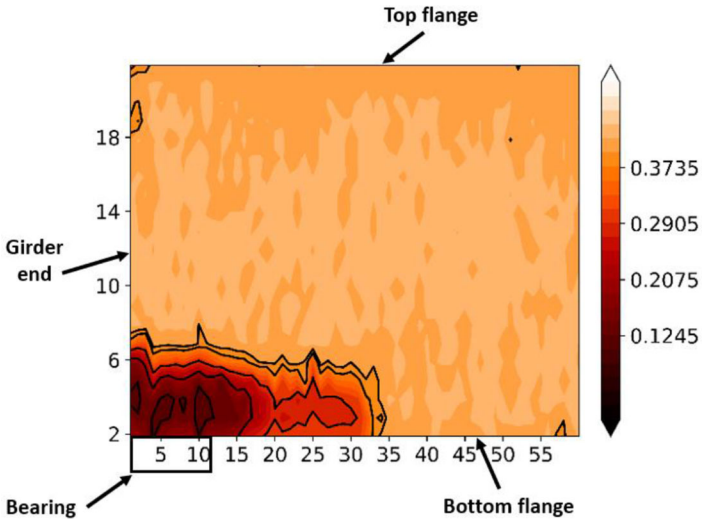

Figure 3.15 Specimen 4 contour plot of thickness measurements.

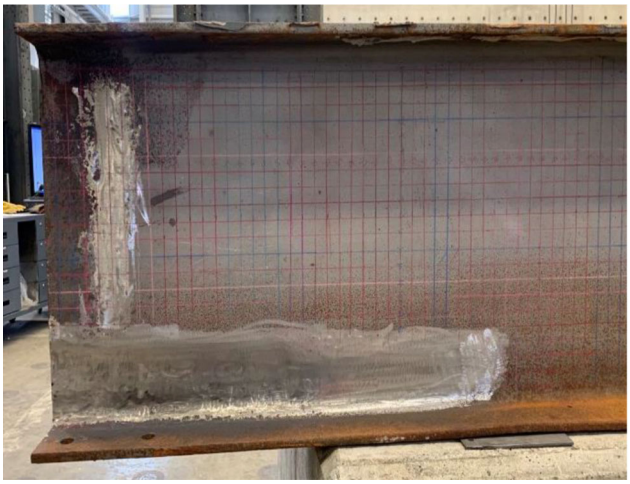

Figure 3.16 Specimen 5 after inducing section loss artificially through grinding.

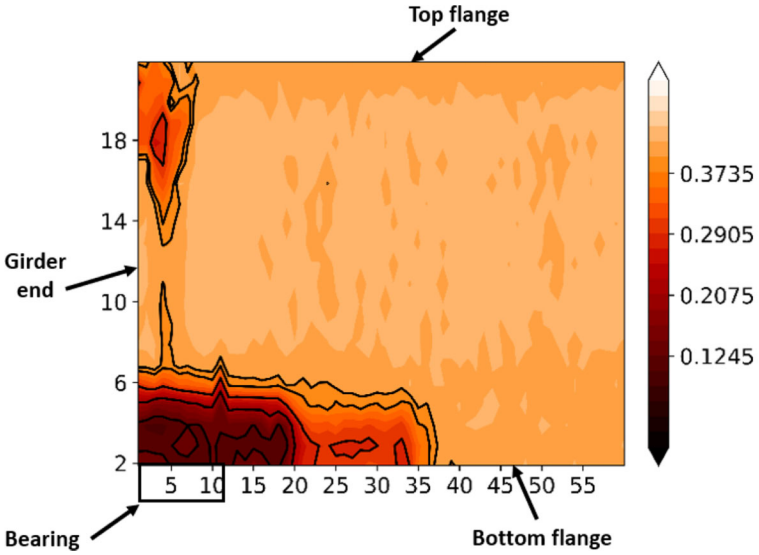

Figure 3.17 Specimen 5 contour plot of thickness measurements.

Figure 3.18 Specimen 6 after inducing the section loss.

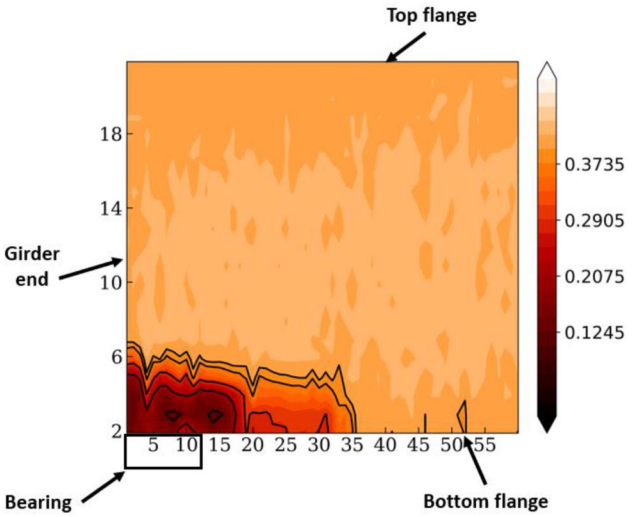

Figure 3.19 Specimen 6 contour plot of thickness measurements.

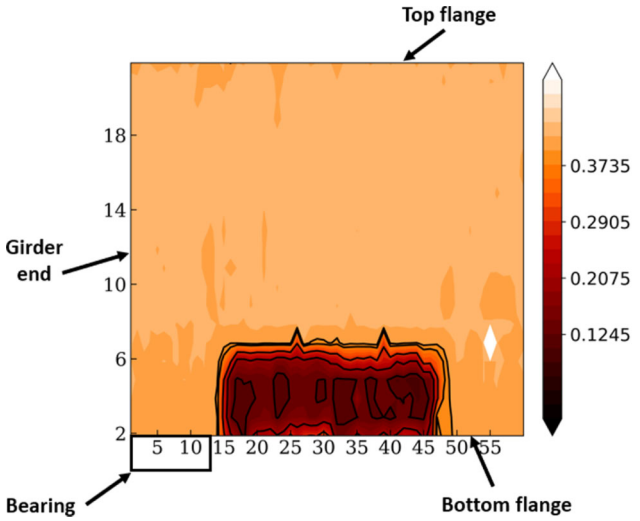

Figure 3.21 Specimen 7 contour plot of thickness measurements.

Figure 3.20 Specimen 7 after inducing the section loss.

it after the inspection. Oppositely, it would be more reasonable to obtain residual thickness measurements with paint and deduct from it an approximate value of paint thickness.

For that purpose, residual thickness measurements were obtained at ten various locations on the steel web plate for three scenarios. In the first scenario (A), measurements were obtained from the steel web plate with paint existing on both sides. In the second scenario (B), paint was removed on one side, and measurements were obtained at the same ten locations. In the third scenario (C), paint was removed on the other side before taking measurements which would be the actual residual thickness of the steel web plate at those ten locations. Measurements in each scenario were recorded and provided in Table 3.1. Differences in measurement between the first scenario (A) and the third scenario (C) would provide the extra thickness measured due to paint at each of the ten locations. Averaging the differences (A–C) gives the value of 23 mils or 0.02 in. which would be an approximate estimate for the extra thickness measured contributing to existing paint. Deducting 20 mils or 0.02 in. from the thickness measurements of the steel sections with paint would provide an accurate estimate of the actual residual thickness of the steel section.

3.5 Digital Geometric Three-Dimensional (3D) Scans of Corroded Girders

Digital geometric three-dimensional (3D) scans of the girders were generated using photogrammetric technique. Photogrammetry generates 3D surfaces from stitching digital overlapping images obtained from varying perspectives. The process of obtaining digital images using a camera is shown in Figure 3.22.

After establishing the steps to generate dense point cloud, a custom rig was built to expedite the process of taking images with the help of eight cameras and a receiver. The custom rig with eight camera attachments is illustrated in Figure 3.23. For the purpose of taking images of the specimen at varying angles, the cart was placed 610 mm (24 in.) away from the specimen and moved in an elliptical path around it as shown in Figure 3.24.

Based on camera parameters such as focal length, angle, lens distortion and other variables the accurate distances were calculated between tie-points. Tie-points refer to the unique feature spots present in a single image. Whereas, stitching of digital images refer to identifying identical tie-points in overlapping images and merging them into a unified surface. Tie-points generated were sparse points present in a 3D cartesian coordinate space. The tie-points were post-processed to

Figure 3.22 3D scanning of corroded girder.

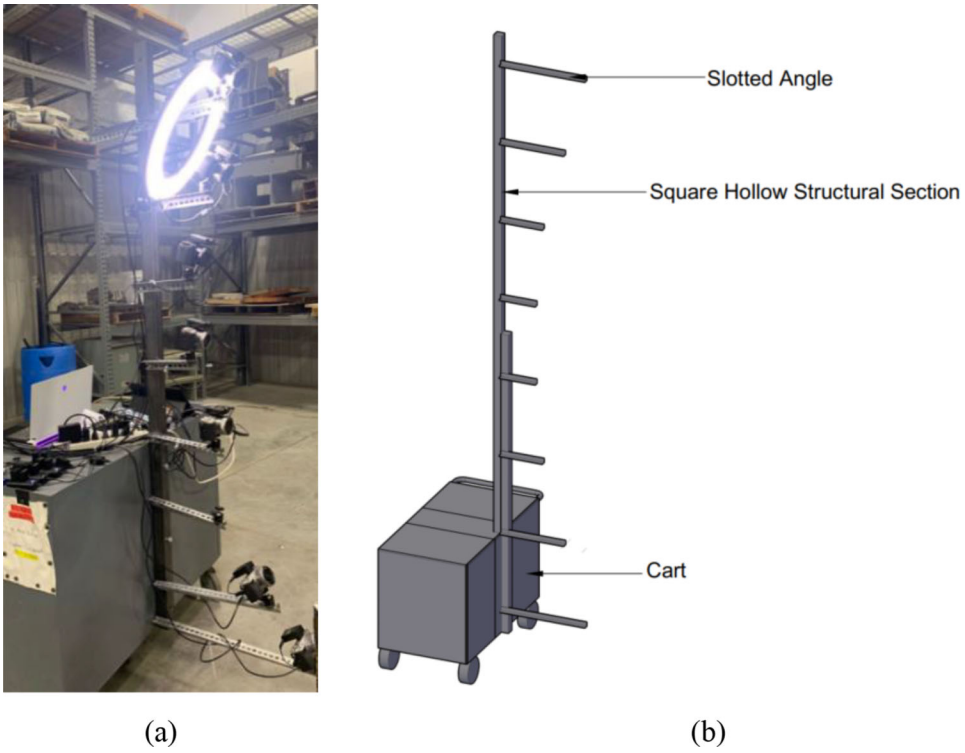

Figure 3.23 Custom rig with eight cameras.

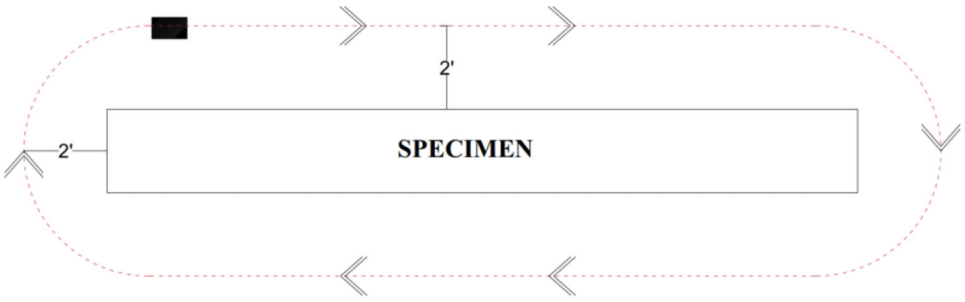

Figure 3.24 Path traversed around the specimen (plan view).

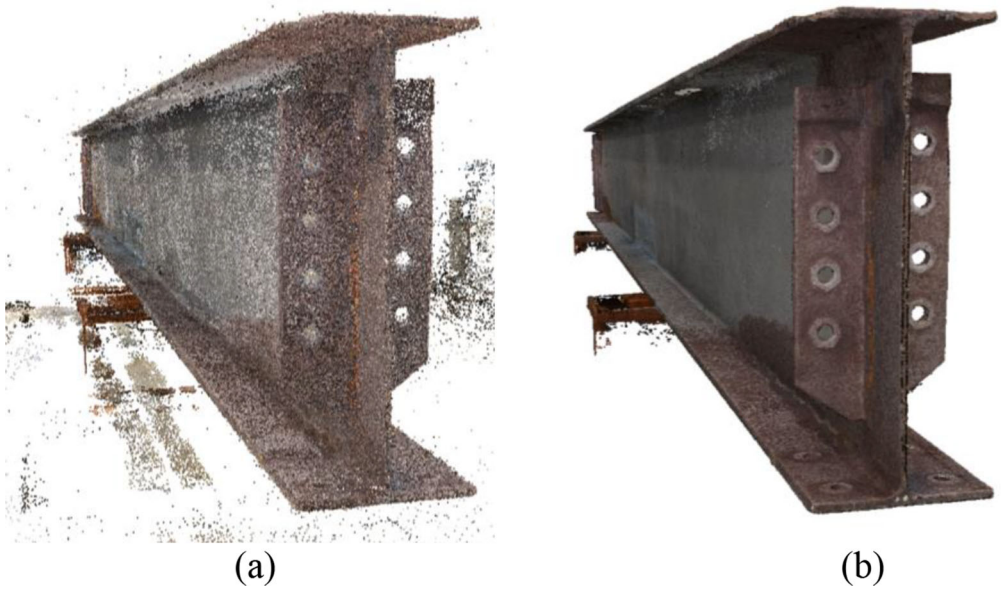

Figure 3.25 Comparison of (a) tie-point cloud and (b) dense point cloud.

generate dense point cloud. The density was manually adjusted to highest setting to increase the level of detail. A comparison of tie-points and dense point cloud is highlighted in Figure 3.25. Point cloud data generated from the scan typically consisted of 5–10 million points.

Even though generating 3D scans was out of the scope of the project, it was performed nonetheless to attain two primary objectives. First, to determine the section loss profile and compare it with the measurements obtained from nondestructive ultrasonic testing. The section loss measurements from the photogrammetry were verified with data obtained using a UT gauge and captured realistic section loss measurements. Secondly, to develop a realistic 3D model representing the actual specimen and perform finite element analysis (FEA) simulations. At present, work is in progress at Purdue University to develop a FEA model from the generated point cloud data.

4. EXPERIMENTAL PROGRAM

4.1 Test Matrix

Full-scale tests were conducted on seven specimens of the same size and length, 22-ft. long W24 × 68 rolled steel sections. All the specimens had section loss in the web and were subjected to shear loading. The objective of the experimental program was to determine the corroded girders' residual bearing and shear strength. It was essential for the specimen to fail either in bearing or shear before any other failure modes. From the preliminary numerical models and previous research, it was observed that web local crippling was the governing failure mode for the unstiffened corroded girders. However, shear buckling, or shear yielding may govern for the stiffened girders, provided the bearing stiffeners have adequate strength against web local crippling. In addition, from the preliminary numerical models with the W24 × 68 section, flexural yielding of the bottom flange was observed before the shear failure of the stiffened girders from the preliminary numerical models.

Reinforcements such as a cover plate and full-depth transverse stiffeners were provided to four specimens. A cover plate was provided at the outer face of the bottom flange in two specimens to exclude any effects due to the flexural yielding of the bottom flange. All the naturally corroded girders obtained were unstiffened, and therefore, additional full depth bearing stiffeners were fillet welded to the web, top flange, and bottom flange just above the bearing. In addition, full-depth stiffeners were provided at the loading region to ensure stability at the loading area. Thus, the test matrix consists of specimens with a combination of full-depth transverse stiffeners, cover plates, and pre-existing partial-depth transverse stiffeners. Specimen details and particulars of corrosion affected region for each Specimen have been provided below after Table 4.1.

4.2 Specimen Details

4.2.1 Specimen 1

Specimen 1 was a W 24 × 68 steel section and 22 ft. in length. Specimen 1 had existing partial depth transverse stiffeners of thickness 3/8 in., and fillet welded to the web at a distance of 4 in. from the beam end. Diaphragm beams were bolted to these partial-depth transverse stiffeners when the girder was in service. These partial-depth transverse stiffeners were retained during the testing. Steel shear studs on the top flange's outer face were cut and removed. Section loss in the web was because of natural corrosion, but very minimum, less than 0.1 $t_{w\_nominal}$ or 10% section loss. A pair of 3/4-in. full-depth transverse stiffeners were

TABLE 4.1
Specimen details

Specimen Number	Section	Beam Depth (in.)	Nom. Web Thickness (in.)	Section Loss (natural/artificial)	Loading	Pre-Existing Partial Depth Transverse Stiffeners	Full Depth Transverse Stiffeners	Cover Plate
1	W24 × 68	23.73	0.415	Natural	Shear	Yes	Yes	Yes
2	W24 × 68	23.73	0.415	Natural	Shear	Yes	Yes	Yes
3	W24 × 68	23.73	0.415	Natural	Shear	Yes	Yes	–
4	W24 × 68	23.73	0.415	Artificial	Shear	Yes	–	–
5	W24 × 68	23.73	0.415	Artificial	Shear	–	–	–
6	W24 × 68	23.73	0.415	Artificial	Shear	Yes	Yes	–
7	W24 × 68	23.73	0.415	Artificial	Shear	Yes	–	–

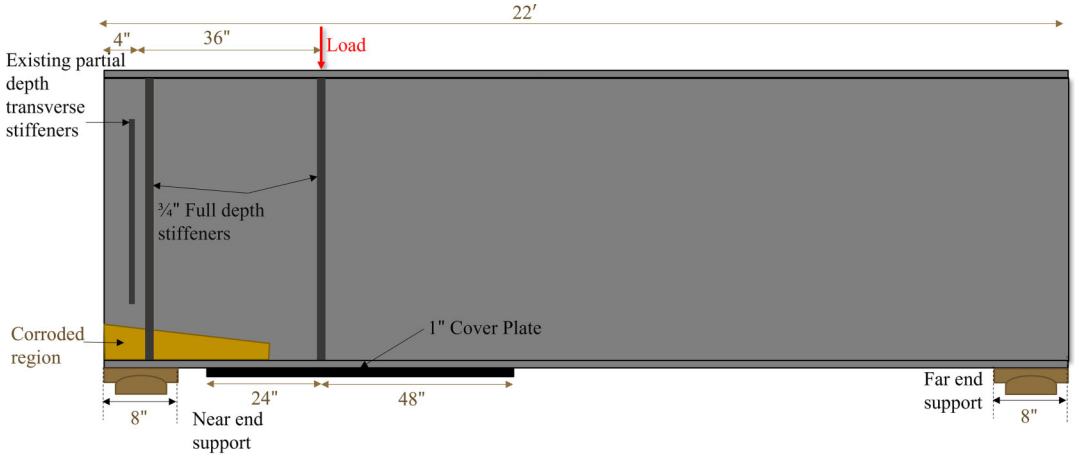

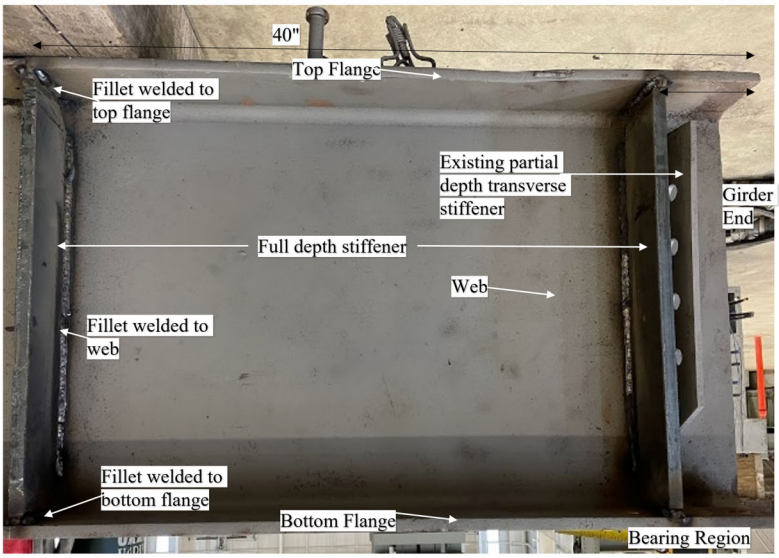

Figure 4.1 Specimen 1 geometry and details.

provided at the bearing region at 4 3/4 in. from the girder end, adjacent to the existing partial-depth transverse stiffeners and fillet welded to the web, inner faces of the top flange and bottom flange. Another pair of full-depth transverse stiffeners were provided at 40 in. from the girder end, where loading was applied through a spreader beam on the top flange. A cover plate of 1 1/2-in. thick and about 6 ft. long was bolted face to the bottom flange as shown in Figure 4.1. Specimen 1 was a part of the commissioning test to test the entire testing apparatus and benchmark the residual strength of the girder with no or minimum section loss.

4.2.2 Specimen 2

Specimen 2 was also a W24 × 68 steel section and 22 ft. in length. Pre-existing partial depth transverse stiffeners of thickness 3/8. were fillet welded to the web at a distance of 4 in. from the girder end. Diaphragm beams were bolted to these partial-depth transverse stiffeners when the girder was in service. During the demolition, the diaphragm beams were unbolted and removed. However, these partial-depth transverse stiffeners were retained during the testing. Steel shear studs on the top flange's outer face were cut and removed. Section loss in the web was because of natural corrosion, but severe compared to Specimen 1 and was concentrated on the bottom of the web. Section loss was present at the top of the web, between the girder end and partial depth transverse stiffener. There were three holes at the bottom of the web as shown in Figure 4.2. Hole 1 was approximately 1 11/16-in. diameter at 6 in. from the girder end. Hole 2 was approximately a 7/8-in. diameter at a distance of 9 5/8-in. from the girder end. Hole 3 was approximately 1 3/8-in. diameter at a distance of 18 3/16 in. from the girder end. Section loss profile was as shown in Figure 4.2. A pair of 3/4-in. full-depth transverse stiffeners were provided about 5 in. and 40 in. from the girder end and fillet welded to the web like Specimen 1. A cover plate of 1 1/2-in. thick and about 6 ft. long was bolted to the bottom flange as shown in Figure 4.3.

4.2.3 Specimen 3

Specimen 3 was a W24 × 68 steel section and 22 ft. in length. Pre-existing partial depth transverse stiffeners of thickness 3/8 in. were fillet welded to the web at a distance of 4 in. from the girder end. Diaphragm beams were bolted to these partial-depth transverse stiffeners when the girder was in service. During the demolition, the diaphragm beams were unbolted and removed. However, these partial-depth transverse stiffeners were retained during the testing. Steel shear studs on the top flange's outer face were cut and removed. Section loss in the web was due to natural corrosion and severe similar to Specimen 2 and was concentrated at the bottom of the web. Section loss was present at the top of the web between the girder end and partial depth transverse stiffener. There were two holes at the bottom of the web, as shown in. Hole 1 was of approximately 1-1/2 in. width at a 6-13/16 in. from the girder end. Hole 2 was of width 1-1/4 in. at a distance of 5-7/8 in. from the top flange's inner face. Section loss profile was shown in Figure 4.4 and Figure 4.5. In addition to holes, cracks were located both to the right side (length = 4″) and to the left side (length = 4-13/16″) of Hole 1. A pair of 3/4" full-depth transverse stiffeners were provided about 5 in., and 40 in. from the girder end and fillet welded to the web like Specimens 1 and 2 as shown in Figure 4.1. The cover plate provided in Specimens 1 and 2 was not provided here.

4.2.4 Specimen 4

Specimen 4 was a W24 × 68 steel section and 22 ft. in length, just like all the other specimens. Pre-existing partial depth transverse stiffeners of thickness 3/8 in. were fillet welded to the web at a distance of 4″ from the girder end. Diaphragm beams were bolted to these partial-depth transverse stiffeners when the girder was in service. During the demolition, the diaphragm beams

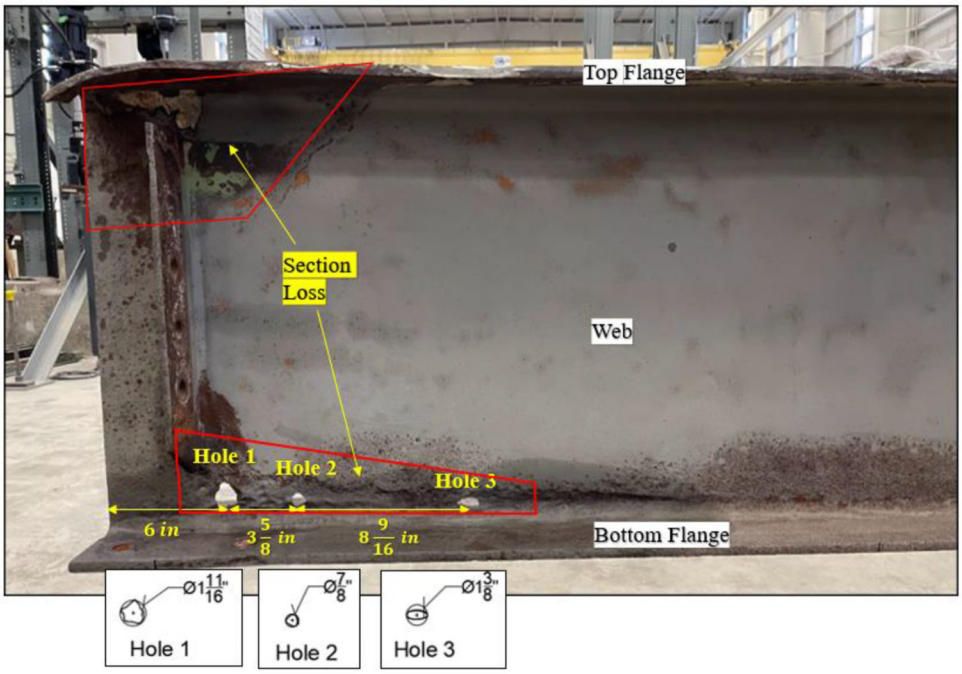

Figure 4.2 Specimen 2 section loss profile.

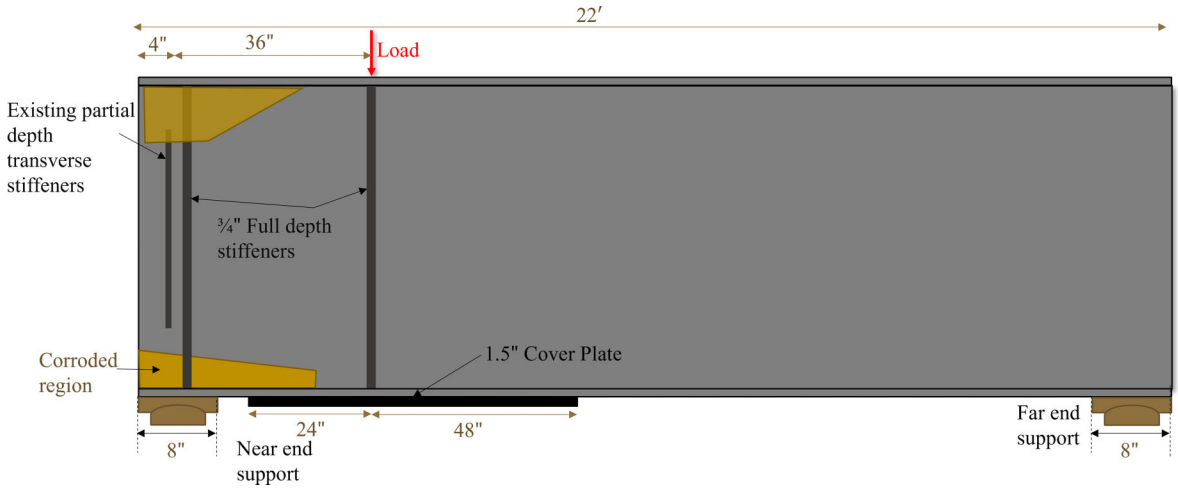

Figure 4.3 Specimen 2 geometry and corrosion details.

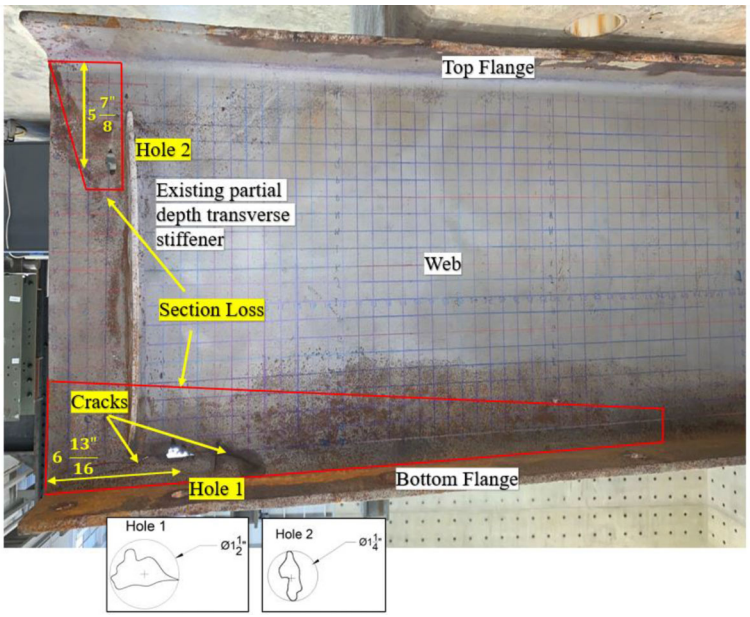

Figure 4.4 Specimen 3 section loss profile.

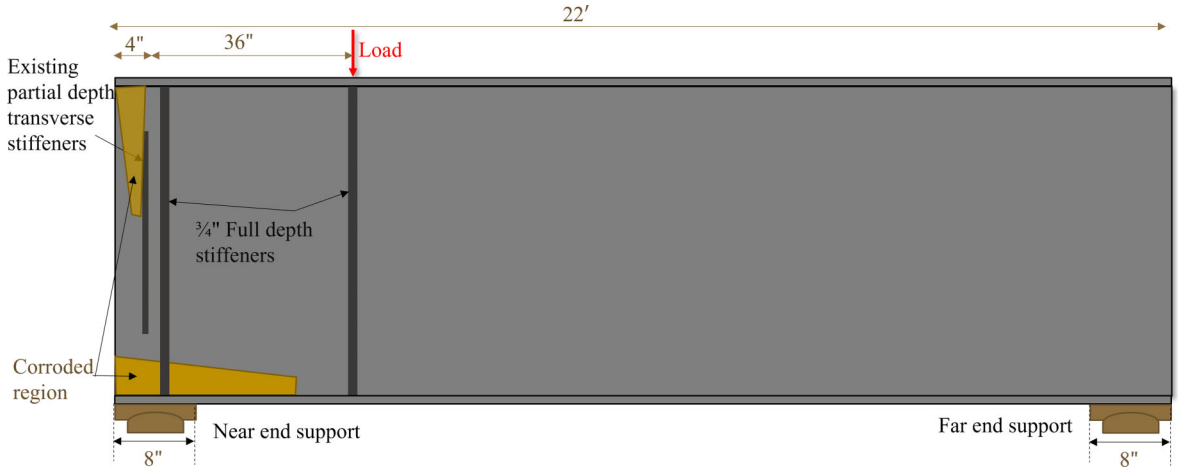

Figure 4.5 Specimen 3 geometry and details.

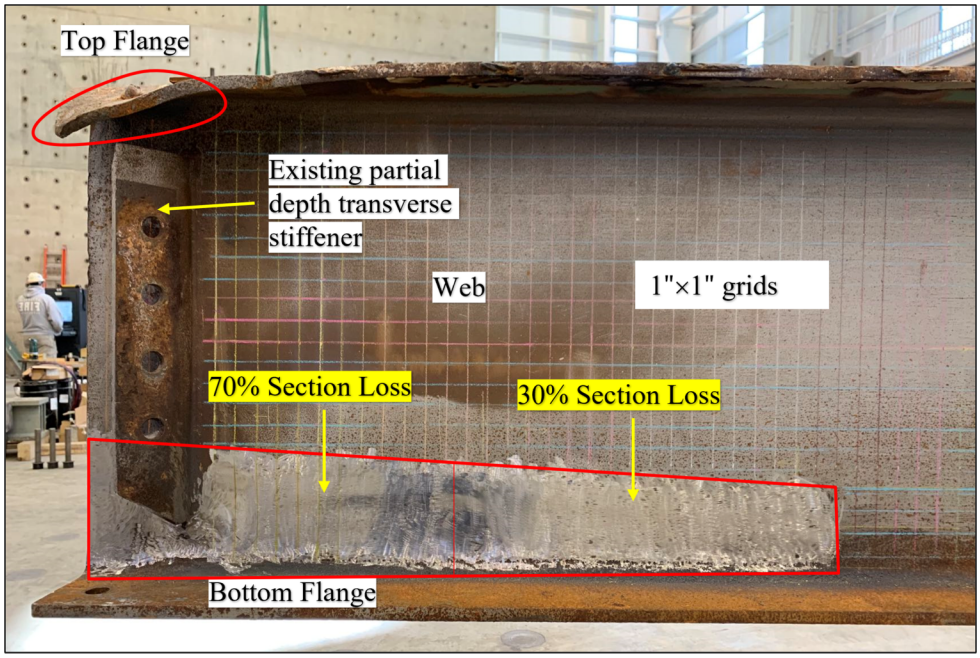

Figure 4.6 Specimen 4 section loss profile.

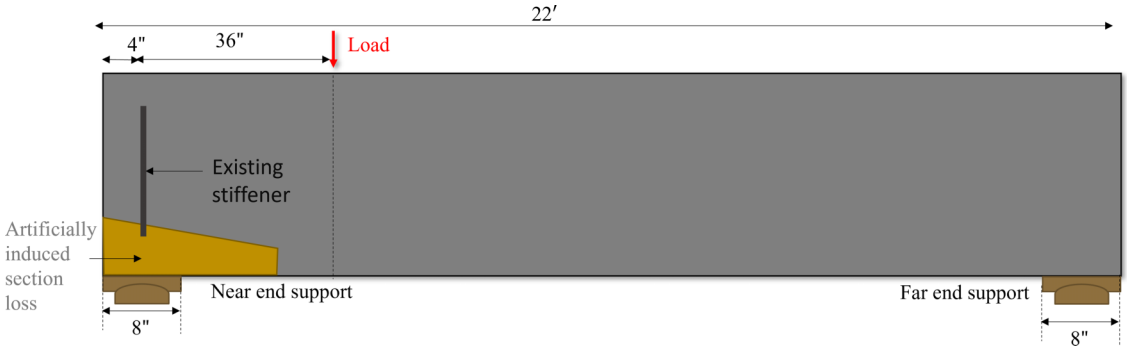

Figure 4.7 Specimen 4 geometry and details.

were unbolted and removed. However, these partial-depth transverse stiffeners were retained during the testing. Steel shear studs on the top flange's outer face were cut and removed. The specimen was lightly corroded. Therefore, there was no significant section loss. However, studying the behavior and residual capacity of unstiffened girders with severe section loss was necessary. For this purpose, the bottom of the specimen's web was intentionally made thinner through grinding (Figure 4.6 and Figure 4.7). Dimensions and profile of the section loss induced artificially were discussed in detail in Section 3.3.

4.2.5 Specimen 5

Specimen 5 was a W24 × 68 steel section and 22 ft. in length. Specimen initially had pre-existing partial depth transverse stiffeners of thickness 3/8 in. fillet welded to the web at a distance of 4 in. from the girder end. Diaphragm beams were bolted to the partial-depth transverse stiffeners when the girder was in service. These pre-existing partial depth transverse stiffeners were cut and removed, and the surface was ground to smooth before the experiment, unlike Specimen 4. Steel shear studs on the top flange's outer face were cut and removed. The specimen was lightly corroded. Therefore, there was no significant section loss. Similar to Specimen 4, the bottom part of the specimen's web was intentionally made thinner through grinding (Figure 4.8 and Figure 4.9). Dimensions and profile of the section loss induced artificially were described in detail in Section 3.3.

4.2.6 Specimen 6

Specimen 6 was a W24 × 68 steel section and 22 ft. in length. Pre-existing partial depth transverse stiffeners of thickness 3/8 in. were fillet welded to the web at a distance of 4 in. from the girder end. Diaphragm beams were bolted to these partial-depth transverse stiffeners when the girder was in service. During the demolition, the diaphragm beams were unbolted and removed. However, these partial-depth transverse stiffeners were

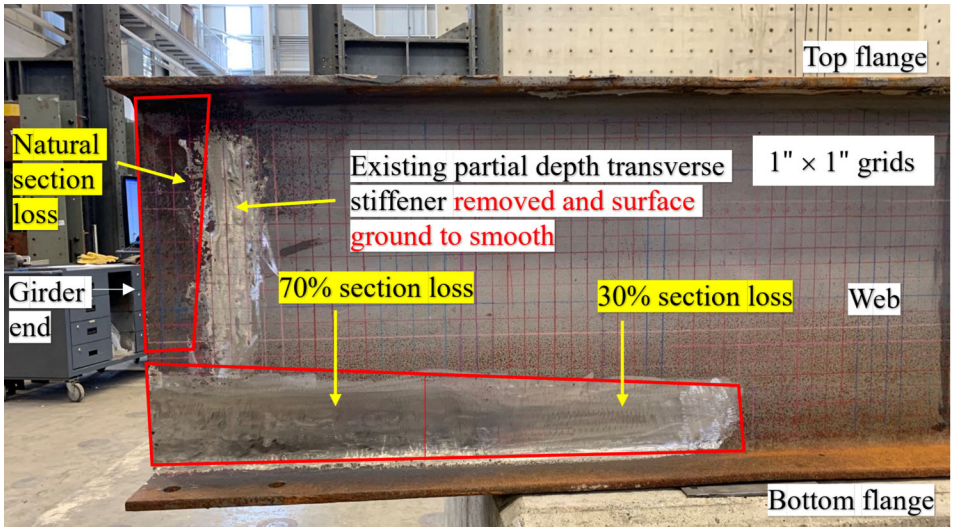

Figure 4.8 Specimen 5 section loss profile.

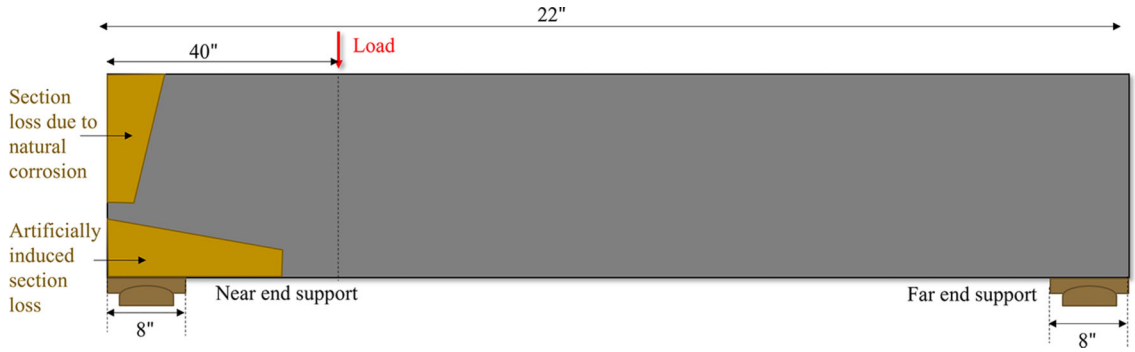

Figure 4.9 Specimen 5 geometry and details.

retained during the testing, like Specimens 1, 2, 3, and Specimen 4. Steel shear studs on the top flange's outer face were cut and removed. The specimen was lightly corroded (Figure 4.10). Therefore, there was no significant section loss. Just like Specimens 4 and 5, the bottom of the specimen's web was intentionally made thinner through grinding (Figure 4.11 and Figure 4.12). Dimensions and profile of the section loss induced artificially were discussed in detail in Section 3.3

4.2.7 Specimen 7

Specimen 7 was a W24 × 68 steel section and 22 ft. in length. Pre-existing partial depth transverse stiffeners of thickness 3/8 in. were fillet welded to the web at a distance of 4 in. from the girder end. Diaphragm beams were bolted to these partial-depth transverse stiffeners when the girder was in service. During the demolition, the diaphragm beams were unbolted and removed. However, these partial-depth transverse stiffeners were retained during the testing, like Specimens 1, 2, 3, 4, and 6. Steel shear studs on the top flange's outer face were cut and removed. The specimen was lightly corroded. Therefore, there was no significant section loss like in Specimens 4, 5, and 6. For studying the effect of the section loss on the flexural capacity of the corroded steel girder, the bottom of the specimen's web at mid-span was intentionally made thinner through grinding. The location and profile of the section loss induced artificially are shown below (Figure 4.13, Figure 4.14).

4.3 Material Properties

All the specimens were acquired from two bridges, and as per construction drawings, the specified nominal material property of the steel used was 36 ksi. However, when tested, the actual material property of steel showed higher strength than specified, as expected. From each specimen, six steel coupons were cut from the web after the test in the region subjected to high shear from each specimen. Additionally, two steel coupons were cut each from the top and bottom flange (only for Specimen 1). Tension tests of steel coupons were performed as per ASTM E8 (2022) and yield strength (F_y) and ultimate strength (F_u) of coupons from are shown in Table 4.2.

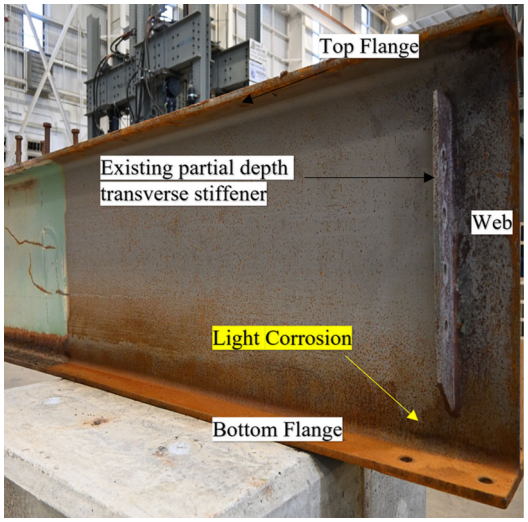

Figure 4.10 Specimen 6 before inducing section loss.

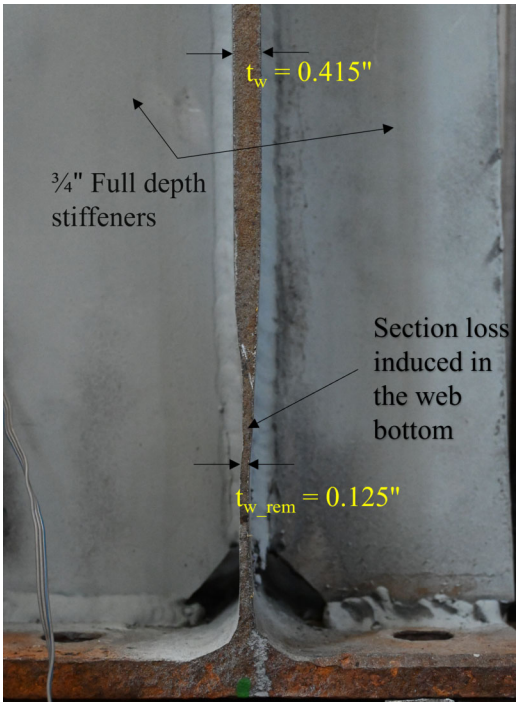

Figure 4.11 Specimen 6 after inducing section loss.

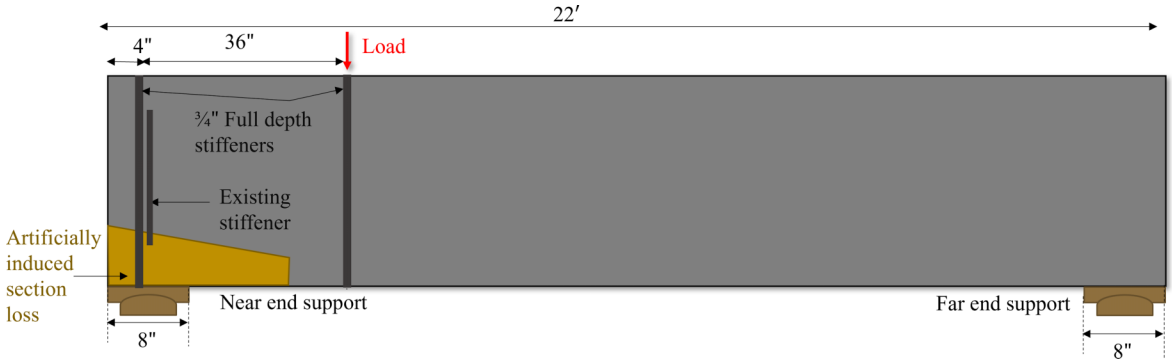

Figure 4.12 Specimen 6 geometry details.

4.4 Test Setup

Test set up was designed to perform full scale test on all the specimens. Specimens were simply supported and subjected to shear loading. The test set up used are shown in Figure 4.15 and Figure 4.18. Typical length of the girder was 22 ft. and girder end close to the corroded web region is referred to as near end and the opposite end of the girder is referred to as far end in this study. For Specimens 1–6, load was applied at 40 in. from the near end of the specimen (Figure 4.15 and Figure 4.16). Load was applied closer to the near end to produce high shear forces in the damaged region and distance 40 in. was the possible closest location loading frame can be anchored based on the spacing of the anchor holes in the strong floor. For Specimen 7, load was applied at mid span, 132 in. away from the near end of the specimen (Figure 4.17). Load was applied monotonically until failure, through a single Enerpac hydraulic actuator capable of applying 1,000-kip load. Actuator was anchored to a stiff loading frame which was anchored to the strong floor through 4–1 3/4 in. DYWIDAG threaded rods of to resist the uplift when applying the load. Load applied by the actuator was transferred to the specimen through a spreader beam of width 16 in. Proper contact between the spreader beam and top flange of the specimen was crucial and was ensured through Hydro-Stone gypsum cement mortar. Spreader beam was bolted to the top flange of the specimen to ensure stability throughout the experiment.

Specimens were simply supported on an assembly of a half-cylindrical steel section and a steel block on top as shown in Figure 4.19. The width of the steel block was 8 in. and the half-cylindrical steel section on the bottom allowed rotation of the steel block and specimen on top during testing simulating a girder in actual

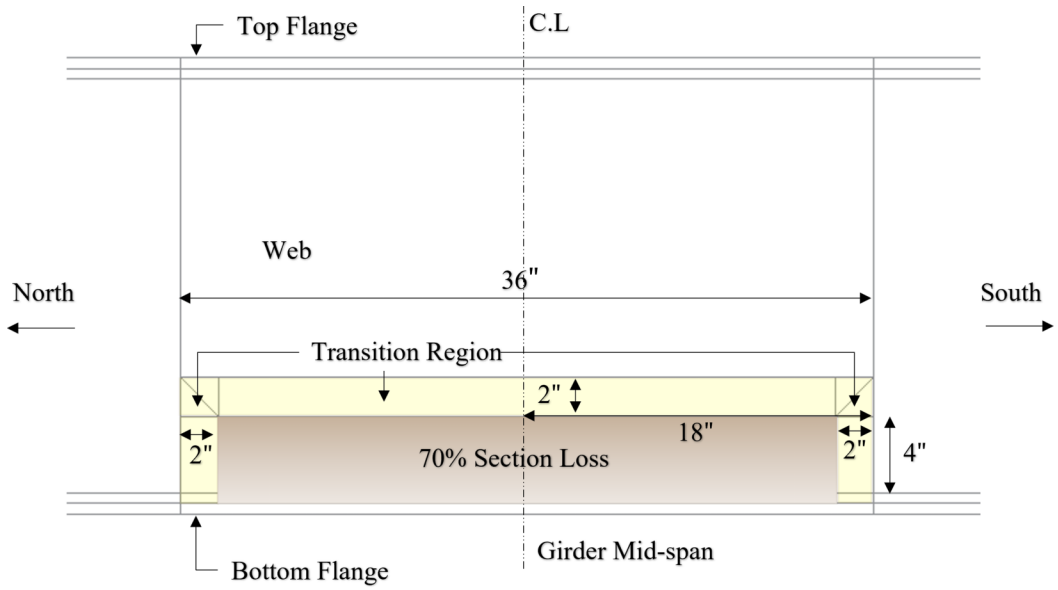

Figure 4.13 Specimen 7 section loss profile.

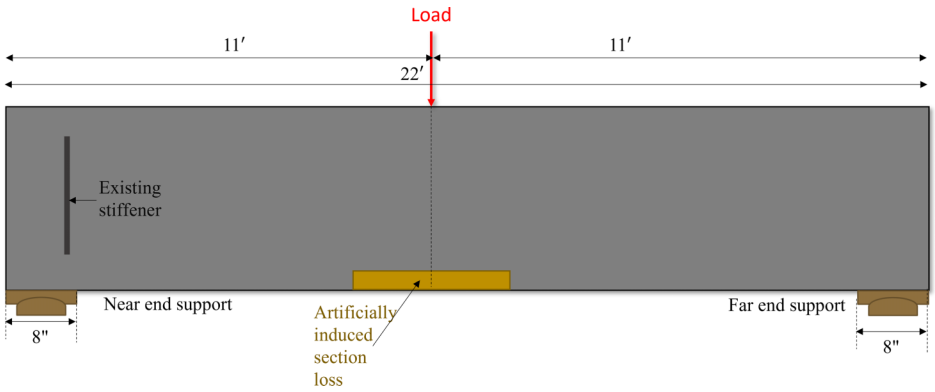

Figure 4.14 Specimen 7 geometry and corrosion details.

TABLE 4.2
Material properties of specimens

Specimen	F_y (ksi)	F_u (ksi)
Specimen 1	46	72
Specimen 2	45	66
Specimen 3	51	73
Specimen 4	51	72
Specimen 5	46	69
Specimen 6	48	72
Specimen 7	48	70

in-service bridge. For Specimen 1–6, assembly of half-cylindrical steel section and steel block at the near end sits on an assembly of built-up section anchored to the strong floor. At the far end, assembly of half-cylindrical steel section and steel block was supported on a bearing plate which sits on a concrete support block. For Specimen 7, assembly of half-cylindrical steel section and steel block sits on a bearing plate which sits on a concrete support block. Hydro-stone gypsum cement mortar was used to ensure proper contact between bearing plate and top surface of concrete block, and between bottom surface of concrete block and strong floor.

While in service, the girders were composite with the deck slab through shear studs. Concrete deck provides lateral restraint to the top flange of the girders. However, full scale test is performed on the specimen without concrete deck and therefore lateral restraints were provided to ensure specimen failure either in shear or bearing without torsional buckling or twisting. Lateral restraint was provided through two bracing frames and loading frame (Figure 4.20 through Figure 4.22). Each bracing frame assembly consists of bottom fixture, two columns, three channel sections, two angle sections as shown in. Angle section of each bracing frames restrain the lateral movement of top flange and bottom flange at the near end support and at 76 in. from the near end. To ensure a frictionless between angle section and flanges of the specimen, Teflon sheets have been provided. Bottom fixture of each bracing

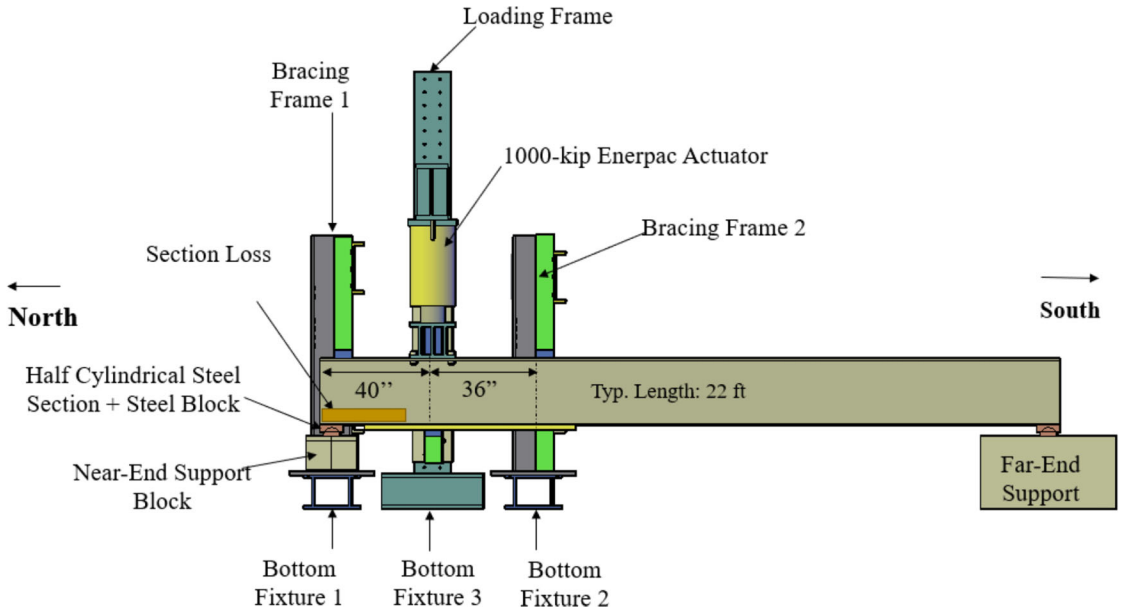

Figure 4.15 Specimen 1–6 test setup schematic view.

Figure 4.16 Photograph of test setup for Specimens 1–6.

frame was anchored to the strong floor through 2–1 1/2 in. DYWIDAG threaded rods. At the loading frame, a set of angle sections anchored to the column of the stiff loading frame restrain the lateral movement of the top and bottom flange of the specimens.

4.5 Instrumentation Layout

The National Instruments (NI) Data Acquisition System was used to collect the data with the test program developed in a graphical programming environment LabView 2012. Throughout testing such parameters as displacement (vertical and out-of-plane), force and strain were recorded. Strain gauges (SG) produced by Tokyo Measuring Instruments Lab (Gauge type YEFLAB-5, resistance $120 \pm 0.5\ \Omega$) were attached to the prepared surface using CN adhesive. For measuring both vertical and out-of-plane displacement, string potentiometers (SP) produced by UniMeasure, Inc. were used. The stroke for string potentiometers varied from 5 and 10 in. and the string potentiometers with the larger stroke (10 in.) were installed at the locations where the large displacements were expected and to prevent damaging the sensors. Finally, to record displacements less than 1 in., displacement transducers (DT) produced by BEI Duncan Electronics with the stroke of 1 in. were utilized. Omega DPG-4000 Series pressure transducer was connected to the DAQ to record the exerting pressure by the actuator on the specimen, to obtain the force applied to a specimen, the pressure values were multiplied by the effective area of the actuator. Strain gauges and string potentiometer layouts varied depending on the type of failure that was expected: web crippling (Specimens 4, 5), shear buckling (Specimens 1, 2, 3, 6), or flexural yielding (Specimen 7). The data obtained was used to validate the FE models developed in Abaqus and to analyze the type of occurred failure.

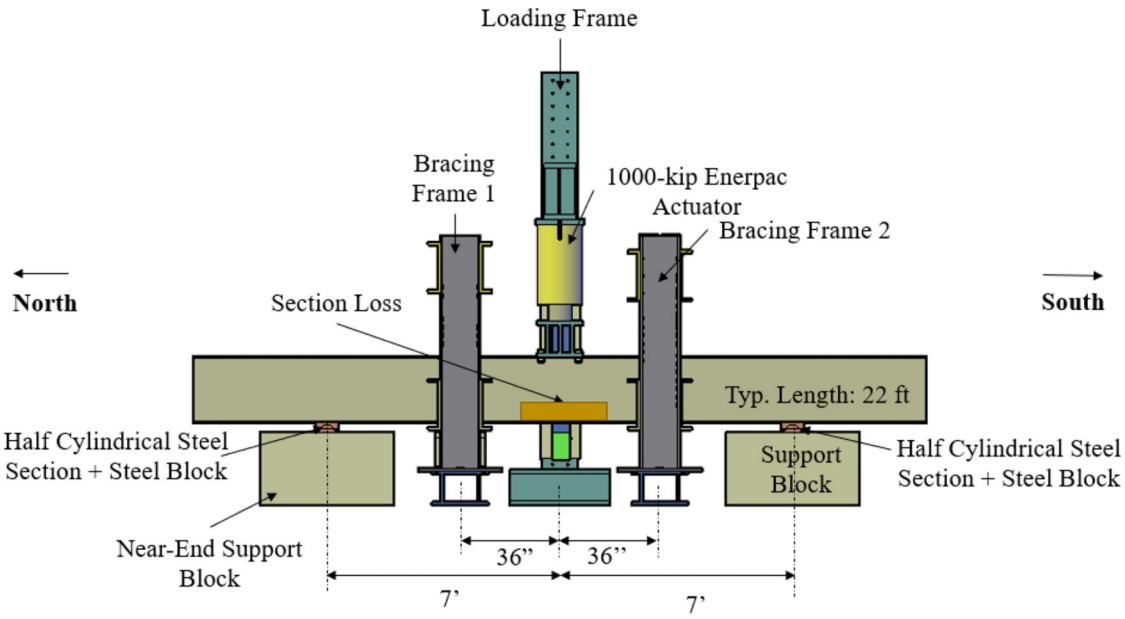

Figure 4.17 Specimen 7 test setup schematic view.

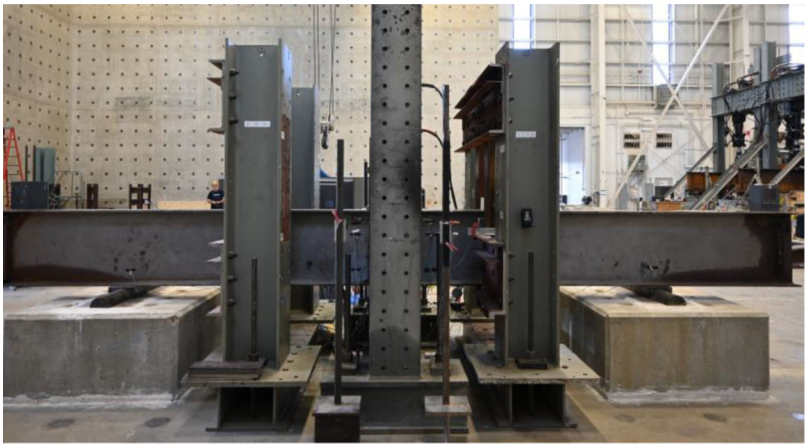

Figure 4.18 Photograph of test setup for Specimen 7.

4.5.1 Specimens 1–6

Typical sensor layouts for Specimens 1–6 are presented in Figure 4.23 to Figure 4.27. The number of strain gauges installed on Specimens 1, 2, 3, and Specimen 6 was 27. Specimens 4 and 5 had a total of 31 strain gauges. For specimens that were expected to fail in web crippling (Specimen 4 and 5) four strain gauges (SG30–SG33) were installed at the web's bottom above the bearing region (Figure 4.13) where web local crippling was expected to occur. Strain gauge (SG 18) was provided on the bottom flange right below the loading point (40″ from the girder end). Strain gauge rosette was provided on both sides of the girder web to record the principal strains.

In the area of the highest interest for Specimen 4 and Specimen 5 (above the bearing, underneath the existing stiffener), where web crippling was expected to occur, two string potentiometers (SP14 and SP15) were installed. For Specimens 1, 2, 3, and 6, out-of-plane (OOP) displacements expected due to web shear buckling were recorded by SP9 and SP6 installed at the center of the web (Figure 4.15). In addition, DT7 was provided to measure any vertical displacement of the built-up support at its centerline (Figure 4.27). Finally, displacement transducers (DT1-DT6) were provided to measure the OOP displacements of the lateral bracings.

4.5.2 Specimen 7

For the last large-scale test, Specimen 7, a separate sensor layout was developed due to different expected failure mode and corresponding test setup configuration. Sensor layout for Specimens 7 is presented in Figure 4.28 to Figure 4.31, with the yellow rectangle indicating the region with section loss profile. Specimen 7 was provided with 27 strain gauges and 12 string potentiometers measuring vertical and out-of-plane

Figure 4.19 Simple support at the girder end.

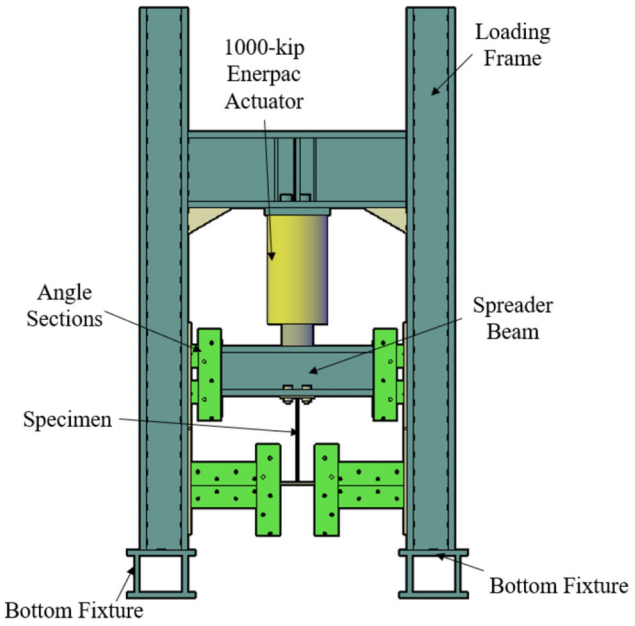

Figure 4.20 Loading frame.

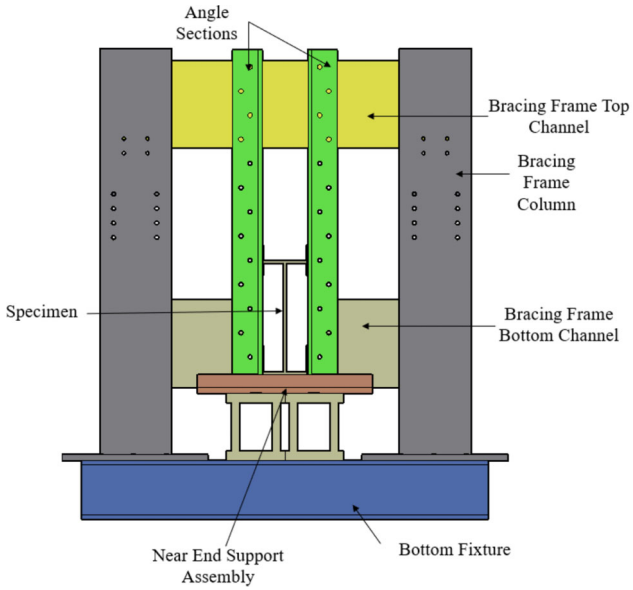

Figure 4.21 Bracing frame at near-end support.

displacements. String potentiometers (SP1-SP3) were provided to measure the vertical displacement during the test and connected to the bottom flange at the loading region. OOP displacements in the web at the loading region were measured by string potentiometers (SP4-SP8) installed on East and (SP9-SP13) West side of the specimen. Since Specimen 7 was expected to fail in flexural yielding, strain gauges (SG27-SG29) were attached to the bottom flange to record the strains and yielding (Figure 4.29). Also, strain gauges (SG1, SG13, SG14, SG26) at the web's bottom are just above the supports (both north and south end). Strain gauge rosette was provided on both sides of the specimen's web for principal strains.

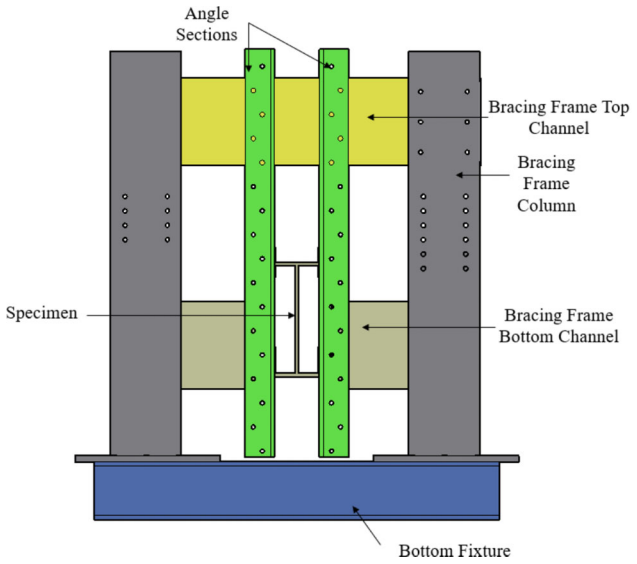

Figure 4.22 Bracing frame at other locations.

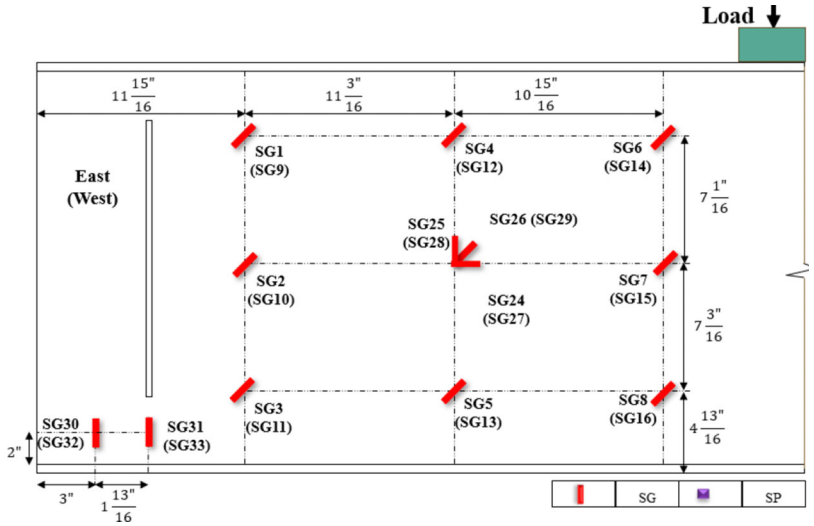

Figure 4.23 Strain gauge layout (side elevation): Specimens 1–6.

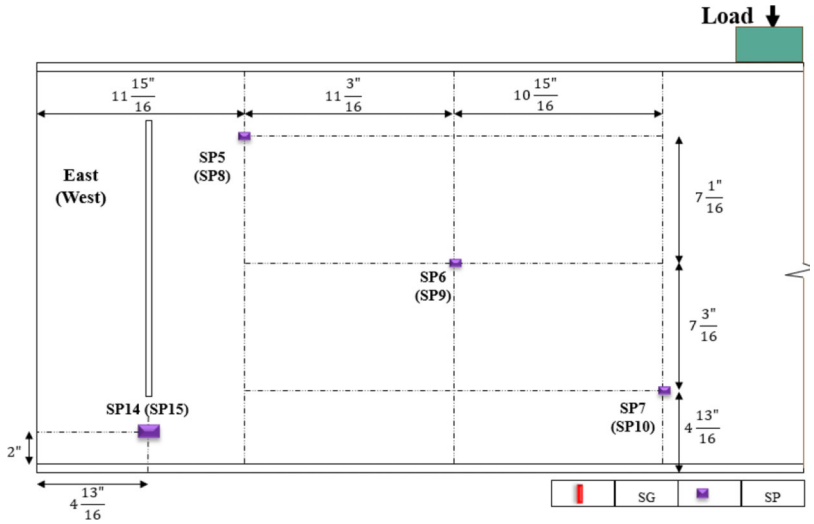

Figure 4.24 Displacement sensor layout (side elevation): Specimens 1–6.

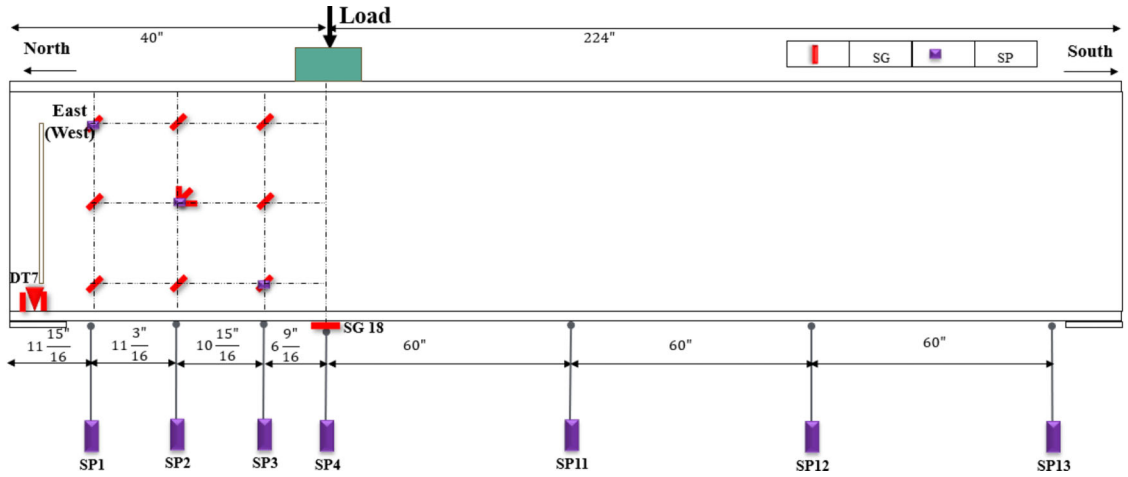

Figure 4.25 Displacement sensor layout (side elevation): Specimens 1–6.

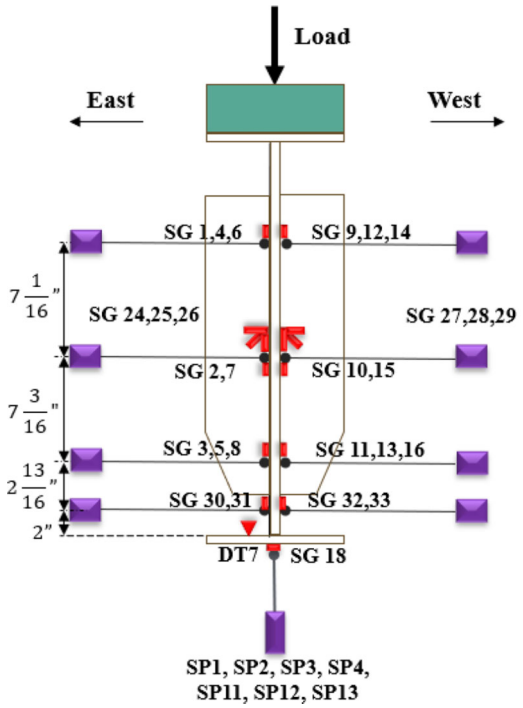

Figure 4.26 Strain gauge layout (front elevation): Specimens 1–6.

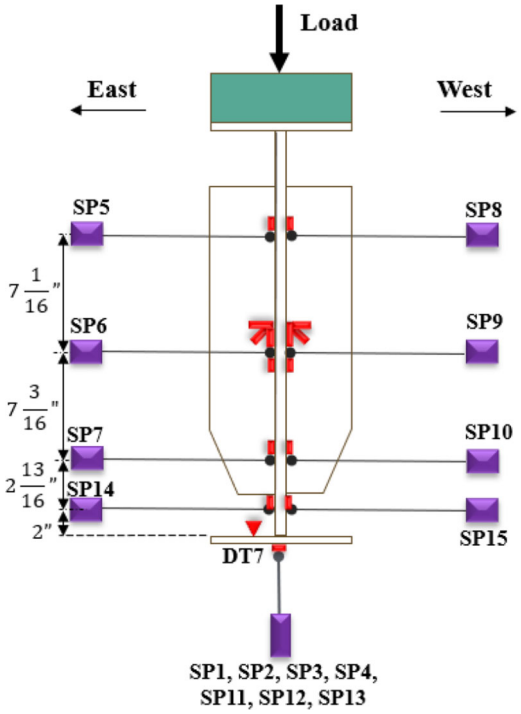

Figure 4.27 Displacement sensor layout (front elevation): Specimens 1–6.

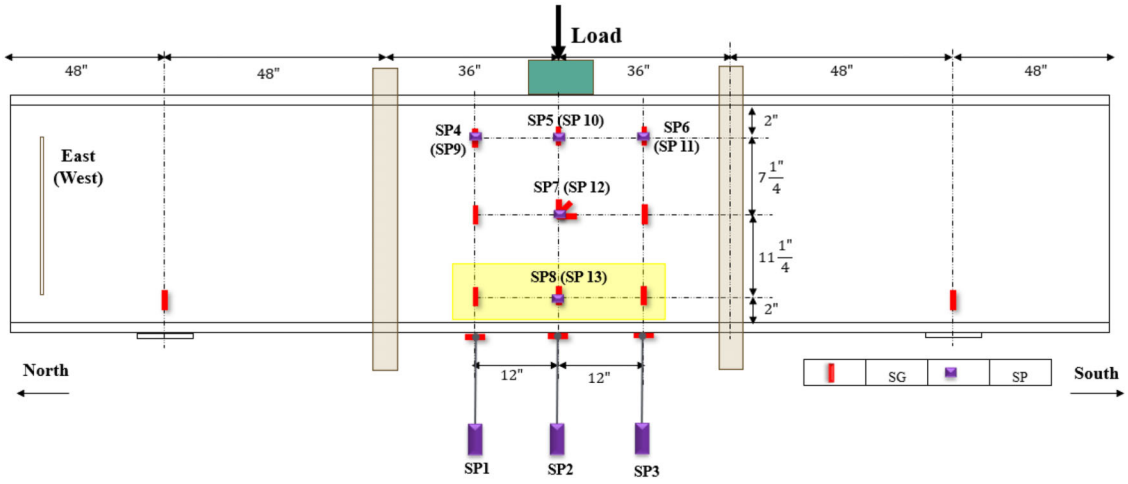

Figure 4.28 Displacement sensor layout (side elevation): Specimen 7.

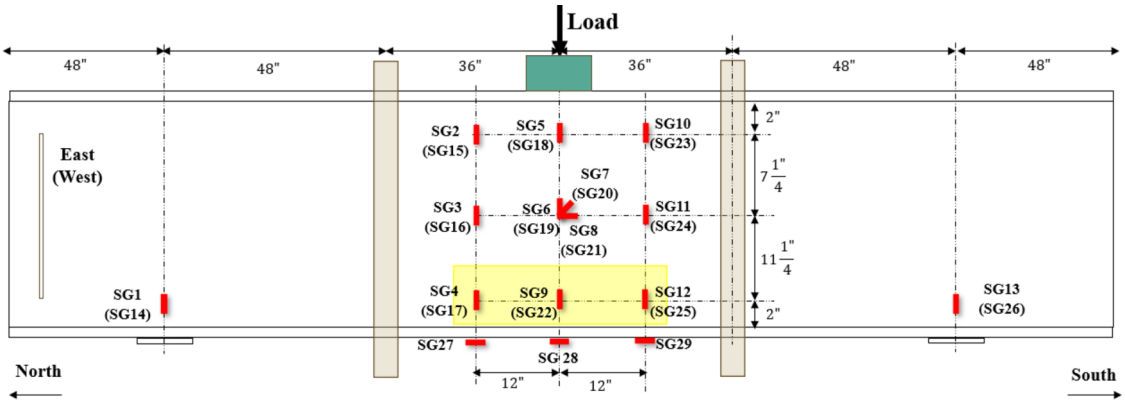

Figure 4.29 Strain gauge layout (side elevation): Specimen 7.

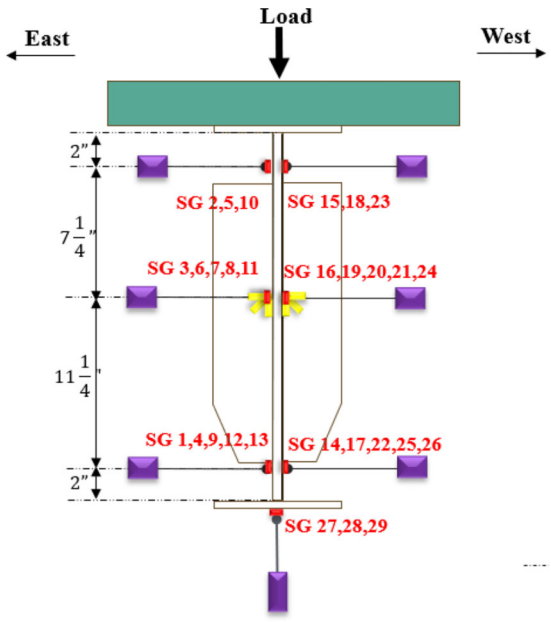

Figure 4.30 Strain gauge layout (front elevation): Specimen 7.

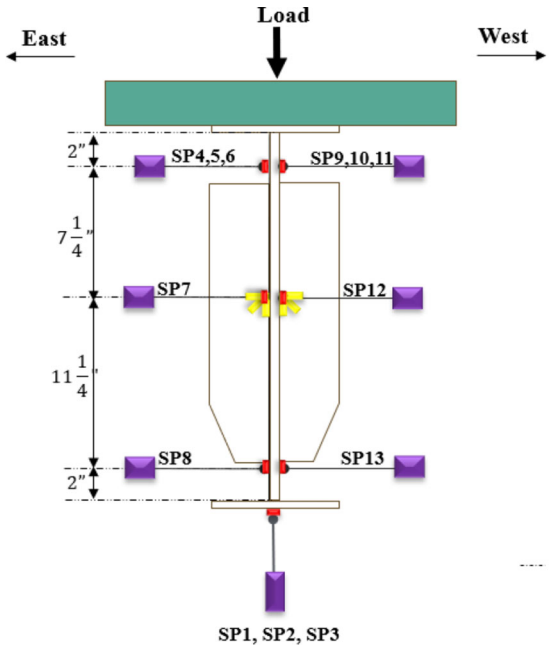

Figure 4.31 Displacement sensor layout (front elevation): Specimen 7.

5. EXPERIMENTAL RESULTS AND OBSERVATIONS

This section presents the experimental data and observations for all seven experiments performed. Experimental data presented in this section includes deformed shape, applied load-displacement relationships and load-strain relationships, and damage progression. The vertical displacement presented below was recorded by a string potentiometer at the bottom flange just below the loading point. Web out-of-plane (OOP) displacement was recorded by string potentiometer at several locations on the web on both sides. The sensor layout for each specimen is shown in Section 4.5. However, the web OOP displacement at critical locations, such as the center of the web panel and web OOP displacement just above the near-end support, is presented below. The strain gauge presented below includes data from the bottom flange just below the loading point and strain gauge data from the strain rosette.

5.1 Specimen 1

Specimen 1 was a W24 × 68 rolled steel section with very light corrosion. Contour plots of section loss measurements are shown in Figure 3.3. Existing partial depth stiffeners used to connect the diaphragm beam to the girder during in-service were retained during the experiment. In addition, full-depth stiffeners were provided at the bearing and loading regions. Overall, Specimen 1 represents a stiffened girder with section loss at the bottom of the web. Section loss in the stiffeners was not considered in this study. Specimen 1 eventually failed in shear buckling, and the maximum applied load was 292 kips. The load was applied through an Enerpac actuator with a capacity of 1,000 kip, and the applied load was obtained through a pressure transducer connected to the data acquisition system. The load was applied onto the top flange at 40 in. from the corroded end Specimen 1. A schematic of the test setup of Specimen 4 is shown in Figure 4.15, and the instrumentation layout is provided in Section 4.5. At the loading region, strain data and vertical displacement data of the outer face of the cover plate were recorded by strain gauge SG18 and string potentiometer SP4, respectively. As the loading was applied, Specimen 1 had vertical displacement with an initial stiffness of 662.88 kip/in up to an applied load of 250 kips. After 250 kips, a gradual reduction in stiffness was observed, but stiffness was still positive up to the maximum applied load of 292 kips. After this, Specimen 1 underwent large vertical displacement without further load increase.

From Figure 5.2, it was observed that Specimen 1 did not have any significant OOP displacement up to an applied load of 250 kips. However, the web began to buckle after the load exceeded 250 kips, as observed by the increase in the web OOP displacement. Large web OOP displacement occurred at the center of the web panel (SP6) and the maximum web OOP displacement recorded by SP6 was 1.7 in.

From the strain gauge data, yielding was first initiated in the web bottom at the corroded end at about 213 kips followed by other locations in the web. Most of the web underwent yielding at the applied load of 272 kips. From Figure 5.3(a), yielding in the bottom flange began at about 290 kips, followed by large strains in the bottom flange. Eventually, Specimen 1 failed in web shear buckling, and the maximum applied load was 292 kips. The experiment was terminated following large OOP displacements and strains in Specimen 1.

In summary, Specimen 1 failed in shear buckling (Figure 5.1), and the maximum applied load was 292 kips with maximum shear at the corroded end of the girder being equal to 251 kips. The nominal shear strength of a W24 × 68 section without any section loss is 272 kips (Appendix A). Comparing the nominal shear strength with the maximum shear force in the bearing during the test, we observe a loss of 8%.

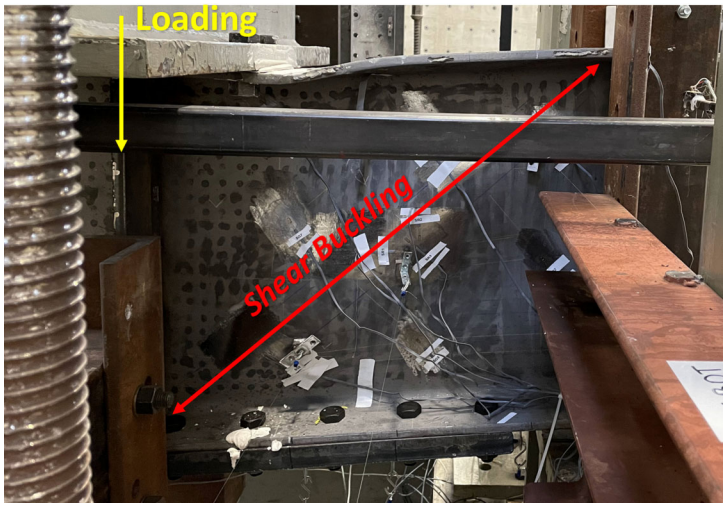

Figure 5.1 Specimen 1 web shear buckling.

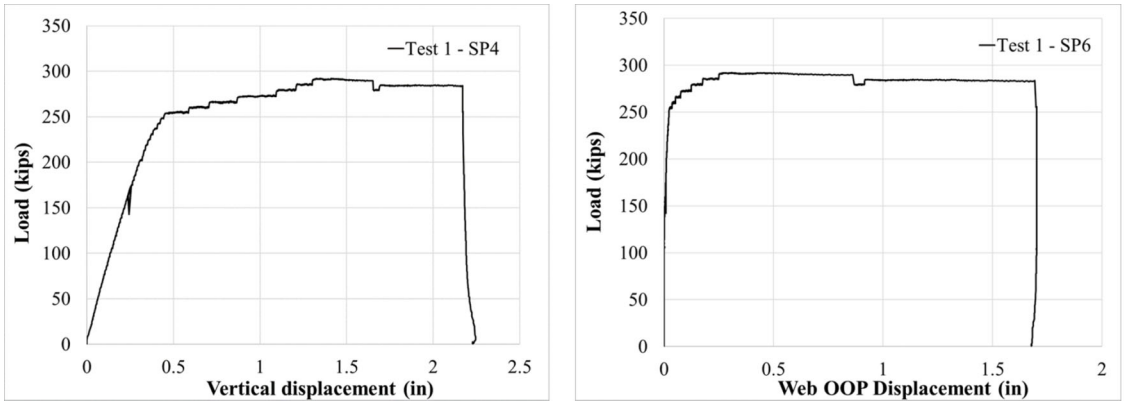

Figure 5.2 Specimen 1 load-displacement relationship.

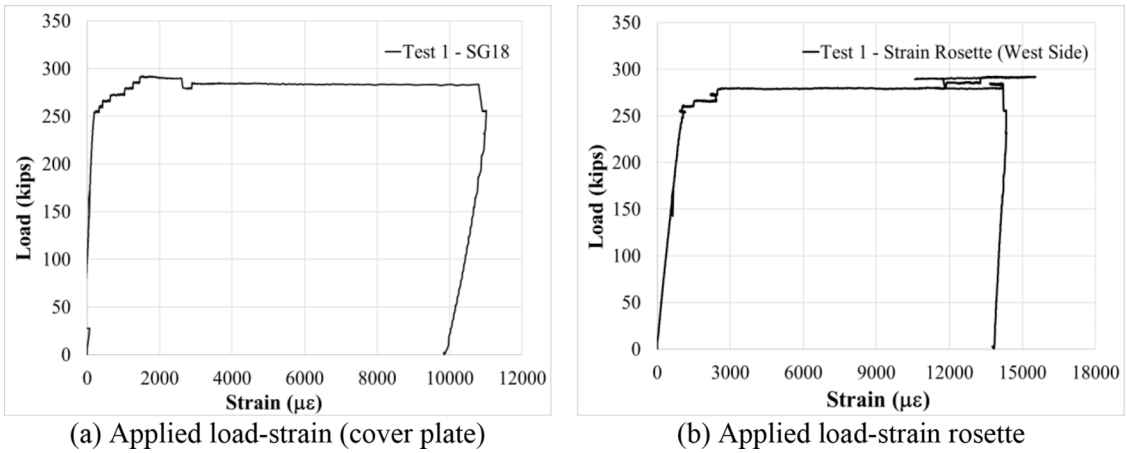

(a) Applied load-strain (cover plate) (b) Applied load-strain rosette

Figure 5.3 Specimen 1 load-strain relationship

5.2 Specimen 2

Specimen 2 was a W24 × 68 rolled steel section with corrosion at the web's bottom at the girder end. Contour plots of section loss measurements are shown in Figure 3.5. Existing partial depth stiffeners used to connect the in-service diaphragm beam to the girder were retained during the experiment. In addition, full-depth stiffeners were provided at the bearing and loading regions. Overall, Specimen 2 represents a stiffened girder with section loss at the bottom of the web. Section loss in the stiffeners was not considered in this study. Specimen 2 eventually failed in shear rupture, and the maximum applied load was 240 kips. The load was applied through an Enerpac actuator of capacity 1,000-kip, and the applied load was measured through a pressure transducer connected to the data acquisition system. The load was applied onto the top flange at 40 in. from the near end (corroded end) of Specimen 2. A schematic of the test setup of Specimen 4 is shown in Figure 4.15, and the instrumentation layout is provided in Section 4.5. Strain data and vertical displacement data of the outer face of the cover plate at the loading point was recorded by strain gauge SG18 and string potentiometer SP4 and shown below in Figure 5.8 and Figure 5.9. As the loading was applied, Specimen 2 had a vertical displacement with an initial stiffness of 683.88 kip/in up to an applied load of 188 kips. After 188 kips, a gradual reduction in stiffness was observed, but stiffness was still positive up to the maximum applied load of 240 kips. After this, Specimen 2 underwent vertical displacement without further load increase.

From Figure 5.8(b), it was observed that Specimen 2 did not have any significant OOP displacement up to an applied load of 227 kips. OOP displacement recorded by SP6 at the center of the web panel after 227 kips was less than 0.15 in. From the strain gauge data, yielding was initiated at the bottom of the web (SG16 and SG5) at about 210 kips followed by other locations in the web. From Figure 5.9(a), yielding in the bottom flange began at about 225 kips, followed by large strains in the bottom flange and the web. Eventually, Specimen 2 failed in web shear rupture, and the maximum applied

Figure 5.4 Specimen 2 before test.

Figure 5.5 Specimen 2 shear rupture at the web bottom (East side).

Figure 5.6 Specimen 2 shear rupture at the web bottom (West side).

Figure 5.7 Specimen 2 deformed stiffener.

load was 240 kips. The experiment was terminated following shear rupture at the web bottom (Figures 5.4 through 5.7) and large vertical displacements of Specimen 2.

5.3 Specimen 3

Specimen 3 was a W24 × 68 rolled steel section with corrosion at the web's bottom. Contour plots of section loss measurements are shown in Figure 3.8. Existing partial depth stiffeners used to connect the in-service diaphragm beam to the girder were retained during the experiment. In addition, full-depth stiffeners were provided at the bearing and loading regions. Overall, Specimen 3 represents a stiffened girder with section loss at the bottom of the web. Section loss in the stiffeners was not considered in this study. Specimen eventually failed in shear web buckling, and the maximum applied load was 275 kips. The load was applied through an Enerpac actuator of capacity 1,000-kip, and the applied load was measured through a pressure transducer connected to the data acquisition system. The load was applied onto the top flange at 40 in. from the near end (corroded end) of Specimen 3. A schematic of the test setup of Specimen 4 is shown in Figure 4.15, and the instrumentation layout is provided in Section 4.5. At the loading region, strain data and vertical displacement data of the outer face of the bottom flange were recorded by strain gauge SG18 and string potentiometer SP4 and presented below. From Figure 5.12(a), Specimen 3 had a vertical displacement as the load increased with an initial stiffness of 465.45 kip/in. After 215 kips, a gradual reduction in stiffness was observed, but stiffness was still positive up to the maximum applied load of 275 kips. After this, Specimen 3 underwent large vertical displacement without further load increase.

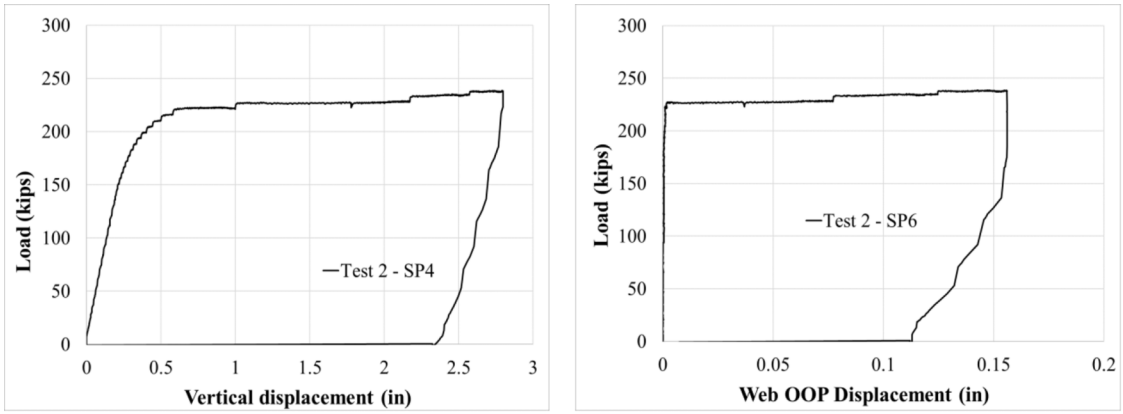

(a) Applied load-vertical displacement (b) Applied load-web OOP

Figure 5.8 Specimen 2 load-displacement relationship.

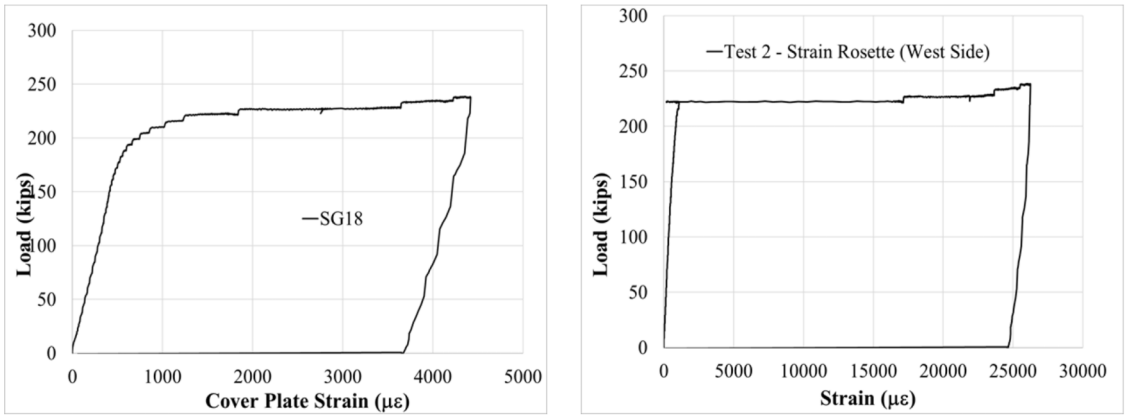

(a) Applied load-strain (bottom flange) (b) Applied load-strain rosette

Figure 5.9 Specimen 2 load-strain relationship.

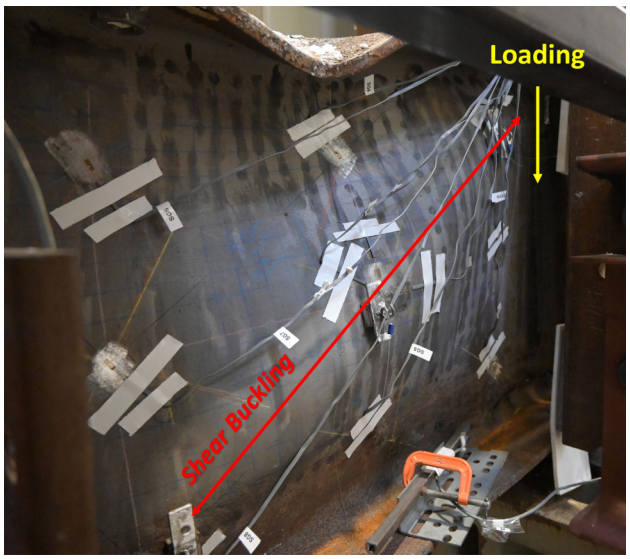

Figure 5.10 Specimen 3 web shear buckling.

Figure 5.11 Specimen 3 web condition at the support.

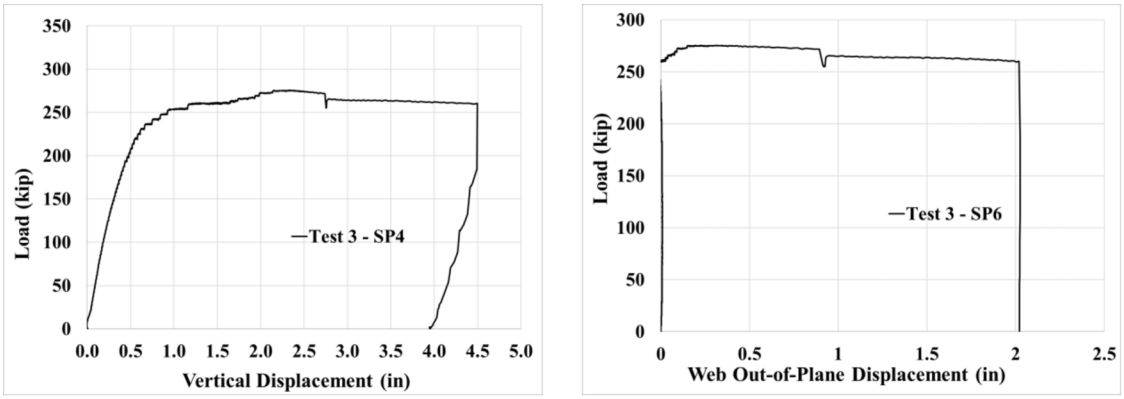

(a) Applied load-vertical displacement (b) Applied load-web OOP

Figure 5.12 Specimen 3 load-displacement relationship.

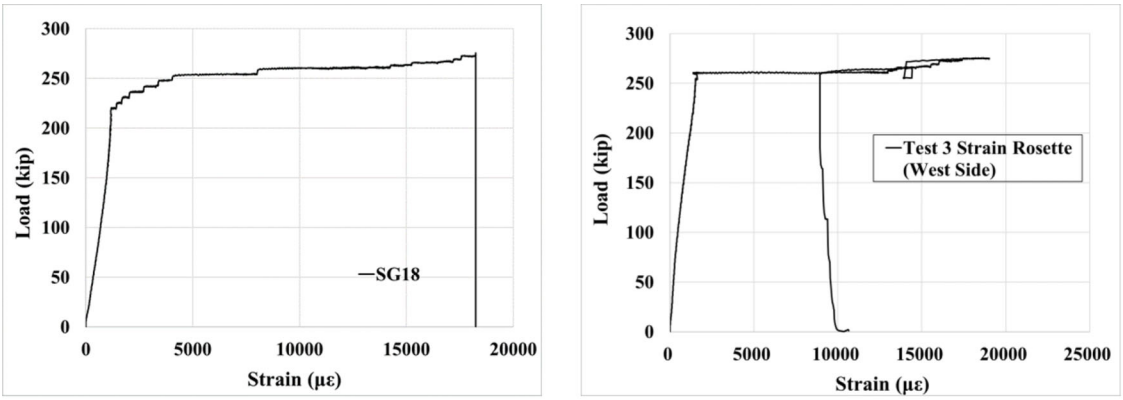

(a) Applied load-strain (bottom flange) (b) Applied load-strain rosette

Figure 5.13 Specimen 3 load-strain relationship.

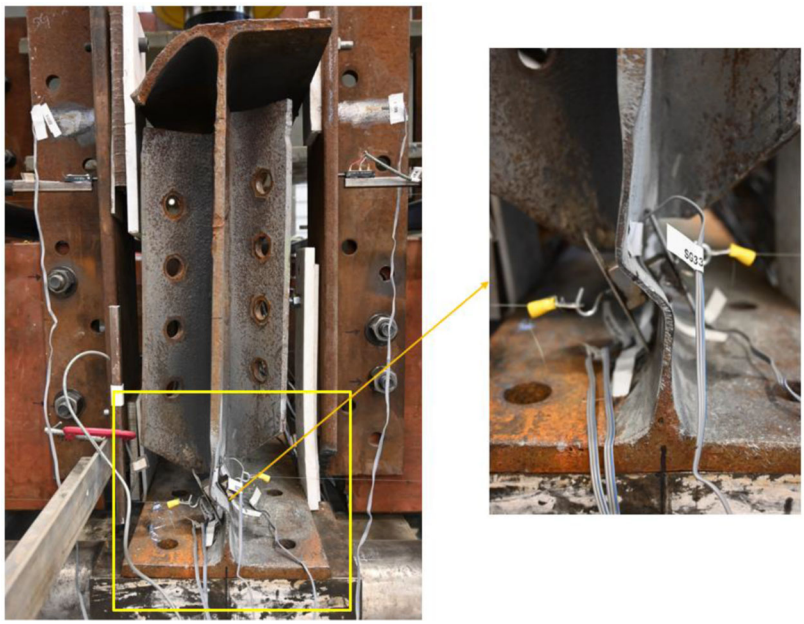

Figure 5.14 Specimen 4 web local crippling.

From Figure 5.12(b), it was observed that Specimen 3 did not have any significant OOP displacement up to an applied load of 260 kips. The web began to buckle after the load exceeded 260 kips, as observed by the gradual increase in the web OOP displacement. At the ultimate load of 275 kips, large web OOP displacement occurred at the center of the web panel at the location of SP6. The maximum web OOP displacement recorded by SP6 was 2 in. at the experiment's termination.

From the strain gauge data, it was observed that yielding was first initiated at the bottom of the web at the loading region (SG16 and SG5) at 200 kips. From Figure 5.13(a), yielding in the bottom flange began at about 225 kips, followed by gradual yielding in the other locations of the web. After the load exceeded 260 kips, large strains occurred in the bottom flange and the web. Eventually, Specimen 3 failed in web shear buckling, and the maximum applied load was 275 kips. The experiment was terminated following large OOP displacements in the web and tilting of the top flange.

In summary, Specimen 3 failed in shear buckling (Figure 5.10 and Figure 5.11), and the maximum applied load was 275 kips with maximum shear at the corroded end of the girder being equal to 236 kips. The nominal shear strength of a W24 × 68 section without any section loss is 301 kips (Appendix A). Comparing the nominal shear capacity with the maximum shear force in the bearing during the test, we observe a loss of 22%.

5.4 Specimen 4

Specimen 4 was a W24 × 68 rolled steel section with very light corrosion in the web. At the girder end, the bottom of the web was purposefully made thinner through grinding to induce the section loss profile discussed in detail in Section 3.3. The contour plot of the thickness measurements of the web of Specimen 4 is shown in Figure 3.15. In addition, existing partial depth stiffeners used to connect the in-service diaphragm beam to the girder were retained during the experiment. Overall, Specimen 4 represents a girder with partial depth transverse stiffeners and section loss at the bottom of the web. Specimen 4 eventually failed in web local crippling and the maximum applied load was 48 kips. The load was applied through an Enerpac actuator of capacity 1,000-kip, and the applied load was measured through a pressure transducer connected to the data acquisition system. The load was applied onto the top flange at 40 in. from the near-end or corroded end of Specimen 4. A schematic of the test setup of Specimen 4 is shown in Figure 4.15, and the instrumentation layout is provided in Section 4.5. At the loading region, strain data and vertical displacement data of the outer face of the bottom flange recorded by strain gauge SG18 and string potentiometer SP4 were shown below. From Figure 5.15(a), Specimen 4 underwent vertical displacement as the load was increased with an initial stiffness of 498.67 kip/in up to the maximum applied load of 48 kips. After the maximum applied load, Specimen 4 underwent vertical displacement with a negative stiffness.

From Figure 5.15(b), Specimen 4 began to have OOP displacement in the section loss region (SP14) at an applied load of 20 kips. This OOP displacement at SP14 continued to increase with load up to the maximum applied load of 48 kips. After 48 kips, large web OOP displacement was observed in the section loss region without increase in the applied load. Specimen 4 did not have the further load-carrying capacity and underwent the web local crippling failure at the bottom of the web. No OOP displacement was observed at the strain rosette (SP6) location until the maximum applied load of 48 kips. OOP displacement recorded at the strain rosette after 48 kips was very small and less than 0.02 in., which could be due to the global OOP displacement of Specimen 4 at failure. The maximum web OOP displacement recorded by SP14 was 0.14 at the experiment's termination.

From observing the strain data, yielding in the steel occurred only in the section loss region but did not occur either at the bottom flange at the loading region or at the strain rosette location during the entire test. From Figure 5.16, yielding initiated first in the section loss region at an applied of 17 kips and continued to take up the load without any reduction in stiffness up to an applied load of 26 kips. Softening in stiffness was observed in the strain data once the applied load

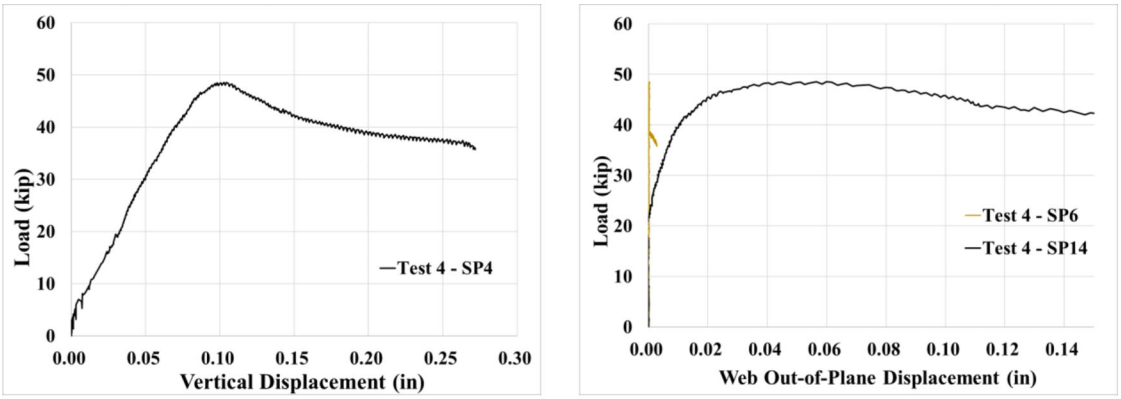

(a) Applied load-vertical displacement (b) Applied load-web OOP

Figure 5.15 Specimen 4 load-displacement relationship.

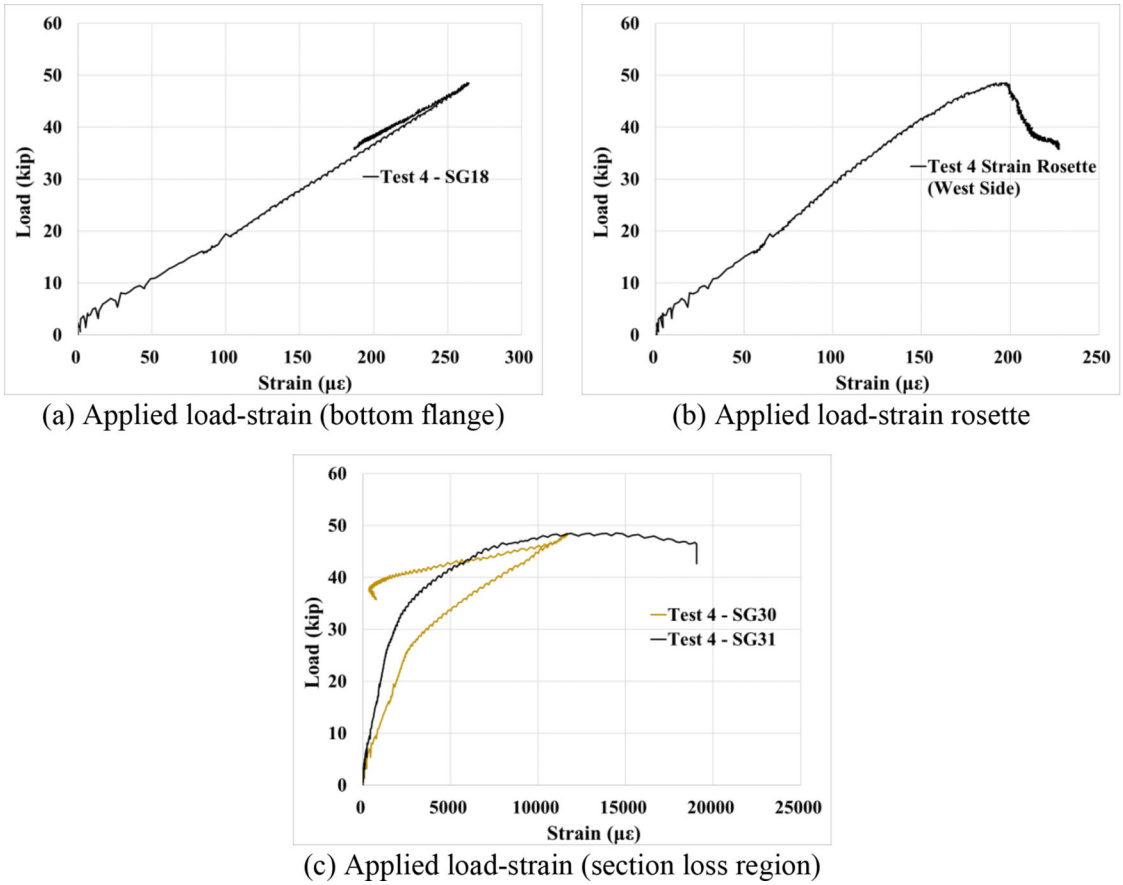

(a) Applied load-strain (bottom flange)

(b) Applied load-strain rosette

(c) Applied load-strain (section loss region)

Figure 5.16 Specimen 4 load-strain relationship.

exceeded 26 kips but continued to take up load up to the peak load 48 kips. From strain gauge data recorded by SG31, large strains were observed after the peak load in the section loss region. Also, strain reversal was observed in the strain gauge SG31 due to the web local crippling. The experiment was terminated after large OOP displacements and strains in the web in the section loss region.

In summary, Specimen 4 failed in web local crippling at an applied load of about 48 kips with maximum shear at the corroded end of the girder being equal to 41 kips. The nominal bearing capacity of a W24 × 68 section without any section loss is 168 kips (Appendix A). Comparing the nominal bearing capacity with the maximum shear force in the bearing during the test, we observe a loss of 75%.

5.5 Specimen 5

Specimen 5 was a W24 × 68 rolled steel section with very light corrosion. Severe section loss was induced artificially, and the section loss profile was discussed in detail in Section 3.3. Existing partial depth stiffeners were removed and ground to smooth. Overall, Specimen 5 represents an unstiffened girder with section loss at the bottom of the web. Specimen ultimately failed in web local crippling at an applied load of 25 kips. The load was applied through an Enerpac actuator of capacity 1,000-kip, and the applied load was obtained through a pressure transducer connected to the data acquisition system. The load was applied on the top flange at 40 in. from the near-end support of Specimen 5 through a spreader beam. At the loading region, strain data and vertical displacement data of the outer face of the bottom flange recorded by strain gauge SG18 and string potentiometer SP4 is shown below. From Figure 5.18(a), Specimen 5 underwent vertical displacement as the load was increased with an initial stiffness of 517 kip/in up to the maximum applied load of 25 kips. After the maximum applied load, Specimen 5 underwent large vertical displacement without further load carrying capacity.

From Figure 5.18(b), Specimen 5 had an increasing OOP displacement in the section loss region (SP14) with increasing load up to an applied load of 25 kips. After this, large web OOP displacement was observed in the section loss region without any increase in the applied load. Specimen 5 did not have any further load-carrying capacity, and the web local crippling at the bottom of the web was clearly visible. No OOP displacement was observed at the location of the strain rosette (SP6) until the maximum applied load of 25 kips. OOP displacement recorded at the strain rosette after 25 kips was very small and less than 0.02 in., which could be due to the global OOP displacement of

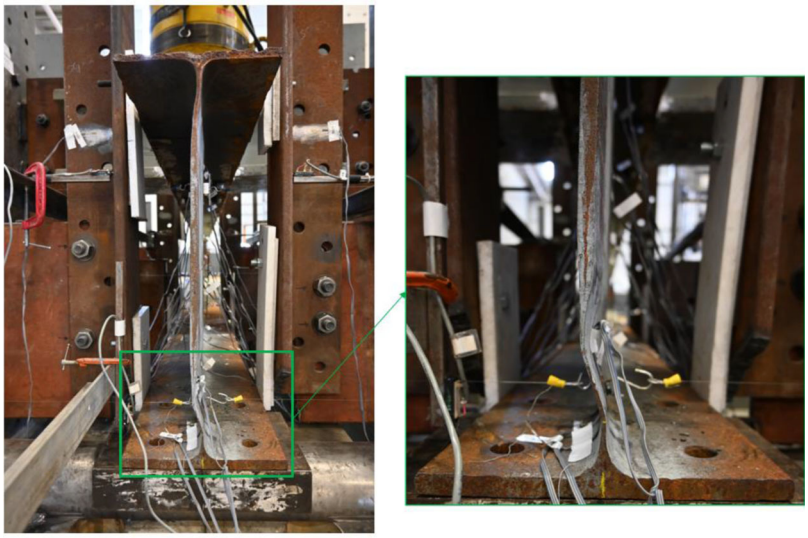

Figure 5.17 Specimen 5 web local crippling.

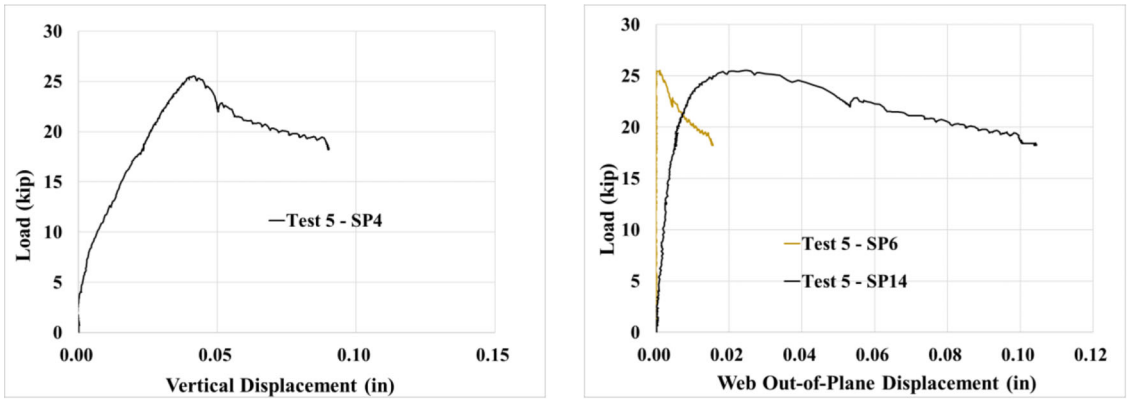

(a) Applied load-vertical displacement (b) Applied load-web OOP

Figure 5.18 Specimen 5 load-displacement relationship.

the specimen as web local crippling failure occurred in the section loss region. Maximum web OOP displacement recorded by SP6 was 0.015 in., while web OOP displacement recorded by SP14 was 0.1 at the experiment's termination.

From the strain data at the strain rosette location and strain gauge on the bottom flange, it was observed that no yielding of the web occurred at the location of the strain rosette and the bottom flange as shown in Figure 5.19. However, steel in the section loss region had undergone yielding. Yielding was initiated in the section loss region at an applied of 17 kips and continued to take up load up to 25 kips. Once the applied load exceeded 25 kips, large strains occurred in the section loss region without any further load carrying capacity. The experiment was terminated following large OOP displacements and strains in the web in the section loss region.

In summary, Specimen 5 failed in web local crippling (Figure 5.17) at an applied load of about 25 kips with maximum shear at the corroded end of the girder being equal to 21 kips. The nominal bearing capacity of a W24 × 68 section without any section loss is 159 kips (Appendix A). Comparing the nominal bearing capacity with the maximum shear force in the bearing during the test, we observe a loss of 87%.

5.6 Specimen 6

Specimen 6 was a stiffened steel girder with both pre-existing partial depth stiffeners and full depth stiffeners at the bearing and loading region. The specimen had section loss at the bottom end of the web, and details of the section loss in Specimen 6 were provided in Section 4.2.5. Specimen 6 ultimately failed in shear web buckling at an applied load of 271 kips. The load was applied load through the Enerpac actuator of capacity 1,000-kip, and the applied load was obtained through a pressure transducer connected to the data acquisition system. The load was applied on the top flange at 40 in. from the near-end support of Specimen 6 through a spreader beam. At the loading region, strain data and vertical displacement data of the outer face of the bottom flange recorded by strain gauge SG18 and

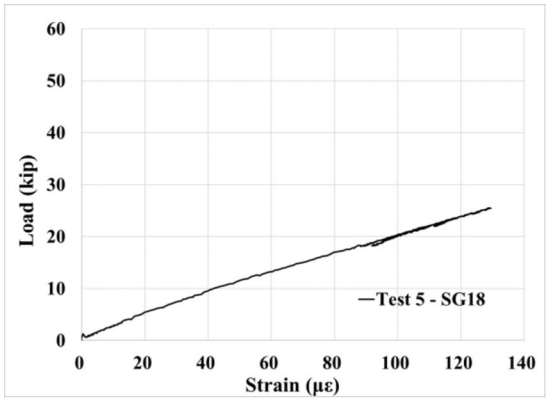

(a) Applied load-strain (bottom flange)

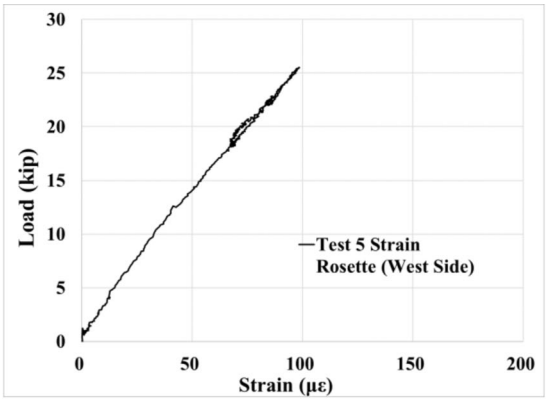

(b) Applied load-strain rosette

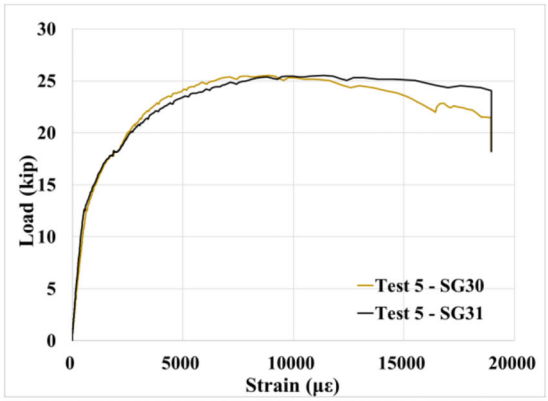

(c) Applied load-strain (section loss region)

Figure 5.19 Specimen 5 load-strain relationship.

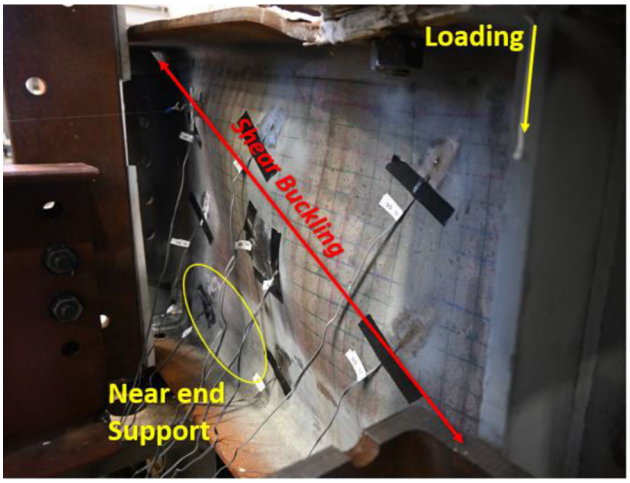

Figure 5.20 Specimen 6 web shear buckling.

Figure 5.21 Specimen 6 OOP web displacement at the bottom (SP14).

string potentiometer SP4 were shown below. From Figure 5.22(a), Specimen 6 had a vertical displacement as the loading was applied with an initial stiffness of 533 kip/in up to an applied load of 215 kips, after which softening behavior was observed. After 215 kips, a gradual reduction in stiffness was observed, but stiffness was still positive, accompanied by large vertical displacements up to the maximum applied load of 271 kips. After this, Specimen 6 continued to undergo vertical displacement with a negative stiffness.

From Figure 5.22(b), it was observed that Specimen 6 did not have any significant OOP displacement up to an applied load of 250 kips. The web began to buckle after the load exceeded 250 kips, as observed by the increase in the web OOP displacement. Large web OOP displacement occurred at the center of the web panel (SP6), as shown in Figure 5.20, in comparison to the bottom of the web just above the near-end support

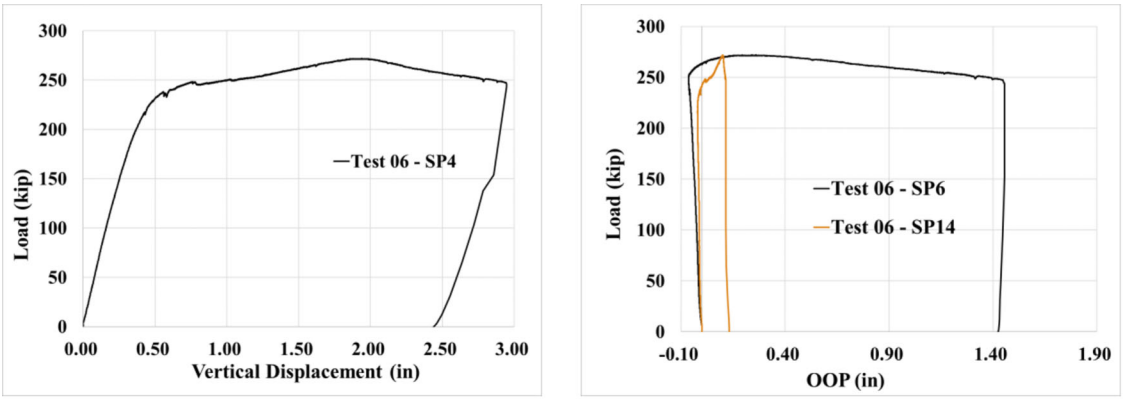

Figure 5.22 Specimen 6 load-displacement relationship.

(SP14), as shown in Figure 5.21. The maximum web OOP displacement recorded by SP6 was 1.4 in., while the web OOP displacement recorded by SP14 was 0.1 in.

Yielding was initiated in the bottom flange just below the loading point at an applied load of 200 kips. As the load increased, the bottom flange continued to take up stress beyond yield stress without any reduction in stiffness, and the yielding region continued to spread to the surrounding web region. Most of the web underwent yielding before the applied load reached 250 kips. Additionally, once the load exceeded 250 kips, large strains occurred at the bottom flange and at the center of the web panel (strain rosette), as shown in Figure 5.24. Finally, the specimen continued to take up load up to 270 kips before failure in web shear buckling. From 250 kip to 270 kip, the observed strength gain of about 20 kip at the end could be due to the post-buckling shear strength of the web. The experiment was terminated following large OOP displacements in the web and tilting of the top flange.

In summary, the specimen failed in shear buckling at an applied load of about 270 kips with maximum shear at the corroded end of the girder being equal to 232 kips. The nominal shear strength of a W24 × 68 section without any section loss is 284 kips (Appendix A). Comparing the nominal shear capacity with the maximum shear force in the bearing during the test, we observe a loss of 18%.

5.7 Specimen 7

Specimen 7 was a W24 × 68 rolled steel section and in contrast to the rest of the specimens, section loss was in the bottom of the web at the mid span. Contour plots of section loss measurements are shown in Figure 3.21. Existing partial depth stiffeners used to connect the in-service diaphragm beam to the girder were retained. Overall, Specimen 7 represents unstiffened girder with section loss at the bottom of the web at midspan. Specimen eventually failed in flexure at an applied load of 184 kips. The load was applied through an Enerpac actuator of capacity 1,000-kip, and the applied load was obtained through a pressure transducer connected to the data acquisition system. The load was applied through a spreader beam onto the top flange at 132 in. from the near-end support of Specimen 7. At the loading region, strain data and vertical displacement data of the outer face of the bottom flange recorded by strain gauge SG28 and string potentiometer SP2 are shown below. As the loading was applied, Specimen 7 had a vertical displacement with an initial stiffness of 499.51 kip/in up to an applied load of 160 kips. After 160 kips, a gradual reduction in stiffness was observed, but stiffness was still positive, accompanied by large vertical displacements up to the maximum applied load of 184 kips. After this, Specimen 7 underwent vertical displacement without further load increase.

From Figure 5.26(b) it was observed that Specimen 7 did not have any significant OOP displacement up to an applied load of 180 kips. OOP displacement recorded by SP4, SP5, and SP7 at the loading region was very small and less than 0.1 in. After 180 kips, extensive OOP displacement was recorded at the loading region.

Yielding was initiated at the outer face of the bottom flange at about 160 kips followed by the bottom of the web with section loss. At this load, large strains were observed in the bottom flange along with reduced stiffness as shown in Figure 5.27. At about 180 kips, the top of the web around the loading region began to yield but the center of the web remained within yield strain. Eventually, the experiment was terminated following large strains in the bottom flange and vertical displacements of the specimen and tilting of the top flange along with the spreader beam.

In summary, Specimen 7 failed in flexural yielding (Figure 5.25), and the maximum applied load was 184 kips, with maximum shear at both ends of the girder being equal to 92 kips. Shear force corresponding to the nominal flexural strength of a W24 × 68 section without any section loss is 101 kips (Appendix A). Comparing this theoretical shear force with the maximum shear force at the bearing during the test, we observe a loss of 9%.

Figure 5.23 Tilting of top flange and spreader beam.

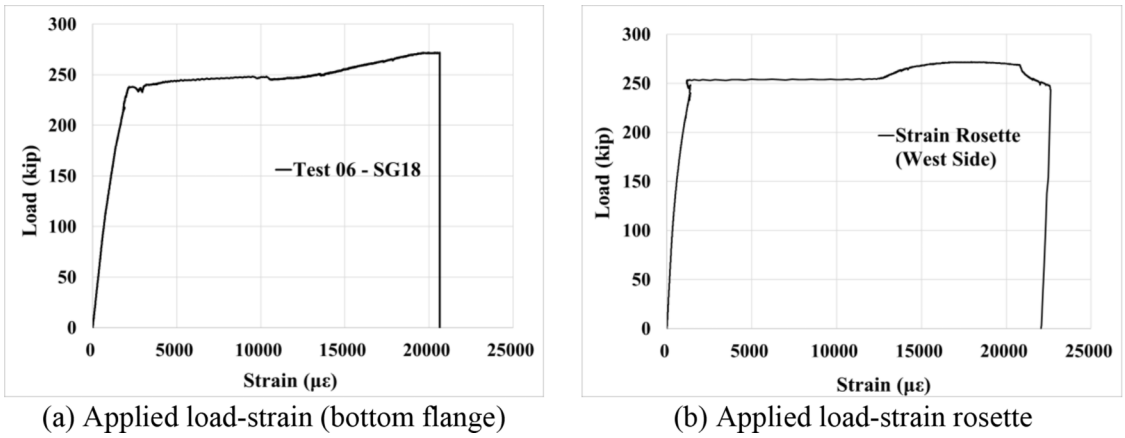

Figure 5.24 Specimen 6 load-strain relationship.

Figure 5.25 Specimen 7 flexural yielding.

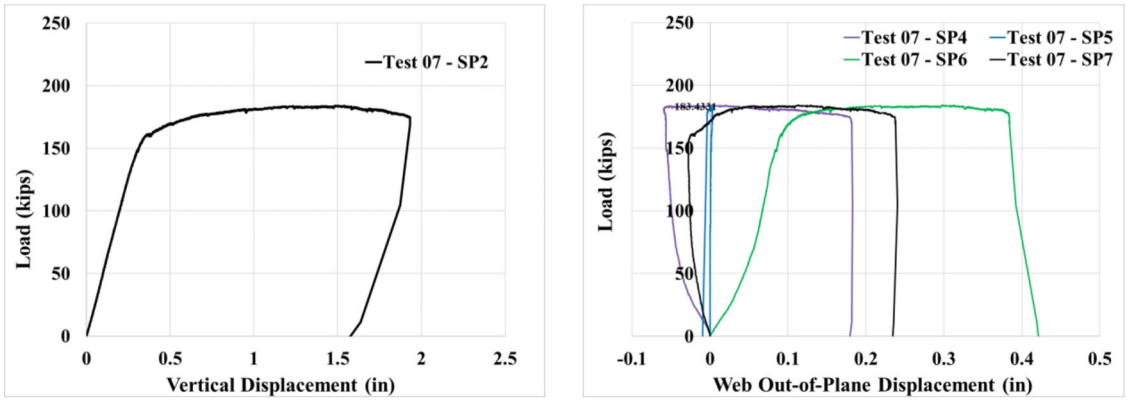

(a) Applied load—vertical displacement (b) Applied load—web OOP

Figure 5.26 Specimen 7 load-displacement relationship.

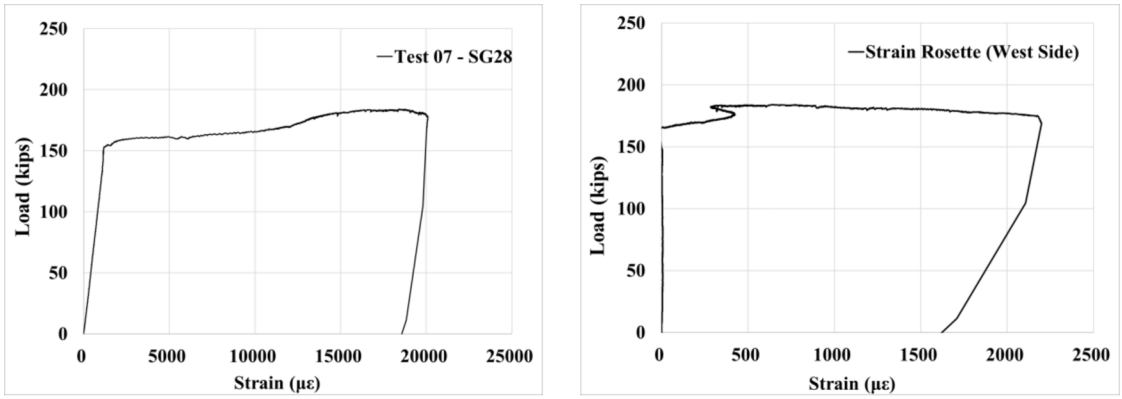

(a) Applied load-strain (bottom flange) (b) Applied load-strain rosette

Figure 5.27 Specimen 7 load-strain relationship.

TABLE 5.1
Summary of experimental results and decrease in capacity due to corrosion

Specimen No.	Residual Capacity of Corroded Girder (kip)	Capacity According to AISC-360-16 for Non-Corroded Girder (kip)	Strength Reduction (%)	Failure Mode
Specimen 1	251	272	8	Shear buckling
Specimen 2		Experiment Terminated Due to Rupture		
Specimen 3	236	301	22	Shear buckling
Specimen 4	41	168	75	Web crippling
Specimen 5	21	159	87	Web crippling
Specimen 6	232	284	18	Shear buckling
Specimen 7	92	101	9	Flexural yielding

5.8 Summary of Experimental Results

The summary of all seven large-scale tests conducted is presented below in Table 5.1. As presented, unstiffened girders (Specimens 4, 5) failed in web crippling, girders with full-depth transverse stiffeners (Specimens 1, 3, 6) failed in shear buckling. Specimen 7 represented the special case where the load was applied at the center to study the effect of corrosion at a midspan on a flexural capacity. The experimentally measured ultimate strength of each specimen was compared with the equations provided below from AISC 360-16 (Equation 5.1 to Equation 5.4) for estimating bearing capacity, shear capacity and flexural capacity for non-damaged girders. The applicable equation for bearing capacity will depend on the distance from the girder end at which compressive load is applied, as well as the ratio of the bearing length over full nominal depth of the member (over or less than 0.2). For example, if the compressive load is applied at a distance greater or equal than half of the nominal depth of the member (Specimen 7) and the ratio of $l_b/d > 0.2$, the equations

for web local yielding and web local crippling provided below will be used, with the lowest value governing. As it could be observed from Table 5.1, corrosion has the biggest impact on unstiffened girders—Specimens 4 and 5, which failed in web crippling and had reduction in capacity of 75% and 87%, respectively.

Web Local Yielding $R_n = F_{yw} t_w (2.5k + l_b)$ (Eq. 5.1)

Web Local Crippling

$$R_n = 0.8 t_w^2 \left[1 + 3\left(\frac{l_b}{d}\right)\left(\frac{t_w}{t_f}\right)^{1.5}\right]\sqrt{EF_{yw} t_f / t_w Q_f} \quad \text{(Eq. 5.2)}$$

Shear Capacity $V_n = 0.6 F_y A_w C_{v1}$ (Eq. 5.3)

Flexural Capacity $M_n = F_y Z_x$ (Eq. 5.4)

6. FINITE ELEMENT MODELING

This chapter describes the finite element models developed to simulate the conducted large-scale experiments using the commercially available software ABAQUS. The objective of developing the finite element models was to accurately capture the failure modes, shear, and bearing capacity of the specimens as well as strains, and displacement behavior observed in the experiments. After benchmarking the finite element models to the experimental results, two parametric studies were performed, modeling different corrosion scenarios, and investigating the effect of section loss on the residual bearing and shear capacity.

6.1 Modelling Approach

Seven full-scale experiments were performed, and the experimental results are presented in Section 5. All the specimens in the experiments are of the same size and length, W24 × 68 rolled steel section, 22 ft. in length. Finite element models were developed for the full-scale model of the specimen tested. Models were developed using shell elements (S4R) which consists of 4-node doubly curved thin or thick shell elements utilizing reduced integration and hourglass control. Section loss in the web was modeled by reducing the thickness of the steel section in the corroded region and is discussed in detail in Section 6.2. A fine mesh size of 0.5 in. was adopted for a distance of 8 ft. from the near end. The remaining 14 ft. of the model consisted of a coarse mesh of size 1 in.

Boundary conditions were defined at the near-end support, far-end support, and lateral bracings. Near-end (corroded region) of the specimen was restrained in all the translational degrees of freedom (U1 = U2 = U3 = 0), while the far-end of the specimen was restrained only in the vertical direction (U2 = 0) and free to move in the horizontal plane. At the locations of the lateral bracings, the top and bottom flanges were restrained in the OOP direction (U1 = 0). Loading was applied to the top flange at a distance of 40 in. from the near end of the girder. To model the behavior of the top flange region, where the spreader beam transfers the applied load by the actuator to the top flange of the specimen, a kinematic coupling constraint was defined, constraining the degrees of freedom to the reference node where the loading is applied in the model.

Static RIKS analysis method was used for the analyses presented below except for Specimen 7. Static RIKS analysis is an arc-based technique suitable for predicting the behavior of structures undergoing large deformations and instability. Specimens except Specimens 2 and 7 underwent failure either by shear buckling or web local crippling, and this analysis method was appropriate for predicting these behaviors. Specimen seven failed in flexural yielding and explicit dynamic analysis method was used for predicting the behavior of Specimen 7. Specimen two underwent failure by shear rupture, which is outside this study's scope; therefore, benchmarked numerical model for Specimen 2 was not developed.

Material property input for each specimen in ABAQUS was obtained from the tensile test of the steel coupons, fabricated from each specimen, and tested per ASTM E8 (2022). It is important to input true (not engineering) stress-strain curves to the ABAQUS, therefore, based on conducted material tests and using equations provided below (Equation 5.5 to Equation 5.7), true stress, true stain and plastic strain were calculated.

$$\varepsilon_{true} = \ln(1 + \varepsilon_{eng}) \quad \text{(Eq. 6.1)}$$

$$\sigma_{true} = \sigma_{eng}(1 + \varepsilon_{eng}) \quad \text{(Eq. 6.2)}$$

$$\varepsilon_p = \varepsilon_{true} - \frac{\sigma_{true}}{E} \quad \text{(Eq. 6.3)}$$

6.2 Section Loss Modelling

Modeling the section loss in the finite element model is critical for residual capacity prediction. One way of modeling the section loss involves assigning the remaining thickness of the web measured at every 1 in. × 1 in. grid on the web in the corroded region. Thickness measurements were obtained utilizing ultrasonic thickness gauge and is discussed in detail in Section 3.1. Thickness can be assigned manually if the corroded region is small. For large, corroded regions it is recommended to automate thickness assignment utilizing Python scripting.

However, a different approach was adopted to model the section loss and this approach consists of two steps. First step involves defining the section loss region in the web. Length of the corroded region (CL) and height of the corroded region (CH1) and (CH2) was utilized to define the section loss region in the web. The second step involves assigning the effective thickness of the web

in the section loss region. Effective thickness of the web was calculated averaging the measured thickness in the region above the bearing length up to a height of 3 in. above the k region. Calculated effective thickness was assigned to the entire section loss region defined in the first step. Section loss in all the specimens have been modelled using this second approach.

6.3 Results From Finite Element Analysis

Finite element models predicted the failure modes and capacities that align well with the experimental results. The maximum variation in the results between the finite element model prediction and experimental results is 8%, with the minimum variation being equal to 0.2%. Behavior predicted up to the peak load matches accurately the experimental results. The finite element models of Specimen 5 and Specimen 6 have been used for the parametric study discussed in Section 7.

6.3.1 Finite Element Model Results for Specimens 1, 3, and 6

The finite element model of Specimens 1, 3, and 6 predicted web shear buckling failure mode, the same failure mode that was observed in the experiment. The comparison of the deformed shape predicted by the finite element model and experiment for Specimens 1, 3, and 6 is made in Figure 6.1, Figure 6.2, and Figure 6.3, respectively. Predicted capacity by the finite element model for Specimens 1, 3, and 6 were 301 kips, 293 kips, and 260 kips, and variation with test results was 3%, 6.6%, and 4%, respectively, as shown in Table 6.1.

From the comparison of force-vertical displacement relationship made in Figure 6.4, the finite element model of Specimen 3 and 6 predicts the behavior before and after the peak load that is very close to the test results. However, the behavior predicted by the finite element model for Specimen 1 after 250 kips differs from the test results. The model did not predict the reduction in stiffness observed in the experiment, and this difference might be due to the modeling of the bolted connection of the cover plate. Nevertheless, the initial stiffness and peak strength predicted by the numerical model correspond well with the experimental results.

6.3.2 Finite Element Model Results for Specimens 4 and 5

The finite element model of Specimens 4 and 5 predicted failures in web local crippling, the same

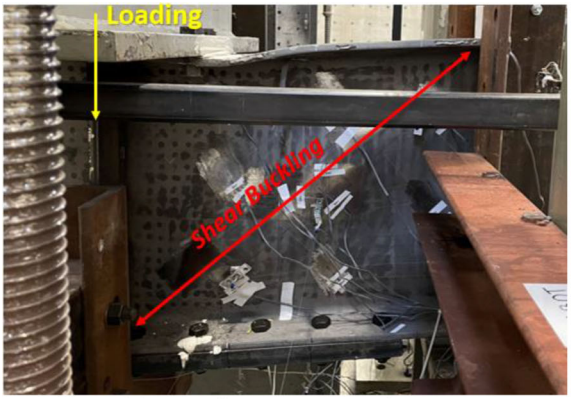

(a) Specimen 1–experiment

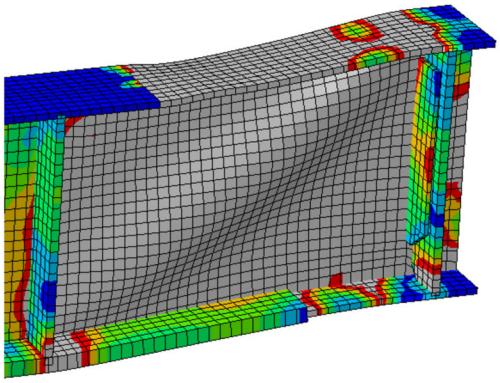

(b) Specimen 1–finite element model

Figure 6.1 Comparison of deformed shape of Specimen 1.

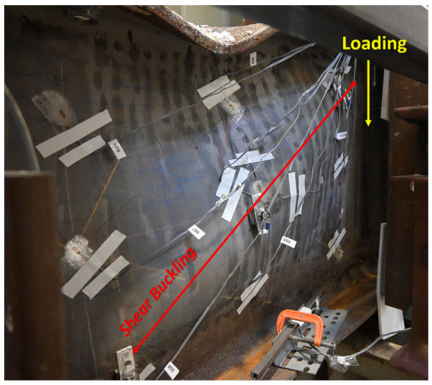

(a) Specimen 3–experiment

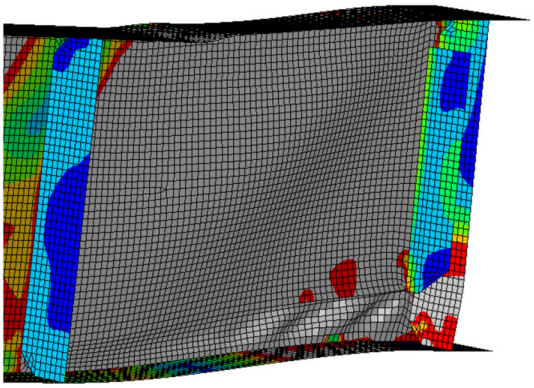

(b) Specimen 3–finite element model

Figure 6.2 Comparison of the deformed shape of Specimen 3.

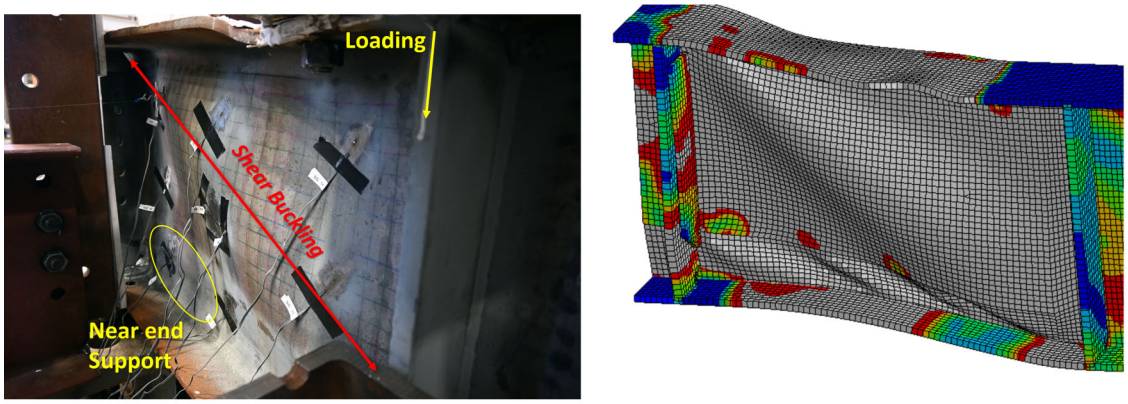

(a) Specimen 6–experiment (b) Specimen 6–finite element model

Figure 6.3 Comparison of the deformed shape of Specimen 6.

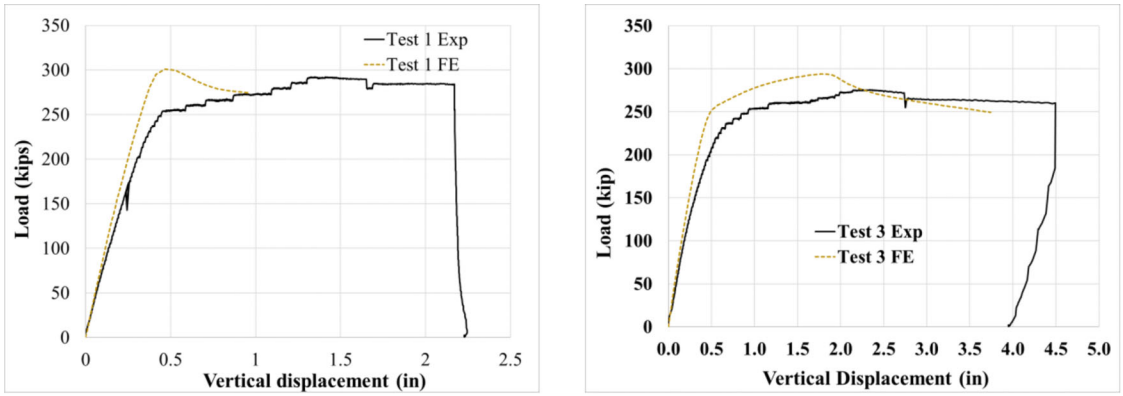

(a) Specimen 1 (b) Specimen 3

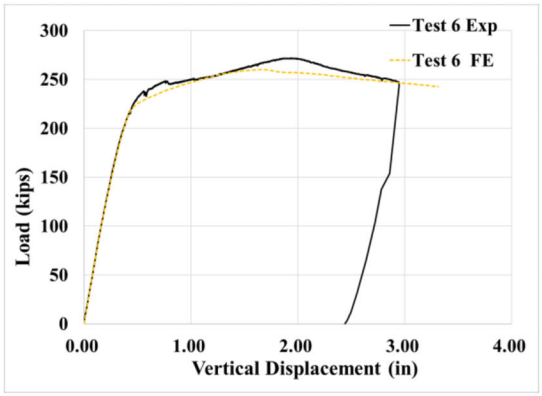

(c) Specimen 6

Figure 6.4 Comparison of the load-displacement relationship for Specimens 1, 3, and 6.

TABLE 6.1
Comparison of the capacities for Specimens 1, 3, and 6

Specimen	Experiment	Finite Element Model	Variation (%)
Specimen 1	292 kips	301 kips	3
Specimen 3	275 kips	293 kips	6.6
Specimen 6	271 kips	260 kips	4.3

TABLE 6.2
Comparison of capacities for Specimens 4 and 5

Specimen	Experiment	Finite Element Model	Variation (%)
Specimen 4	48 kips	47 kips	2.6
Specimen 5	25 kips	25 kips	0.2

(a) Specimen 4–experiment

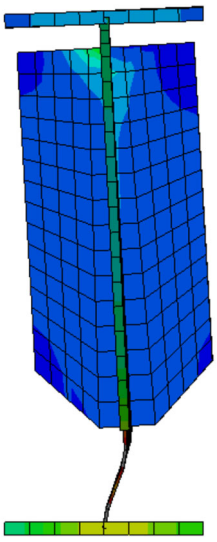

(b) Specimen 4–finite element model

Figure 6.5 Comparison of the deformed shape of Specimen 4.

(a) Specimen 5–experiment

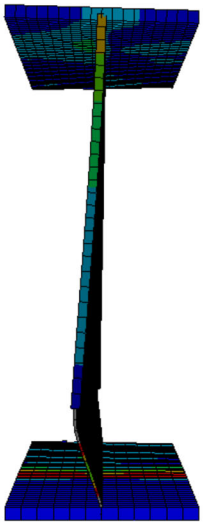

(b) Specimen 5–finite element model

Figure 6.6 Comparison of the deformed shape of Specimen 5.

failure mode observed in the experiment. The comparison of the deformed shape predicted by the finite element model and experiment for Specimen 4 and 5 is made in Figure 6.5 and Figure 6.6, respectively. Predicted capacity by the finite element model for Specimens 4 and 5 were 47 kips and 25 kips, and variation with the test results was 2.6% and 0.2%, as shown in Table 6.2.

From the comparison of the force-vertical displacement relationship made in Figure 6.7, the finite element model of Specimens 4 and 5 predicts the behavior before buckling that is very close to the test results. However, difference is observed in the post-buckling behavior in both models.

6.3.3 Finite Element Model Results for Specimen 7

The finite element model of Specimen 7 predicted failure in flexural yielding, which is the same failure mode observed in the experiment. The comparison of the deformed shape predicted by the finite element model and experiment for Specimen 7 is made in Figure 6.8. Predicted capacity by the finite element model for Specimen 7 is 25 kips with the variation with the test results of approximately 8%, as shown in Table 6.3.

From the comparison of the force-vertical displacement relationship made in Figure 6.9, the finite element model of Specimen 7 predicts the behavior before peak load, up to 160 kips, that is close to the test results.

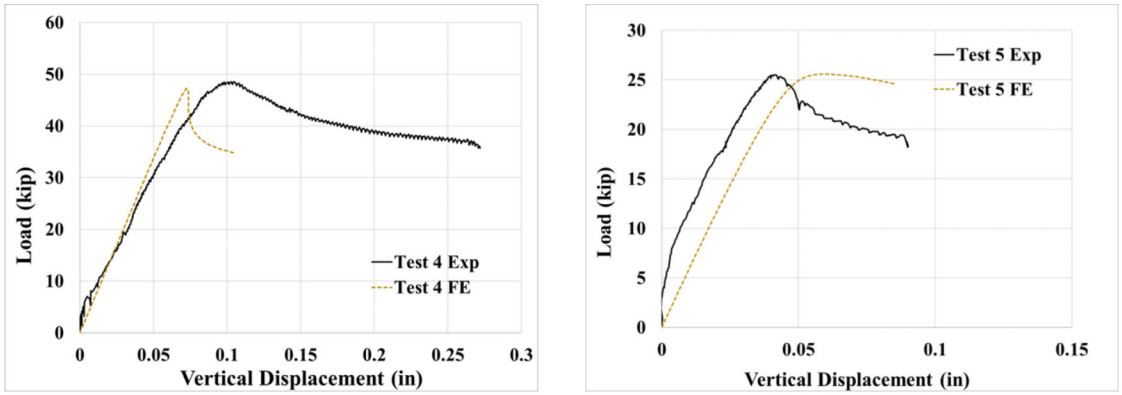

(a) Specimen 4 (b) Specimen 5

Figure 6.7 Comparison of the load-displacement relationships for Specimens 4 and 5.

(a) Specimen 7 experiment (b) Specimen 7 finite element model

Figure 6.8 Comparison of the deformed shape of Specimen 7.

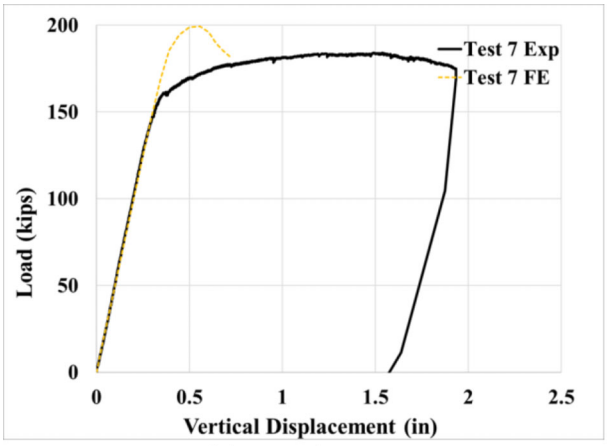

(c) Specimen 7

Figure 6.9 Comparison of the load-displacement relationship for Specimen 7.

TABLE 6.3
Comparison of capacities for Specimen 7

Specimen	Experiment	Finite Element Model	Variation
Specimen 7	184 kips	199 kips	8%

The model did not predict the reduction in stiffness observed in the experiment after 160 kips, but the model accurately predicted the initiation of yielding in the bottom flange followed by yielding around the loading region. Eventually, the entire web underwent yielding followed by OOP displacement at the web's top portion just below the loading region, similar to the observations from the performed experiment. The difference in post-peak behavior could be also observed from Figure 6.9.

7. PARAMETRIC ANALYSIS

This section describes the parametric analysis performed to investigate the effect of section loss on the corroded girders' residual shear and bearing capacity. Section loss in the girder web caused by corrosion was introduced to the numerical model by defining the remaining thickness and dimensions of the damaged region. Based on the type of the girders, the parametric analysis performed can be categorized into Parametric Study 1 and Parametric Study 2. Parametric Study 1 investigated the effect of section loss on the bearing capacity of an unstiffened girder. In contrast, Parametric Study 2 investigates the effect of section loss on stiffened girders' shear and bearing capacity. Benchmarked numerical modeling approach using finite element modeling software, ABAQUS, discussed in Section 6, was used for the parametric analysis. The study involved modeling different corrosion scenarios and predicting the corresponding residual capacity. The corrosion scenario is modeled through input parameters such as the corroded region's length, the corroded region's height, and the remaining thickness in the corroded region. The range of each parameter and the increments were presented in Section 7.2. Results from the parametric analyses were investigated to identify the relationship between the topology of the corroded region and the residual capacity and failure mode of the girders.

7.1 Corrosion Pattern

Naturally, corroded girders were obtained from the decommissioned bridges for experimental purposes. From analyzing the section loss measurements in the corroded girders, the observed corrosion pattern can be approximated to be trapezoidal in shape discussed in Section 3.2. Details of the corrosion pattern incorporated in the parametric analysis are shown below in Figure 7.1 and Figure 7.2. This typical corrosion pattern consists of four parameters, (1) length of the corroded region (CL), (2) effective thickness loss in the web (t_{loss}), (3) height of the corroded region at the girder end (CH1) and (iv) the height of the corroded region on the opposite side of the girder end (CH2).

Previous researchers have considered rectangular and triangular corrosion patterns in the web. The uniqueness of this trapezoidal corrosion pattern lies in the implicit consideration of the triangular and rectangular corrosion patterns. For example, it becomes a rectangular pattern when the height of corroded regions on both sides is equal (CH1 = CH2). On the other hand, when the height of corrosion on the opposite side of the girder end is zero (CH2 = 0), the shape of the corroded region is triangular. Due to this uniqueness, parametric analysis utilizing this corrosion pattern is rich and more comprehensive.

7.2 Corrosion Topology Parameters

Each parameter was varied over a specific range. For example, thickness loss in the web varied from 0.1 t_w to 0.9 t_w, where t_w was the nominal thickness of the web. Thickness lost was assumed to be uniform over the entire corroded region. The effect of holes in the web, formed due to complete section loss in the web, has not been considered in either of the two parametric analyses performed. The height of the corroded region at the girder end was varied from 0.2 h to 0.6 h, where h is the clear distance between the flanges less the inside corner radius on each side. The height of the corroded region on the opposite side to the girder end (CH2) was varied from 0 to 0.6 h or CH1, whichever is minimum. This is to conform to the realistic situation where corrosion is caused by the deicing salts and water leaking through the expansion joint at the girder end, which results in the larger height of the corroded region at the girder end (CH1 > CH2). As a result, the value of CH2

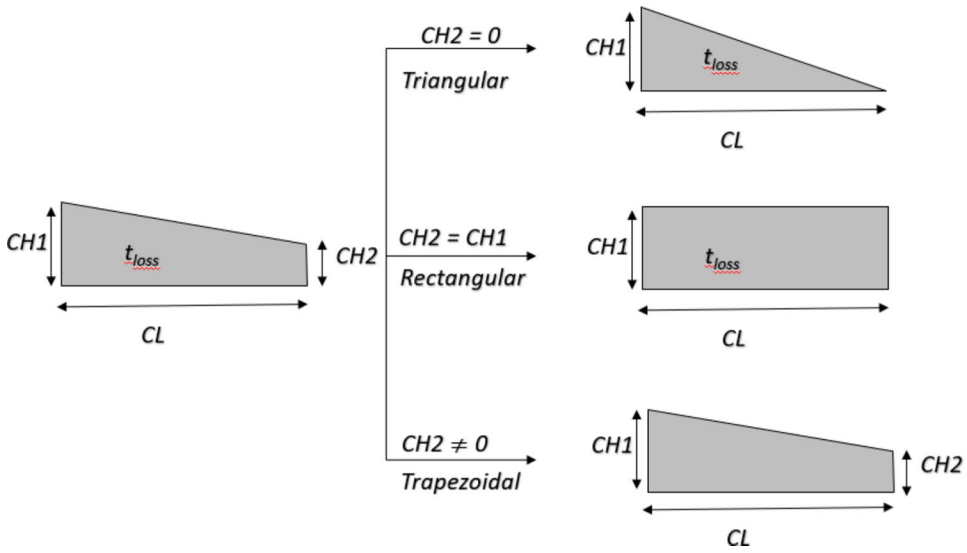

Figure 7.1 Corrosion pattern.

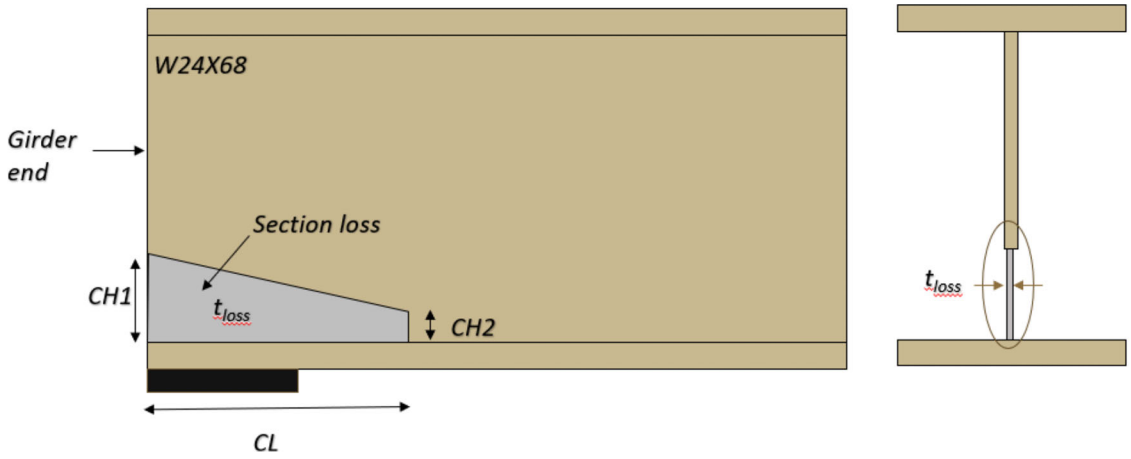

Figure 7.2 Schematic of girder with trapezoidal corrosion pattern.

TABLE 7.1
Corrosion topology parameters

Parameters	Range Start	Range End	Difference	Increment
Corrosion Height CH1 (γh)	0.2 h	0.6 h	0.4 h	0.1 h
Corrosion Height CH2 (κh)	0 h	0.6 h	0.6 h	0.1 h
Thickness Loss t_{rem} (αt_w)	0.1 t_w	0.9 t_w	0.8 t_w	0.1 t_w
Corrosion Length CL (βh)	0.1 h	2.5 h	2.4 h	0.1 h

cannot take a value greater than CH1. The length of the corroded region varied from 0.1 h to 2.5 h. Values of CH1, CH2, and CL were increased in increments of 0.1 h while thickness lost in the web t_{loss} was increased in increments of 0.1 t_w. The range of each parameter is summarized below in Table 7.1. The number of combinations from these parameters was about 4,900 for each parametric study.

7.3 Numerical Model Using Python Script

The finite element model was developed using the commercially available software ABAQUS. The full-length girder was modeled in all the parametric analyses, and the girder was a W24 × 68 rolled steel section. Models were generated utilizing the same girder size but with varying corrosion parameters in each model. Generating an extensive number of models manually was not feasible and required automation. Therefore, a Python script was developed for generating the numerical models. Python script utilizes the exact numerical modeling approach benchmarked to the experimental data discussed in Section 6.

Input to the Python script consists of the identification number for each corrosion scenario and input values for each of the four corrosion parameters as shown in Table 7.2 and Table 7.3. Section loss was introduced into the web, based on the input details of corrosion parameters, and partitioned automatically at the edges of the section loss region. Fine mesh with an element size of 0.5 in. × 0.5 in. was utilized at full depth of the web up to 8 ft. Coarse mesh with an element size of 1 in. × 1 in. was used for the remaining 14 ft. This detailed partitioning and meshing strategy tailored based on the corrosion topology of each model was automated with the script.

7.4 Parametric Study 1

Parametric Study 1 consisted of models utilizing W 24 × 68 section without any stiffeners and with section loss and subjected to shear loading at 40 in. from the girder end. These models were identical to Specimen 5. Therefore, the numerical modeling approach benchmarked with Specimen 5 experiment's results was used in Parametric Study 1. Analysis of each model consists of an eigenvalue buckling analysis and a quasi-static analysis. First, eigenvalue buckling analysis was performed, and the first eigenmode (usually web local crippling in the section loss region) was scaled by a factor of 0.5 t_w and introduced as the initial imperfection for the quasi-static analysis. The expected failure mode was either web buckling or web local crippling in the section loss region observed in Experiment 5. The objective of Parametric Study 1 was to study the effect of section loss on the bearing capacity of unstiffened girders and investigate the relationship between corrosion topology parameters and the loss in bearing capacity.

7.4.1 Effect of Thickness Loss

Parameters were varied as shown below with varying thickness loss (t_{loss}) (from 0.1 tw to 0.9 tw) with

TABLE 7.2
Input for Python script

Scenario	CH1	CH2	CL	t_{loss}
4870	4.31	0.00	2.16	0.04
4871	6.47	2.16	4.31	0.08
4872	8.62	4.31	6.47	0.12
4873	10.78	6.47	8.62	0.17
4874	12.93	8.62	10.78	0.21
4875	6.47	10.78	12.93	0.25
4876	8.62	12.93	15.09	0.29
4877	10.78	10.78	17.24	0.33
4878	12.93	10.78	19.40	0.37

TABLE 7.3
Parametric study 1: variation of thickness loss

CH1	CH2	CL	tl_{oss}
0.6 h	0.6 h	0.5 h	0.9 t_w
0.6 h	0.6 h	0.5 h	0.8 t_w
0.6 h	0.6 h	0.5 h	0.7 t_w
0.6 h	0.6 h	0.5 h	0.6 t_w
0.6 h	0.6 h	0.5 h	0.5 t_w
0.6 h	0.6 h	0.5 h	0.4 t_w
0.6 h	0.6 h	0.5 h	0.3 t_w
0.6 h	0.6 h	0.5 h	0.2 t_w
0.6 h	0.6 h	0.5 h	0.1 t_w

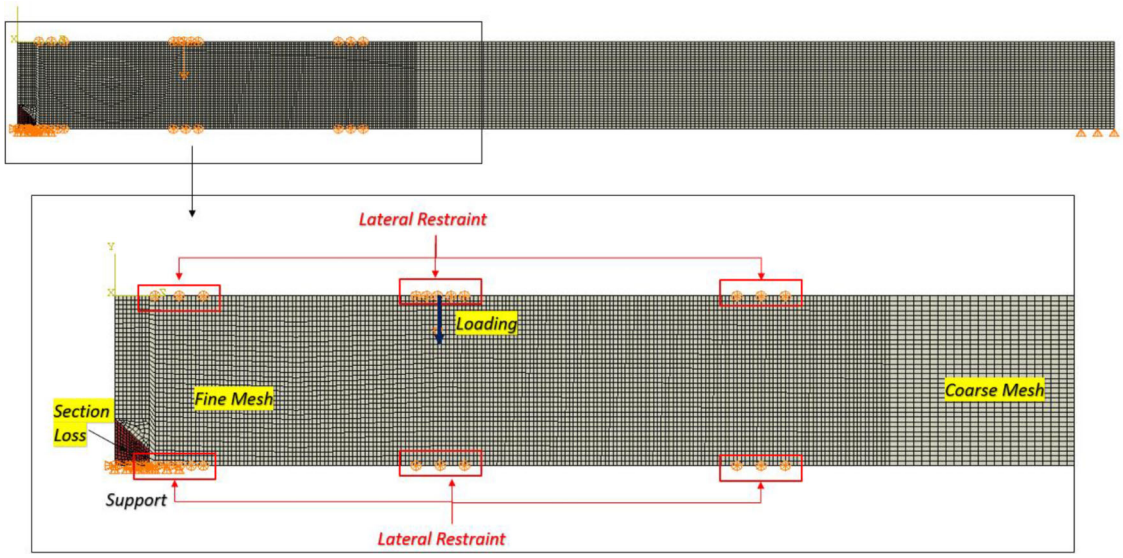

Figure 7.3 Parametric study 1: numerical model.

constant corrosion heights (CH1, CH2) and corrosion length (CL). After performing the set of analyses (for example, shown), the corrosion length (CL) was increased by 0.1 h. Then, keeping the corrosion heights (CH1, CH2) and the new corrosion length (CL) as constant, the thickness loss was varied (from 0.1 tw to 0.9 tw), and simulations were performed. This process was repeated so that simulations included corrosion scenarios with different corrosion lengths and heights.

From the comprehensive simulations performed in Parametric Study 1, only a few results have been selected and shown in this section. Figure 7.4 shows the results for the girder with section loss modeled with corrosion height (CH1) as 0.2 h, corrosion height (CH2) as 0.1 h, and corrosion length (CL) as 0.6 h. In Figure 7.4, Model A, B, and C have thickness loss of 40%, 60%, and 90%, respectively. Three key observations could be made from the results regarding the failure modes, residual capacity, and minimum thickness loss. The first observation is regarding the failure modes, either web buckling or web local crippling. Web buckling failure mode is expected for girders with low section loss. As section loss increases, maximum OOP displacement in the web gradually shifts downward towards the bottom region with section loss causing web local crippling failure mode. In other words, web local crippling failure mode is expected for unstiffened girders with severe section loss. The second observation was regarding the capacity variation with the increase in section loss. Small reduction in bearing capacity is observed for the girder with less than 40% thickness loss. However, a significant drop in the bearing capacity was observed after 40% thickness loss. The third observation was that the same conclusion could not be drawn for all the corrosion scenarios. For example, from the six results shown in Figure 7.5, different reduction trends of the bearing capacity could be observed for different corrosion scenarios. However, it can safely be concluded that a girder with a section loss of less than 20% will not have a significant reduction in its bearing capacity and can be considered as limiting thickness loss.

7.4.2 Effect of Corrosion Length CL

Parametric Study 1 were performed as described in Section 7.4.1, and analysis results were obtained for varying corrosion length (CL) from 0.1 h to 2.5 h for

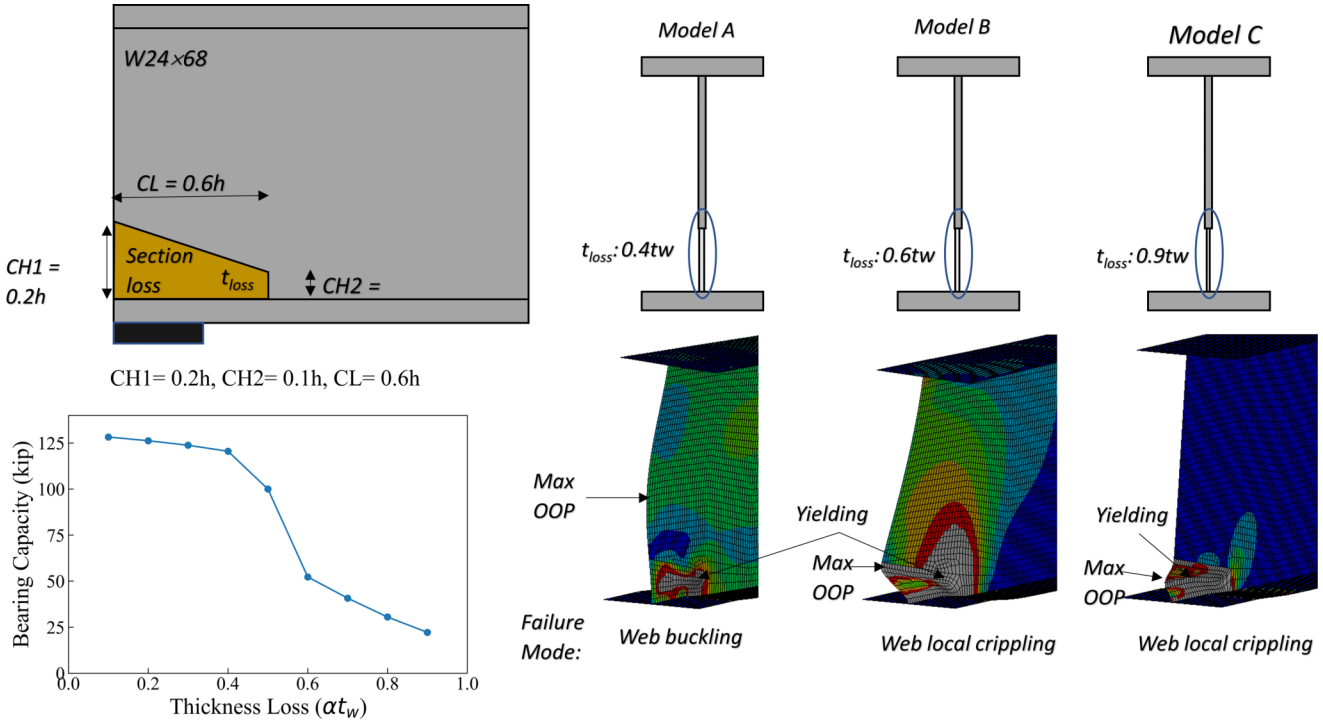

Figure 7.4 Effect of thickness loss on bearing capacity and failure modes.

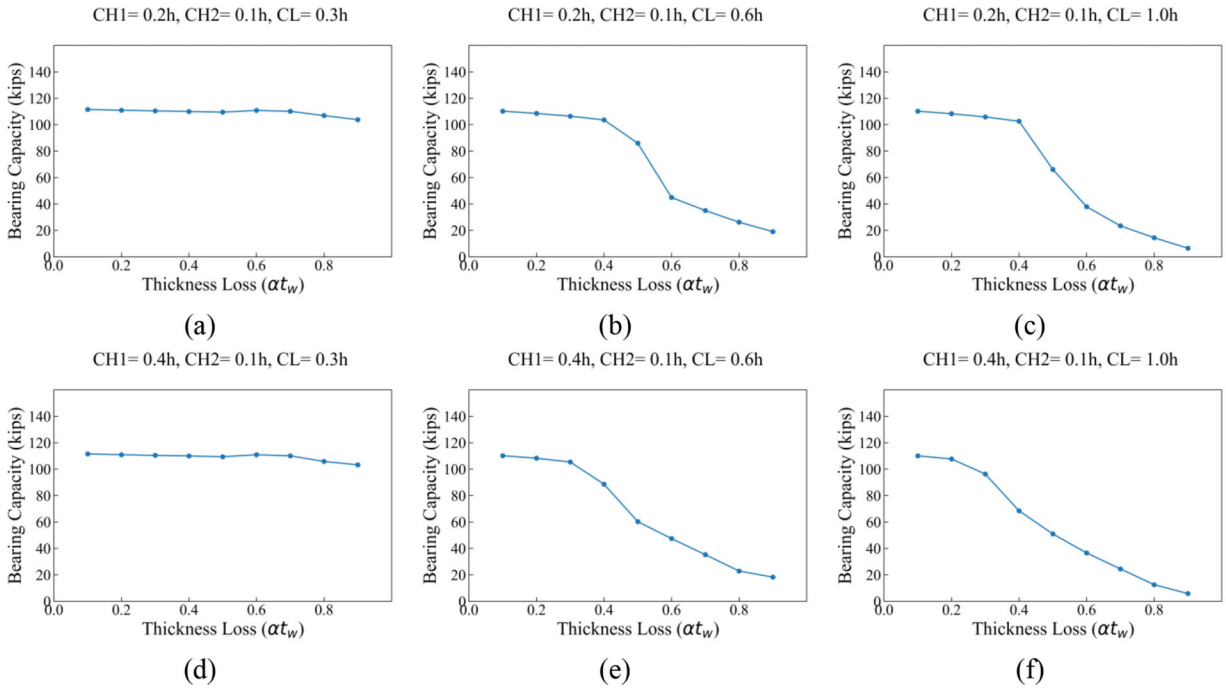

Figure 7.5 Effect of thickness loss on bearing capacity.

every corrosion height (CH1, CH2) and thickness loss (t_{loss}). From the comprehensive simulations performed in Parametric Study 1, only a few results have been selected and shown in this section. Predicted capacities from the simulation for the corrosion scenario with thickness loss of 70%, corrosion height CH1 of 0.2 h, and corrosion height of CH2 of 0.1 h are shown below (b). Model A, Model B, and Model C has a corrosion length of 0.5 h, 1.0 h, and 1.8 h, respectively. Figure 7.6(a), and corresponding finite element simulation results are presented in Figure 7.6(c).

From Figure 7.6(b), a reduction in the bearing capacity was observed with the increase in corrosion length. However, the reduction plateaued after a

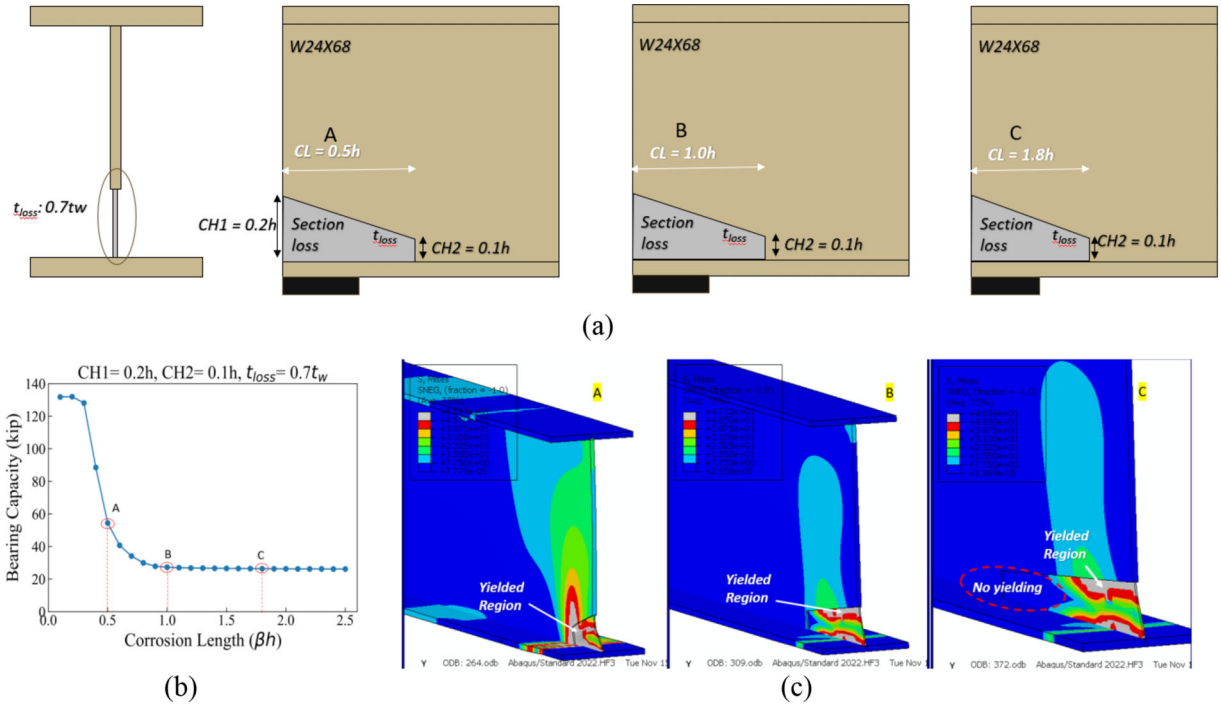

Figure 7.6 Effect of corrosion length (CL) on bearing capacity and failure modes.

specific corrosion length. In other words, after a certain length of corrosion region (CL), there was no significant reduction in bearing capacity with an increase in the corrosion length. This behavior was explained by comparing the finite element results at the peak capacity of Model A, B, and C in Figure 7.6(c). In Model A, the length of the corroded region was 0.5 h (10.8 in.), and at the peak load, almost the entire section loss region underwent yielding. In Model B, the length of the corroded region was 1 h (21.6 in.). At the peak load, almost the entire section loss region had stress concentration and underwent yielding at the boundaries of the section loss. However, in Model C, with a corrosion length of 1.8 h (38.8 in.), only a portion of the section loss region has stress concentrations, and the remaining region was unaffected. Although the failure mode in all models, Model A, B, and C is web local crippling, no capacity reduction was observed between Model B and C despite the larger section loss region in Model C.

In addition to above, Figure 7.7 shows the results for six different corrosion scenarios and variation in reduction of bearing capacity with corrosion length for different corrosion scenarios. Figure 7.7(a) and Figure 7.7(b) shows the results for the models with the same corrosion heights but different thickness loss and corresponding different reduction trends in the bearing capacity. In Figure 7.7(a) has a maximum reduction in the capacity of about 15 kips, while Figure 7.7(b) has a maximum reduction of about 100 kips. A similar observation could be made from Figure 7.7(a) and Figure 7.7(c) where both the models have the same thickness loss but different corrosion heights (CH1). However, from all the results shown in Figure 7.7, it can be safely established that reduction in capacity plateaus after the corrosion length of 1.0 h (21.6 in.). This limiting corrosion length (27 in.) in terms of bearing length (N = 8 in., in the simulations and the experiment) would be approximately 2.7 N.

7.4.3 Effect of Corrosion Height CH1 and CH2

Parametric Study 1 was performed as described in Section 7.4.1, and analysis results were obtained for varying corrosion heights (CH1 and CH2) from 0.1 h to 0.6 h for every corrosion length (CL) and thickness loss (t_{loss}). From the comprehensive simulations performed in Parametric Study 1, only a few results have been selected and shown in this section. Predicted capacity from the simulations for the corrosion scenario with corrosion height (CH2) of 0.1 h and corrosion length (CL) of 1.0 h is shown in Figure 7.8(a). Simulation results for corrosion scenarios with corrosion height (CH2) of 0.3 h and corrosion length (CL) of 1.0 h is shown in Figure 7.8(b). Simulation results for corrosion scenarios with corrosion height (CH1) of 0.5 h and corrosion length (CL) of 1.0 h is shown in Figure 7.8(c). All three results shown include results for different thickness loss ranging from 0.1 t_w to 0.9 t_w. In general, no reduction in the bearing strength was observed for the corrosion scenarios with different corrosion height (CH1 and CH2) and same corrosion length and thickness loss. Reduction has been observed in only in Figure 7.8(a) and Figure 7.8(c) corresponding to thickness loss 0.3 t_w and 0.4 t_w. Apart from this, the general trend observed was of no strength reduction with respect to corrosion heights.

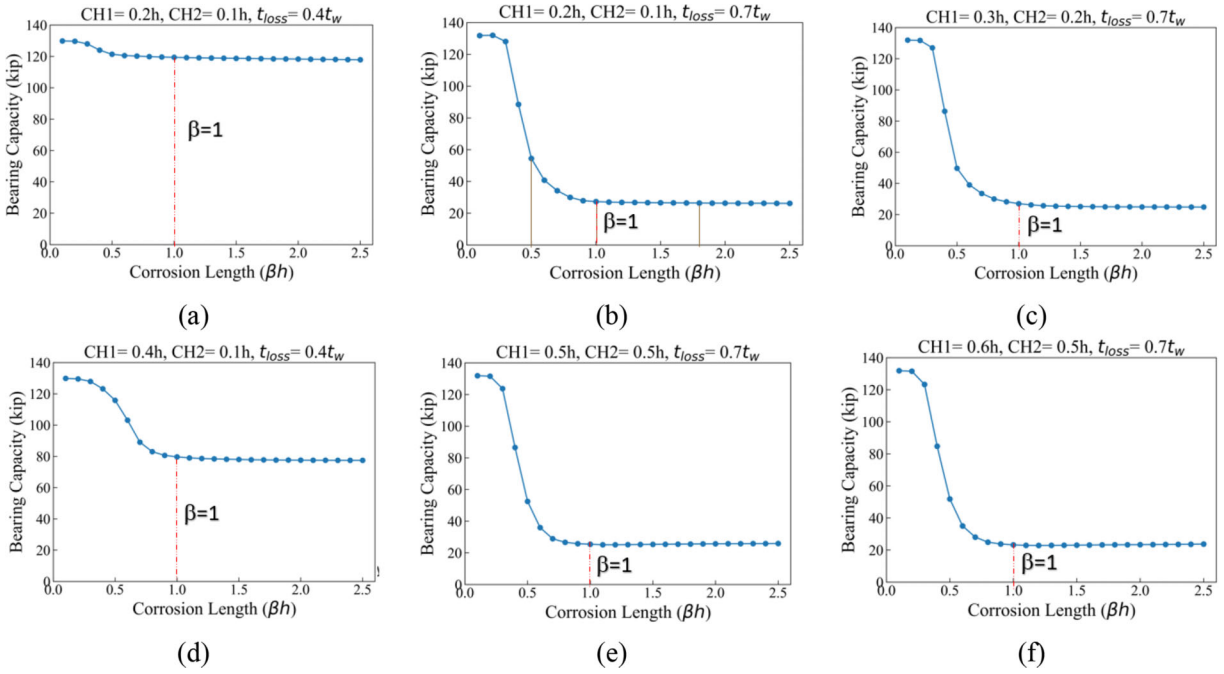

Figure 7.7 Effect of corrosion length (CL) on bearing capacity.

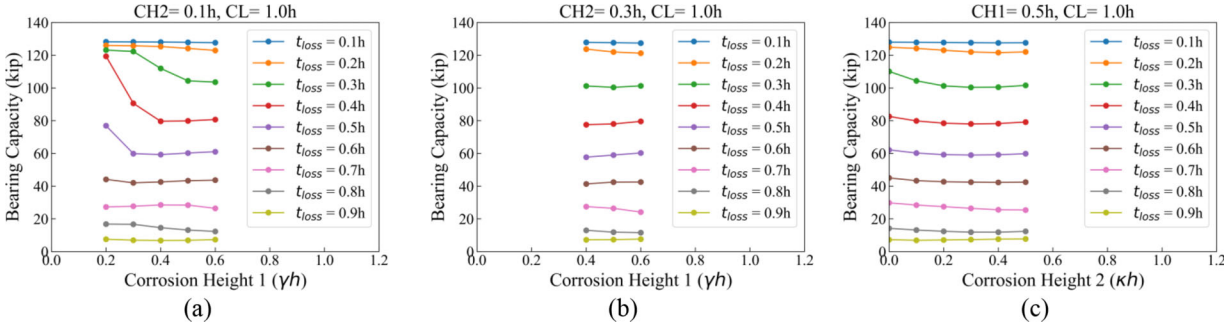

Figure 7.8 Effect of corrosion height (CH1 and CH2) on bearing capacity.

7.5 Parametric Study 2

Models in the parametric study 2 consist of a W24 × 68 section like the previous parametric study. However, the critical difference is the presence of stiffeners. The simulation modeled existing partial depth transverse stiffeners on the corroded girder's web. In addition, full-depth stiffeners were modeled at the bearing and loading regions. Finally, the girder was subjected to shear loading at 40 in. from the girder end. This model was a replica of Specimen 6, and the numerical modeling approach was benchmarked with the Experiment 6 results. Analysis of the model consists of an eigenvalue buckling analysis and a quasi-static analysis. First, eigenvalue buckling analysis was performed, and the first eigenmode was web local crippling in the section loss region. Secondly, the first eigenmode was scaled by a factor of 0.5 tw and introduced as the initial imperfection for the quasi-static analysis.

The expected failure mode was web shear buckling observed in Experiment 6. The objective of this Parametric Study 2 was to study the effect of section loss on the shear capacity of stiffened girders and investigate the relationship between corrosion topology parameters and the loss in shear capacity. The presence of stiffeners in the model does not increase its shear capacity since the section was a rolled steel section and was compact enough to reach its plastic shear capacity. However, in normal loading conditions, web local crippling failure governs over shear failure. Therefore, the influence of failure modes other than shear yielding or shear web buckling must be avoided or reduced to investigate the effect of section loss on the shear capacity alone. Full-depth stiffeners were provided to increase the bearing strength and allow the web to fail in shear.

7.5.1 Effect of Thickness Loss

Parametric Study 2 performed included corrosion scenarios with varying thickness loss (t_{loss}) (ranging from 0.1 tw to 0.9 tw) for different corrosion lengths

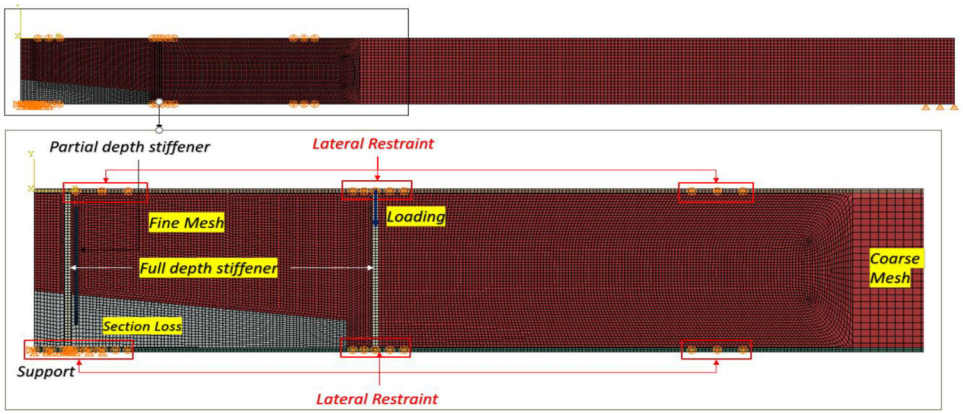

Figure 7.9 Parametric study 2: numerical model.

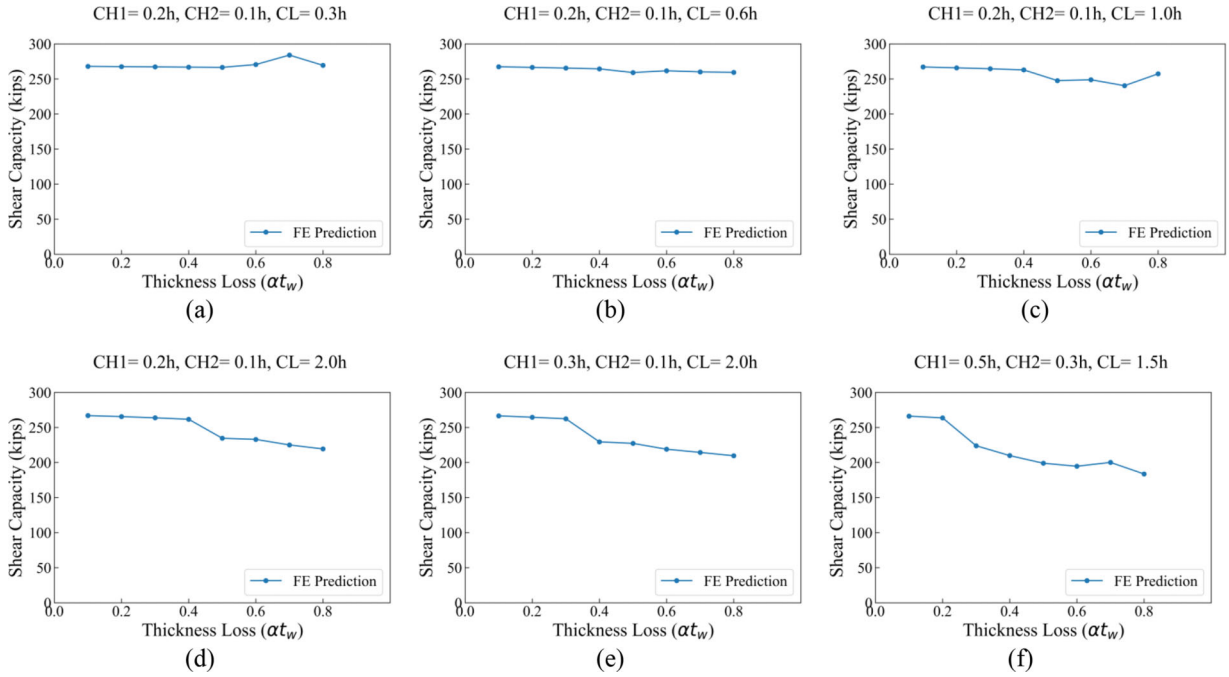

Figure 7.10 Effect of thickness loss on shear capacity.

(ranging from 0.1 h to 2.5 h) and corrosion heights (CH1 and CH2 ranging from 0.1 h to 0.6 h). From the comprehensive simulations performed in Parametric Study 2, only a few results have been selected and shown below. In Figure 7.10(a–d) comparison is made for corrosion scenarios with corrosion heights CH1 = 0.2 h, CH2 = 0.1 h but different corrosion lengths. Figure 7.10(a–d) have a corrosion length of 0.3 h, 0.6 h, 1.0 h, and 2.0 h, respectively, and each figure has predicted shear capacity corresponding to different thickness losses. Maximum reduction in capacity in Figure 7.10(a–d) was 4 kips, 9 kips, 11 kips and 73 kips, respectively. Maximum reduction observed in Figure 7.10(e–f) is 82 kips and 110 kips. In general, no significant reduction was observed for corrosion scenarios with thickness loss less than 0.2 tw (20%). However, for the corrosion scenarios with thickness loss greater than 0.2 tw (20%), reduction trend in residual shear capacity can be observed with the increase in the thickness loss. Moreover, this reduction trend grows more significant with the increasing length of the corroded region.

7.5.2 Effect of Corrosion Length CL

Figure 7.11(a, b) consists of the results for the corrosion scenarios with corrosion height CH1 as 0.2 h, CH2 as 0.1 h but thickness loss of 0.2 t_w (20%) and 0.6 t_w (60%), respectively. Increase in the length corroded region resulted in the reduction of the residual capacity. Maximum reduction observed in Figure 7.11(a) is 3 kips but in Figure 7.11(b) is 41 kips. Reason for very low reduction observed in Figure 7.11(a) for different corrosion length is the low thickness loss (0.2 t_w). Similar observation could be made from Figure 7.11(d) for the corrosion scenario with corrosion height CH1 as 0.4 h, CH2 as 0.2 h. However, the most important

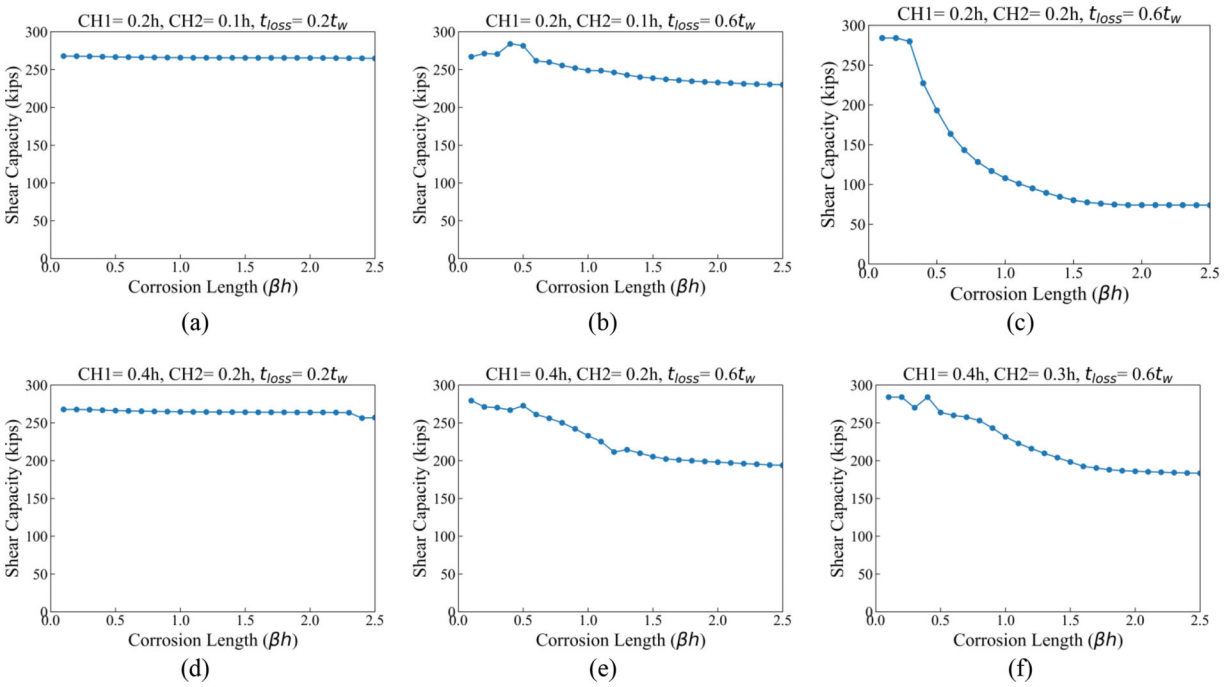

Figure 7.11 Effect of corrosion length (CL) on shear capacity.

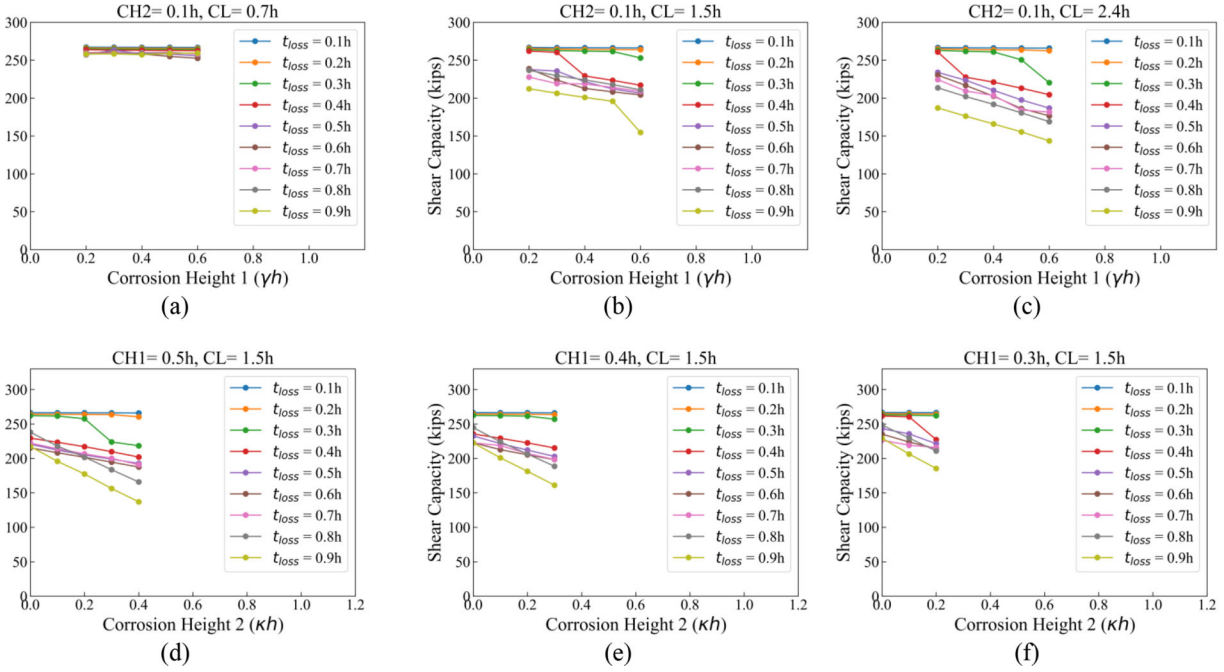

Figure 7.12 Effect of corrosion height (CH1 and CH2) on shear capacity.

observation is the large reduction in the shear capacity with increase in the length of corrosion and the thickness loss Figure 7.11(c, e, f).

7.5.3 Effect of Corrosion Height CH1 And CH2

In Figure 7.12(a–c) results are shown for the corrosion scenarios with corrosion height CH2 as 0.1 h but corrosion length of 0.7 h, 1.5 h, and 2.4 h, respectively. Each figure has results corresponding to different thickness loss and different corrosion height CH1. In general, with the increase in the height of corrosion CH1, reduction in the shear capacity is observed. This reduction is becoming more significant when thickness loss is greater than 0.2 t_w, consistent with the observations made earlier in Sections 7.5.1 and 7.5.2. Linear reduction in the capacity is observed with the increase in the corrosion height CH1.

In contrast to the above, Figure 7.12(d–f) shows the effect of corrosion height CH2 on the residual shear capacity. Figure 7.12(d–f) include the corrosion scenarios with corrosion length of 1.5 h but different corrosion height CH1 as 0.5 h, 0.4 h, and 0.3 h, respectively. Each figure has results corresponding to different thickness loss and different corrosion height CH2. Similar observations could be made for the effect of corrosion height CH2 on residual shear capacity. Linear reduction in shear capacity is observed with the increase in the corrosion height CH2 for most of the scenarios. No significant reduction is observed for the corrosion scenarios with thickness loss less than 0.2_s (20%).

8. MODIFICATION FACTOR

Primary objective of the study was to develop a reduction factor that estimates the corroded steel girders' residual bearing capacity and shear capacity. For this purpose, large-scale experiments were performed, and numerical models were developed. An extensive parametric study was carried out for different corrosion scenarios. Results from the Parametric Study 1 and 2, discussed in Section 7 were analyzed using symbolic regression to develop reduction factors. Symbolic regression analysis is a type of regression analysis that generates a mathematical expression that is best fitting to the dataset provided. This study adopted symbolic regression analysis utilizing genetic programming technique to develop the reduction factors. The data set provided is the different corrosion scenarios and corresponding predicted capacities from the parametric analysis.

Symbolic regression analysis was performed by first shuffling the data randomly and split into groups, Group A and Group B. Group A consists of 75% of the total data set while Group B consists of the remaining 25% of the data. The second step also called "training step" was to use the Group A data to develop a mathematical expression that estimates the capacity considering the corrosion parameters provided. Genetic programming technique was used during this process. Then, the estimated capacity was compared against the predicted capacity from the finite element simulations. After every comparison, the mathematical expression is evolved and evaluated again. This repetitive process was carried out until the desired fitness level was reached. The third and final step in the process was to use Group B data which was never used in the training step and test the accuracy of the resulting mathematical expression.

The equations for the reduction factor generated from the regression analysis are shown below. Section 8.1 consists of the equations for the calculation of the reduction factor for web local crippling while Section 8.2 consists of equation for the reduction factor for shear capacity reduction.

8.1 Residual Web Local Crippling Capacity of Corroded Steel Girder

8.1.1 Reduction Factor for Web Local Crippling Capacity

From the Parametric Study 1, reduction in the web local crippling has a strong relationship with the length of the corroded region (CL) and thickness loss in the web (t_{loss}). Therefore, the two proposed equations consist of only factors associated with the corrosion length and thickness loss in the web. First proposed equation, Equation 8.1 is applicable for the corrosion scenario when the length of the corroded region (CL) is less than value of h, where h is the clear distance between the flanges less the inside corner radius on each side for rolled steel section and clear distance between the inner surface of the flanges for the plate girders. At larger corrosion lengths (CL > 1.0 h), no significant reduction is observed in the web local crippling capacity. For this purpose, a slightly different equation, Equation 8.2 was proposed for the corrosion scenario when the length of the corroded region (CL) is greater than the value of h.

When CL < h

$$\phi_{r\_wlc} = 0.8 - \left(1.4e^{\left(\frac{-1}{3\beta}\right)}(\alpha)\right) \qquad \text{(Eq. 8.1)}$$

When CL ≥ h

$$\phi_{r\_wlc} = 0.8 - \left(1.4e^{\left(\frac{-1}{3}\right)}(\alpha)\right) \qquad \text{(Eq. 8.2)}$$

Where,

CL = length of corroded region.

β = corrosion length factor $= \dfrac{CL}{h}$

α = thickness reduction factor $= \dfrac{t_{loss}}{t_{web\_nominal}}$

h = the clear distance between the flanges less the inside corner radius on each side for rolled steel section and clear distance between the inner surface of the flanges for the plate girders.

t_{loss} = average thickness loss of the web calculated averaging the thickness loss in the region above the bearing length up to a height of 3 in. above the k region.

8.1.2 Residual Web Local Crippling

Equation 8.3 shows how the residual web local crippling capacity of the corroded girder is calculated. As shown the capacity is calculated by applying the reduction factor to the nominal web local crippling capacity (uncorroded section) calculated as per provisions in *AASHTO LRFD Bridge Design Specifications* (2020).

$$R_{r\_wlc} = R_n * \phi_{r\_wlc} \qquad \text{(Eq. 8.3)}$$

Where,
R_n = nominal web local crippling capacity.
R_{r_wlc} = residual web local crippling capacity.
ϕ_{r_wlc} = reduction factor for web local crippling capacity.

8.2 Residual Shear Capacity of Corroded Steel Girder

8.2.1 Reduction Factor for the Shear Capacity

From the Parametric Study 2, it was found that the parameters corrosion length (CL), thickness loss (t_{loss}), corrosion heights (CH1, CH2) have a strong influence on the reduction of the shear capacity. Therefore, the proposed equation (Equation 8.4) for the reduction factor for the shear capacity consists of all the four parameters.

$$\phi_{r\_shear} = 1 - 0.4(\beta) * (0.7\gamma + 0.5\kappa) * \alpha \qquad \text{(Eq. 8.4)}$$

Where,
β = corrosion length factor = $\dfrac{length\ of\ corroded\ region\ (CL)}{h}$
α = thickness reduction factor = $\dfrac{t_{loss}}{t_{web\_nominal}}$
γ = corrosion height at the girder end factor = $\dfrac{corrosion\ height\ (CH1)}{h}$
κ = corrosion height at opposite side of the corroded region = $\dfrac{corrosion\ height\ (CH2)}{h}$
h = the clear distance between the flanges less the inside corner radius on each side for rolled steel section and clear distance between the inner surface of the flanges for the plate girders.
t_{loss} = Average thickness loss of the web calculated averaging the thickness loss in the region above the bearing length up to a height of 3 in. above the k region.

8.2.2 Residual Shear Capacity

Equation 8.5 shows how the residual shear capacity of the corroded girder is calculated. As shown, the capacity is calculated by applying the reduction factor to the nominal shear capacity (uncorroded section) calculated as per provisions in AASHTO *LRFD Bridge Design Specifications* (2020).

$$V_r = V_n * \phi_{r\_shear} \qquad \text{(Eq. 8.5)}$$

Where,
V_n = nominal shear capacity.
V_r = residual shear capacity.
ϕ_{r_shear} = reduction factor for shear capacity.

8.3 Comparison to Parametric Study Results

Parametric studies conducted consisted of approximately 9,800 simulations and from the results of these studies reduction factors were developed to estimate the residual shear and bearing capacity of corroded girders. This process was discussed in Section 8.1 and 8.2. However, before this study is implemented for evaluating corroded girders in service, it is critical to understand the accuracy of the estimated capacities and limitations associated. Accuracy of each the reduction factors is demonstrated statistically through coefficient of determination (R^2). Other statistical measures such as mean square error (MSE) and its square root variant which is also known as root mean square deviation (RMSD) are other alternative measures that can be used. However, coefficient of determination (R^2) is selected here because the value of R^2 ranges between 0 and 1 where as MSE and RMSD ranges between 0 and infinity. Interpretation of the results of coefficient of determination (R^2) is intuitive, higher the value of R^2 (closer to 1), the better the reduction factor fits the predicted capacities from the numerical analysis.

Table 8.1 shows the coefficient of correlation (r) and coefficient of determination (R^2) for the reduction factors shown in Equation 8.1 and Equation 8.2, which provides the reduction factor for the web local crippling capacity of corroded girder and has coefficient of correlation (r) value of 0.976 and coefficient of determination (R^2) value of 0.95. High value of R^2 indicates a good relationship between the reduction factor and predicted capacities from the numerical analysis. In addition, Figure 8.1 shows the comparison between the residual bearing capacity estimated from the reduction factor proposed (Equation 8.1 and Equation 8.2) and numerically predicted capacities. Estimated capacities from the reduction factors developed are overestimated in certain regions while underestimated in other regions. However overall, a good relationship and fit is observed between the two.

Table 8.1 shows the coefficient of correlation (r) and coefficient of determination (R^2) for the Equation 8.4, which provides the reduction factor for the shear capacity of corroded girder and has coefficient of correlation (r) value of 0.94 and coefficient of determination (R^2) value of 0.88. The value of R^2 for Equation 8.4 is certainly not as high as the R^2 for Equation 8.1 and Equation 8.2, however 0.88 or 88% is still a high value and indicates a good relationship between the reduction factor and predicted capacities from the numerical analysis. Figure 8.2 shows the comparison between the residual shear capacity estimated from the reduction factor proposed (Equation 8.4) and numerically predicted capacities. Estimated capacities are overestimated in most regions while underestimated in other regions. However overall, a good relationship and fit is observed between the two.

8.4 Calculation of Average Section Loss (t_{loss}) for the Residual Capacity Calculation

Section loss in corroded steel girders is unique with irregular topology and non-uniform section loss. From the section loss profile analysis in Section 3.2, shape of

TABLE 8.1
Statistical evaluation of reduction parameters

Coefficient	Equations 8.1 and 8.2	Equation 8.4
Coefficient of Correlation (r)	0.97	0.94
Coefficient of Determination (R-squared)	0.95	0.88

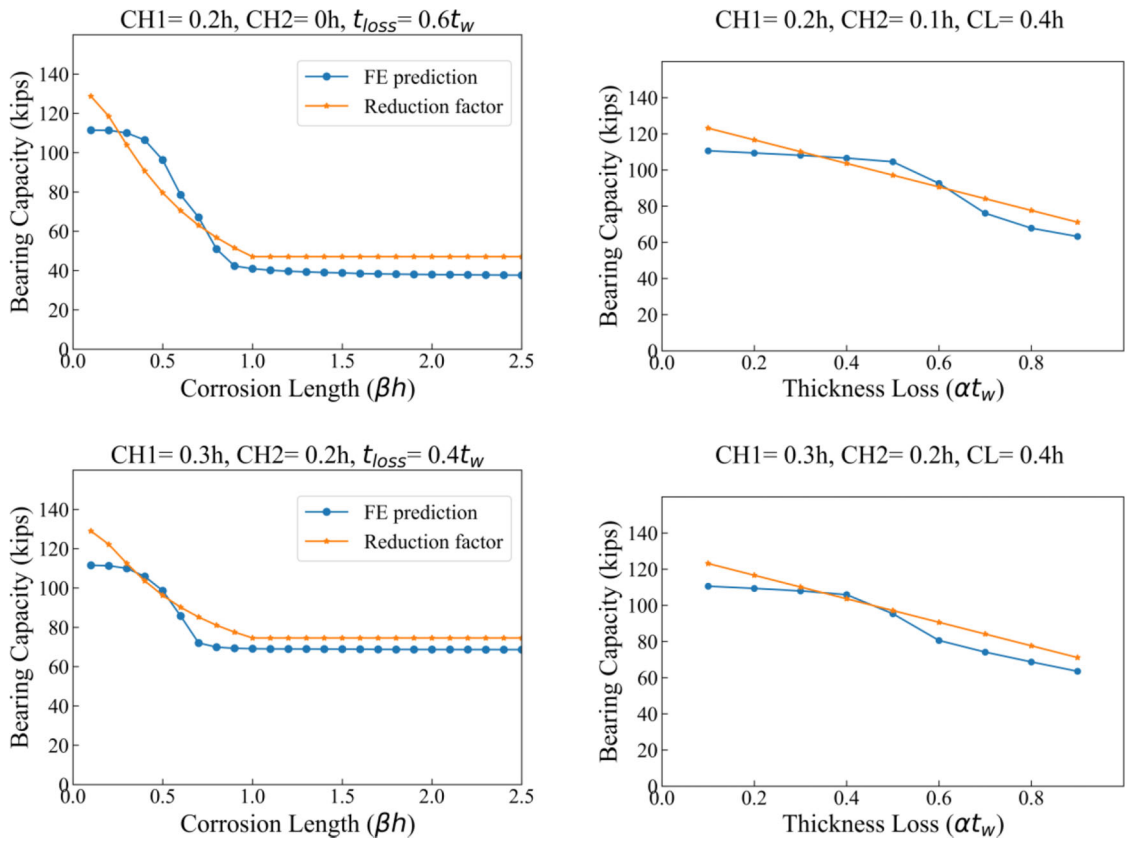

Figure 8.1 Comparison between FE predicted bearing capacity and bearing capacity calculated by proposed reduction factor.

corroded region is approximated to be trapezoidal in shape. From extensive parametric study discussed in Section 7, influence of section loss parameters on the residual shear and bearing capacity and failure mode is investigated and proposed equations (Equation 8.1 to Equation 8.5) to estimate the residual shear and bearing capacity. Parameters investigated are average thickness loss (t_{loss}), length of corroded region (CL), heights of the corroded region (CH1 and CH2). First parameter, the average thickness loss (t_{loss}) in the web calculation is slightly different and is not calculated by averaging the section loss in the entire corroded region. From the experimental and numerical analysis, it is observed that the critical location is the region just above the bearing where stress concentration and local failure is observed. Therefore, average thickness loss (t_{loss}) is calculated by averaging the section loss in the critical section which is the region above the bearing length up to a height of 2 in.–3 in. above the k region for rolled steel section or 2 in.–3 in. above the weld toe for the plate girders as shown in Figure 8.3. Remaining parameters include length of the corroded region (CL) and heights of the corroded region (CH1 and CH2) which can be measured in the field and used in the equations directly to get the residual capacity.

8.5 Application for Load Rating in AASHTOWare BrR

AASHTOWare BrR is a software used by many state transportation agencies for load rating purposes. BrR software was explored as a part of this study to incorporate the reduction factors proposed in Sections 8.1 and 8.2 for steel girders with corrosion and perform load rating. It was found that the current version of BrR (version 7.3) does not evaluate the web local crippling capacity of the steel girder, however it does evaluate the shear capacity of a steel girder as per the AASHTO *LRFD Bridge Design Specification* (2020). Moreover, BrR software allows the users to model corrosion damage in the girder and estimates the residual shear capacity considering the input damage

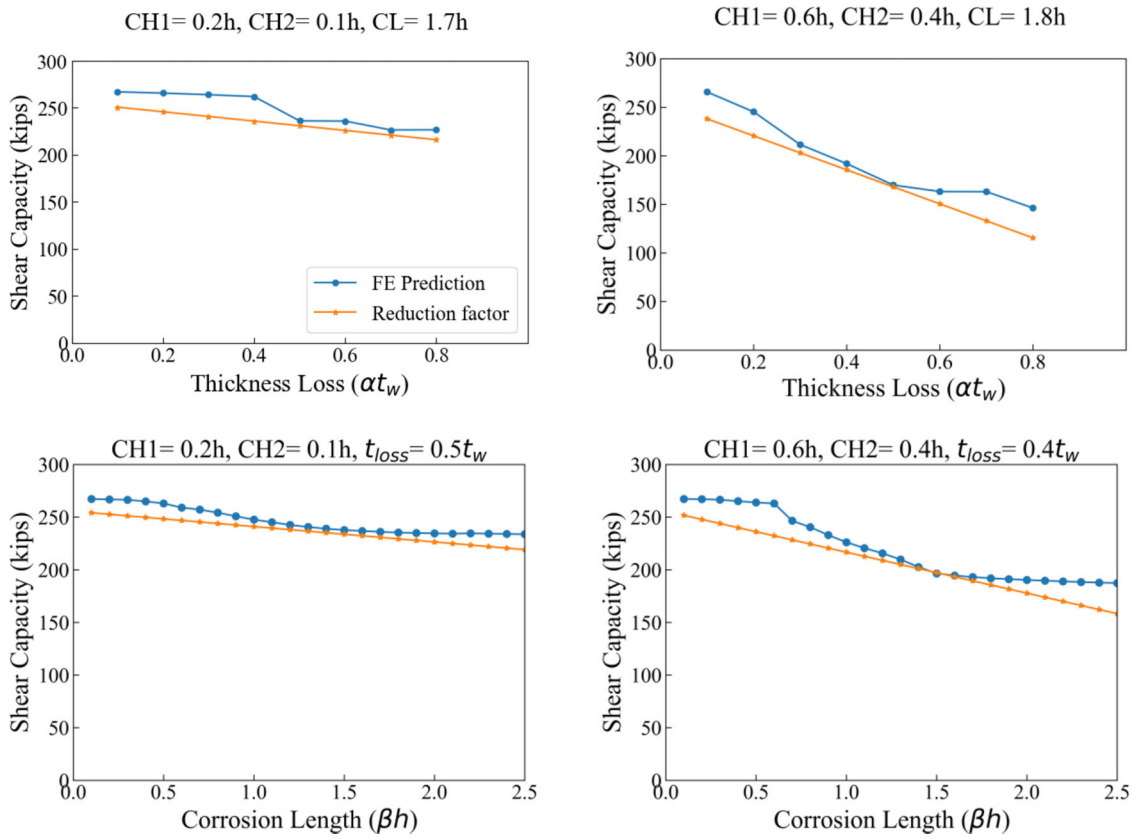

Figure 8.2 Comparison between FE predicted shear capacity and shear capacity calculated by proposed reduction factor.

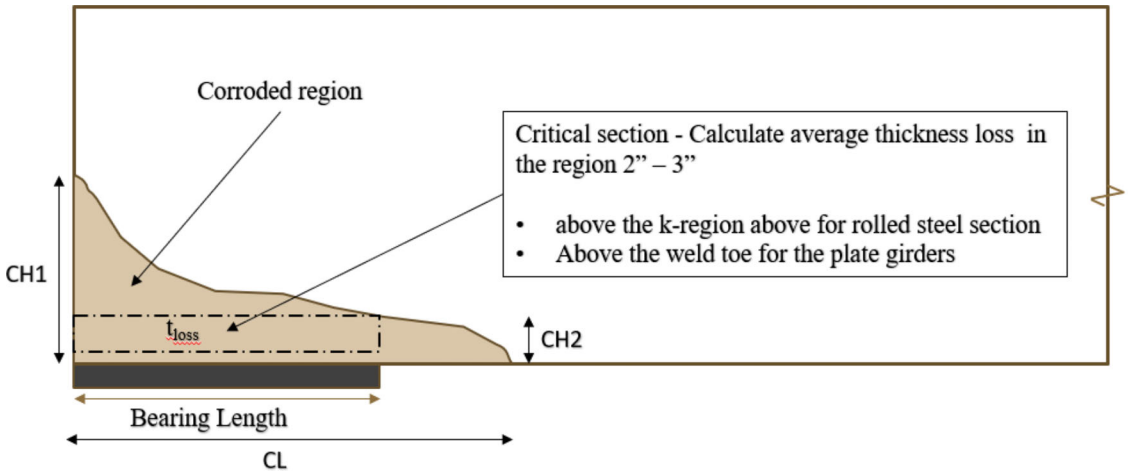

Figure 8.3 Critical section for average thickness loss calculation.

details. In BrR software, corrosion damage is modelled by defining the three inputs, (1) starting point of the corrosion from the support, (2) length of the corroded region from the starting point and (3) average thickness loss in the steel section. However, there was no provision to input the height of the corroded region and instead BrR software considers the input corrosion damage for the entire height of the web. This is the source of underprediction of the residual shear capacity estimated by BrR software. Updating the BrR software to include modeling corrosion heights, calculation of the residual shear capacity and web local crippling capacity based on the reduction factors developed in this study requires time. For immediate application, an available alternative approach is recommended to incorporate the results of this study into BrR software for load rating and this approach is decried below.

8.5.1 Load Rating Utilizing Reduction Factor

From the equations provided in Sections 8.1 and 8.2, residual shear capacity and bearing capacity can be calculated using the corresponding reduction factors. Minimum of the two values can be input at the point of interest to override the nominal capacity as shown in Figure 8.4. This is available in the "point of interest" under member alternatives in the model tree of BrR software. The point of interest will be the corroded region from the support end. Input minimum value of the calculated capacities using Equation 8.3 and Equation 8.5. This will override the nominal capacity of the section at the point of interest and load rating procedure can be performed to with these capacities to evaluate the girder.

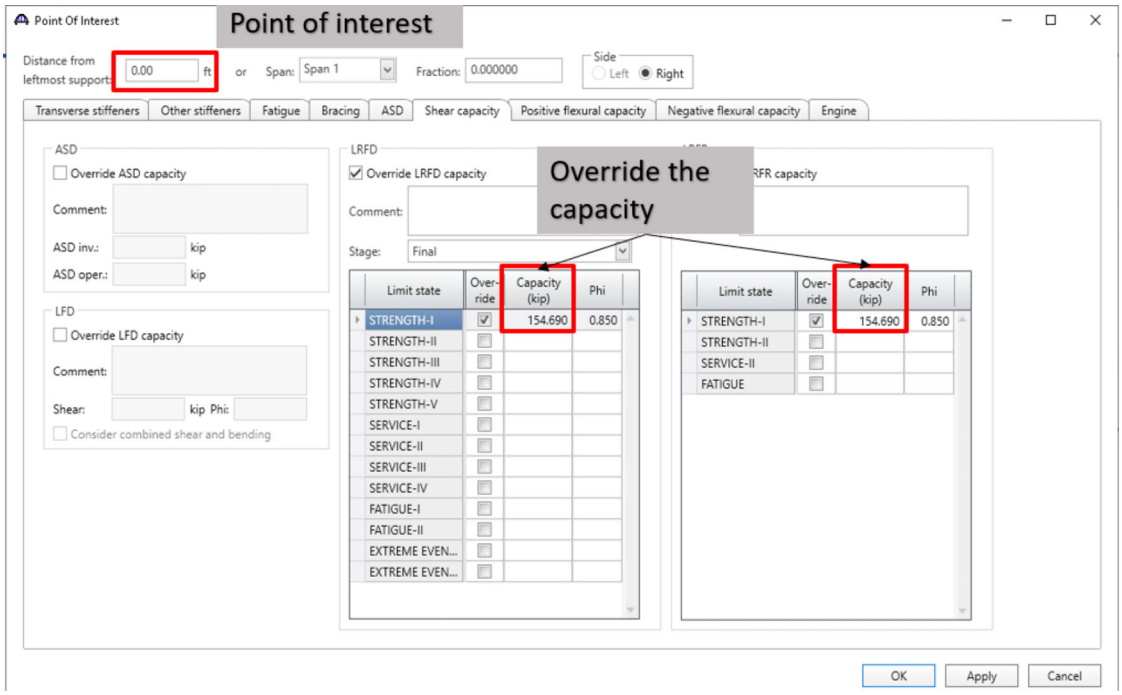

Figure 8.4 Example screenshot of overriding the nominal capacity at the point of interest in BrR software.

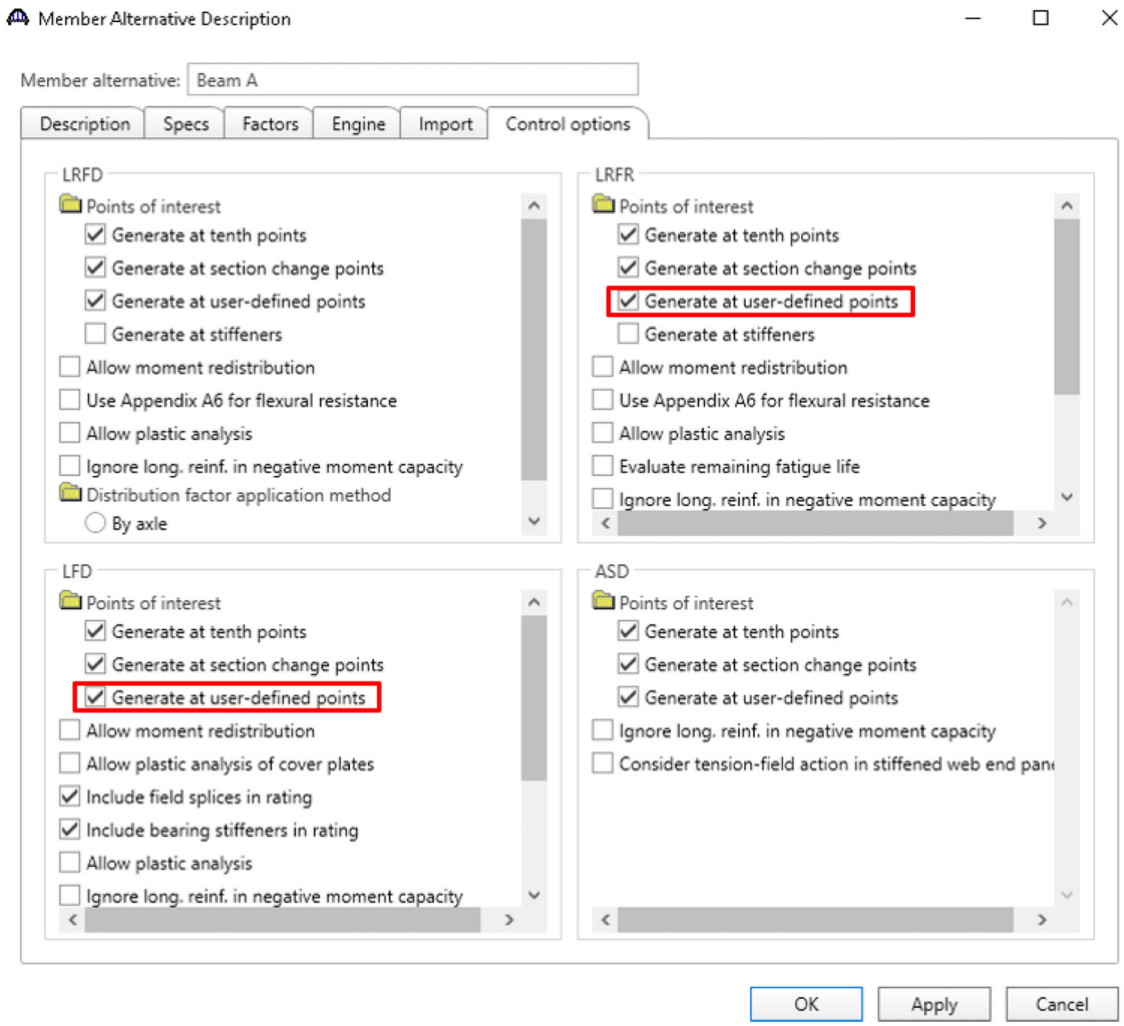

Figure 8.5 Example screen shot of "Control Options" feature available for each member.

9. CONCLUSIONS

This study investigated the effects of corrosion on the residual shear and bearing capacity of steel girders both experimentally and numerically. From the experiments conducted, governing failure modes were identified for the unstiffened and stiffened corroded sections. Numerical models were developed and benchmarked to the experiments. Influence of section loss on the residual capacity was investigated from the parametric analysis conducted consisting of more than 9,800 analyses. At the end of the study, a set of modification factors were developed that estimates the residual shear capacity of stiffened girders and the residual bearing capacity of unstiffened girders. In addition, several observations were made in each stage of the study and summarized in this section.

1. Naturally, corroded girders were obtained from decommissioned bridges in North-Split Reconstruction Project in Indiana. Girders had varying levels of corrosion, and the topology observed in the corroded region was approximately trapezoidal in shape with a larger corrosion height at the girder end. This topology was adopted in subsequent numerical models and parametric studies. This was considered realistic since corrosion at the girder end was caused by the deicing salts and water leaking through the expansion joint at the girder end, which results in a larger corrosion height at the girder end (CH1 $>$ CH2) and thus the resulting trapezoidal shape.
2. Section loss in the web was measured using an ultrasonic thickness gauge, consistent with the practice by bridge inspectors during field inspection to spot-check the residual thickness of steel girders. However, measurements were affected by the paint thickness present. Therefore, measurements were taken twice at several locations before and after paint removal. After analyzing the difference in the measurements, deducting 20 mils or 0.02 in. from the thickness measured at the locations with paint is recommended.
3. Experimental investigation showed that the governing failure mode for the unstiffened girders with section loss is web local crippling and section loss has a strong influence on the residual web local crippling capacity. From Experiment 5, it was observed that for a W24 $\times$ 68

with 70% section loss, 87% web local crippling strength reduction was observed and failure occurred at 25 kips.

4. Parametric study was performed using the benchmarked numerical models for unstiffened W24 × 68 sections with the section loss. The parametric study did not consider the presence of holes and cracks in the web. From the parametric study 1, it was found that web local crippling failure governs for girders with thickness loss in the web greater than 0.5 t_w (50%). Web buckling governs for the girder with thickness loss in the web less than 0.3 t_w (30%) as shown in Figure 7.4. In general, residual bearing capacity decreases with the increase in the thickness loss in the web. This reduction is amplified with the increase in the length of the corroded region. However, the reduction trend in the capacity plateaus after the corrosion length of 1.0 h, where h is the clear distance between the flanges less the inside corner radius on each side. The corroded region's height does not influence the residual bearing capacity of the unstiffened girders. Hence, the modification factor developed for estimating the residual bearing capacity (Equation 8.1 and Equation 8.2) considers only two of the four parameters.

    a. Average thickness loss in the web (t_{loss}).
    b. Corrosion length (CL).

5. For the stiffened girders, shear web buckling becomes the governing failure mode provided the stiffened section had bearing strengths greater than the shear strength of the section. In the experiments performed, shear web buckling failure was observed in Specimens 1, 3, and 6 while, shear rupture failure mode was observed in Specimen 2 initiated from the cracks at the bottom of the web. Therefore, it is recommended to arrest any cracks at the bottom of the web especially for the stiffened girders.
6. Parametric study 2 investigated the effect of section loss on the residual shear capacity. It was found that height of corroded region has a strong influence along with the corrosion length and thickness loss. Residual shear capacity decreases with the increase in the thickness loss in the web, amplified by the corrosion length and the corrosion heights. The modification factor developed for estimating the residual shear capacity (Equation 8.4) considers the following parameters.
    a. Average thickness loss in the web (t_{loss}).
    b. Corrosion length (CL).
    c. Corrosion height (CH1 and CH2).

7. In addition, it was observed that the existing partial depth stiffeners that were used to connect the in-service diaphragm to the girder provided additional strength against web local crippling as observed in Specimen 4. However, the extent of contribution in different corrosion scenarios is not investigated numerically.
8. Proposed equations in Equation 8.1, Equation 8.2, and Equation 8.4 consist of parameter, average thickness loss (t_{loss}). For most of the steel girders, deterioration due to corrosion typically occurs at the girder end. Critical section is the region just above the bearing and average thickness loss (t_{loss}) to be used in the equations is to be calculated averaging the thickness loss in the region above the bearing length up to a height of 3 in. above the k region for the rolled steel girders and above the weld toe for the plate girders as discussed in Section 8.4. Remaining parameters include length of the corroded region (CL) and heights of the corroded region (CH1 and CH2) which can be measured in the field and used in the equations directly to get the residual capacity.
9. AASHTOWare BrR is a software used by many state transportation agencies for load rating purposes. BrR is capable of modeling the corrosion damage and calculation of the residual shear capacity. Corrosion damage in BrR is modelled by providing length of the corroded region and corresponding thickness loss as the inputs. BrR assumes the thickness loss provided along the entire height. This assumption sometimes results in underestimating the residual shear capacity and eventually leading to lower rating factor. Another limitation of BrR is that it is not capable of calculating web local crippling capacity.
10. Proposed equations can be used to estimate the residual shear and bearing capacity more accurately leading to improved rating factors. Therefore, an alternative approach is provided at the end of the study in Section 8.4 where, residual shear capacity and bearing capacity can be calculated using the equations provided in Sections 8.1 and 8.2 and override the nominal capacity at the point of interest to as shown in Figure 8.4.

REFERENCES

AASHTO. (2020). *AASHTO LRFD bridge design specifications* (9th ed.). American Association of State Highway and Transportation Officials.

AISC. (2016, July 7). *AISC 360-16: Specification for structural steel buildings* (ANSI/AISC 360-16). American Institute of Steel Construction.

ASCE. (2021). *2021 report card for America's infrastructure*. American Society of Civil Engineers.

ASTM. (2022). *ASTM standard E8/E8M: Standard test methods for tension testing of metallic materials*. American Society for Testing and Materials International.

Gerasimidis, S., Breña, S., & Tzortzinis, G. (2021). *Improved load rating procedures for deteriorated steel beam ends with deteriorated stiffeners* (Report No. 21-024). Massachusetts Department of Transportation.

Javier, E. M., III., Hebdon, M. H., & Provines, J. T. (2021a, October). *Methods for evaluation of the remaining shear capacity in steel bridge beams with section losses attributable to corrosion damage* (Report No. FHWA/VTRC 22-R4). Virginia Transportation Research Council.

Javier, E. M., III. (2021b, October). *Methods for evaluation of the remaining shear strength in steel bridge beams with section losses due to corrosion damage* [Master's thesis, Virginia Tech].

Kayser, J. R. (1988). *The effects of corrosion on the reliability of steel girder bridges*. University of Michigan.

Kayser, J. R., & Nowak, A. S. (1989). Capacity loss due to corrosion in steel-girder bridges. *Journal of Structural Engineering*, *115*(6), 1525–1537.

Rahgozar, R. (2009). Remaining capacity assessment of corrosion damaged beams using minimum curves. *Journal of Constructional Steel Research*, *65*(2), 299–307.

Sugimoto, I., Kobayashi, Y., & Ichikawa, A. (2006). Durability evaluation based on buckling characteristics of corroded steel deck girders. *Quarterly Report of RTRI*, *47*(3), 150–155.

Tzortzinis, G. (2021). *A comprehensive protocol for inspection and assessment of aging steel bridges: Experiments, compu-*

tations, and 3D laser scanning of field corroded girders [Doctoral dissertation, University of Massachusetts Amherst].

Tzortzinis, G., Breña, S. F., & Gerasimidis, S. (2022). Experimental testing, computational analysis and analytical formulation for the remaining capacity assessment of bridge plate girders with naturally corroded ends. *Engineering Structures*, *252*, 113488.

Tzortzinis, G., Gerasimidis, S., Brena, S., & Knickle, B. (2019). *Development of load rating procedures for deteriorated steel beam ends: Deliverable 4* (Report No. 19-008). University of Massachusetts at Amherst.

Tzortzinis, G., Knickle, B. T., Bardow, A., Breña, S. F., & Gerasimidis, S. (2021a). Strength evaluation of deteriorated girder ends. I: Experimental study on naturally corroded I-beams. *Thin-Walled Structures*, *159*, 107220.

Tzortzinis, G., Knickle, B. T., Bardow, A., Breña, S. F., & Gerasimidis, S. (2021b). Strength evaluation of deteriorated girder ends. II: Numerical study on corroded I-beams. *Thin-Walled Structures*, *159*, 107216.

APPENDICES

Appendix A. Capacity Calculations for W24 × 68

APPENDIX A. CAPACITY CALCULATIONS FOR W24×68

Specimen #1

Calculations were conducted according to AISC-360-16.

1. Plastic shear capacity of W24x68:

$V_p := 0.6 \cdot F_y \cdot t_w \cdot d \cdot C_{v1} = 272\ kip$

$Plastic\_shear\_capacity\_Specimen\_1 := V_p = 272\ kip$

2. Web crippling capacity of unstiffened W24x68:

$$R_{WLC} := 0.4 \cdot \left(t_w^{\,2}\right) \cdot \left(1 + \left(4 \cdot \frac{l_b}{d} - 0.2\right) \cdot \left(\frac{t_w}{t_f}\right)^{1.5}\right) \cdot \sqrt{\frac{E \cdot F_y \cdot t_f}{t_w}} \cdot Q_f$$

$R_{WLC} = 159\ kip$

To prevent web crippling, a pair of full-depth transverse stiffeners were added at the support and at the loading point.

3. Plastic moment capacity of W24x68 with cover plate:

$M_p := F_y \cdot Z_x = 907\ kip \cdot ft$

$$Shear\_at\_flexural\_capacity\_Specimen\_1 := \frac{M_p}{a} = 302\ kip$$

Data from the Large-Scale test for Specimen #1:

$P := 292\ kip$ — maximum applied load

$$V_{p.test} := \frac{(P \cdot 220\ in)}{256\ in} = 251\ kip$$ — maximum shear force at the bearing during the test

$$reduction := \frac{(V_p - V_{p.test})}{V_p} = 8\%$$ — decrease in shear capacity

Specimen #3

Calculations were conducted according to AISC-360-16.

1. Plastic shear capacity of W24x68:

$V_p := 0.6 \cdot F_y \cdot t_w \cdot d \cdot C_{v1} = 301 \ kip$

$Plastic\_shear\_capacity\_Specimen\_3 := V_p = 301 \ kip$

2. Web crippling capacity of unstiffened W24x68:

$$R_{WLC} := 0.4 \cdot \left(t_w^{\ 2}\right) \cdot \left(1 + \left(4 \cdot \frac{l_b}{d} - 0.2\right) \cdot \left(\frac{t_w}{t_f}\right)^{1.5}\right) \cdot \sqrt{\frac{E \cdot F_y \cdot t_f}{t_w}} \cdot Q_f$$

$R_{WLC} = 168 \ kip$

To prevent web crippling a pair of full-depth transverse stiffeners were added at the support and at the loading point.

3. Plastic moment capacity of W24x68:

$M_p := F_y \cdot Z_x = 752 \ kip \cdot ft$

$$Shear\_at\_flexural\_capacity\_Specimen\_3 := \frac{M_p}{a} = 251 \ kip$$

Data from the Large-Scale test for Specimen #3:

$P := 275 \ kip$ — maximum applied load

$V_{p.test} := \frac{(P \cdot 220 \ in)}{256 \ in} = 236 \ kip$ — maximum shear force at the bearing during the test

$reduction := \frac{(V_p - V_{p.test})}{V_p} = 22\%$ — decrease in shear capacity

Specimen #4

Calculations were conducted according to AISC-360-16.

1. Plastic shear capacity of W24x68:

$V_p := 0.6 \cdot F_y \cdot t_w \cdot d \cdot C_{v1} = 301\ kip$

$Plastic\_shear\_capacity\_Specimen\_4 := V_p = 301\ kip$

2. Web crippling capacity of unstiffened W24x68:

$$R_{WLC} := 0.4 \cdot \left(t_w{}^2\right) \cdot \left(1 + \left(4 \cdot \frac{l_b}{d} - 0.2\right) \cdot \left(\frac{t_w}{t_f}\right)^{1.5}\right) \cdot \sqrt{\frac{E \cdot F_y \cdot t_f}{t_w}} \cdot Q_f$$

$R_{WLC} = 168\ kip$

3. Plastic moment capacity of W24x68:

$M_p := F_y \cdot Z_x = 752\ kip \cdot ft$

$$Shear\_at\_flexural\_capacity\_Specimen\_4 := \frac{M_p}{a} = 251\ kip$$

Data from the Large-Scale test for Specimen #4:

$P := 48\ kip$ — maximum applied load

$V_{p.test} := \frac{(P \cdot 220\ in)}{256\ in} = 41\ kip$ — maximum shear force at the bearing during the test

$reduction := \frac{(R_{WLC} - V_{p.test})}{R_{WLC}} = 75\%$ — decrease in bearing capacity

Specimen #5

Calculations were conducted according to AISC-360-16.

1. Plastic shear capacity of W24x68:

$V_p := 0.6 \cdot F_y \cdot t_w \cdot d \cdot C_{v1} = 272\ kip$

$Plastic\_shear\_capacity\_Specimen\_5 := V_{p1} = 272\ kip$

2. Web crippling capacity of unstiffened W24x68:

$$R_{WLC} := 0.4 \cdot \left(t_w{}^2\right) \cdot \left(1 + \left(4 \cdot \frac{l_b}{d} - 0.2\right) \cdot \left(\frac{t_w}{t_f}\right)^{1.5}\right) \cdot \sqrt{\frac{E \cdot F_y \cdot t_f}{t_w}} \cdot Q_f$$

$R_{WLC} = 159\ kip$

3. Plastic moment capacity of W24x68:

$M_p := F_y \cdot Z_x = 679\ kip \cdot ft$

$$Shear\_at\_flexural\_capacity\_Specimen\_5 := \frac{M_p}{a} = 226\ kip$$

Data from the Large-Scale test for Specimen #5:

$P := 25\ kip$ — maximum applied load

$V_{p.test} := \frac{(P \cdot 220\ in)}{256\ in} = 21\ kip$ — maximum shear force at the bearing during the test

$reduction := \frac{(R_{WLC} - V_{p.test})}{R_{WLC}} = 87\%$ — decrease in bearing capacity

Specimen #6

Calculations were conducted according to AISC-360-16.

1. Plastic shear capacity of W24x68:

$V_p := 0.6 \cdot F_y \cdot t_w \cdot d \cdot C_{v1} = 284\ kip$

$Plastic\_shear\_capacity\_Specimen\_6 := V_p = 284\ kip$

2. Web crippling capacity of unstiffened W24x68:

$$R_{WLC} := 0.4 \cdot \left(t_w^{\,2}\right) \cdot \left(1 + \left(4 \cdot \frac{l_b}{d} - 0.2\right) \cdot \left(\frac{t_w}{t_f}\right)^{1.5}\right) \cdot \sqrt{\frac{E \cdot F_y \cdot t_f}{t_w}} \cdot Q_f$$

$R_{WLC} = 163\ kip$

To prevent web crippling a pair of full-depth transverse stiffeners were added at the support and at the loading point.

3. Plastic moment capacity of W24x68:

$M_p := F_y \cdot Z_x = 708\ kip \cdot ft$

$$Shear\_at\_flexural\_capacity\_Specimen\_6 := \frac{M_p}{a} = 236\ kip$$

Data from the Large-Scale test for Specimen #6:

$P := 270\ kip$ — maximum applied load

$V_{p.test} := \frac{(P \cdot 220\ in)}{256\ in} = 232\ kip$ — maximum shear force at the bearing during the test

$reduction := \frac{(V_p - V_{p.test})}{V_p} = 18\%$ — decrease in shear capacity

Specimen #7

Calculations were conducted according to AISC-360-16.

1. Plastic shear capacity of W24x68:

$$V_p := 0.6 \cdot F_y \cdot t_w \cdot d \cdot C_{v1} = 284 \ kip$$

$$Plastic\_shear\_capacity\_Specimen\_7 := V_p = 284 \ kip$$

2. Web crippling capacity of unstiffened W24x68:

$$R_{WLC} := 0.8 \cdot \left(t_w{}^2\right) \cdot \left(1 + 3 \cdot \frac{l_b}{d} \cdot \left(\frac{t_w}{t_f}\right)^{1.5}\right) \cdot \sqrt{\frac{E \cdot F_y \cdot t_f}{t_w}} \cdot Q_f = 310 \ kip$$

$$R_{WLC} = 310 \ kip$$

3. Plastic moment capacity of W24x68:

$$M_p := F_y \cdot Z_x = 708 \ kip \cdot ft$$

$$Shear\_at\_flexural\_capacity\_Specimen\_7 := \frac{M_p}{a} = 101 \ kip$$

Data from the Large-Scale test for Specimen #7:

$P := 184 \ kip$ — maximum applied load

$V_{p.test} := \frac{(P \cdot 7 \ ft)}{14 \ ft} = 92 \ kip$ — maximum shear force at the bearing during the test

$$reduction := \frac{\left(\frac{M_p}{a} - V_{p.test}\right)}{\frac{M_p}{a}} = 9\%$$

decrease in flexural capacity

About the Joint Transportation Research Program (JTRP)

On March 11, 1937, the Indiana Legislature passed an act which authorized the Indiana State Highway Commission to cooperate with and assist Purdue University in developing the best methods of improving and maintaining the highways of the state and the respective counties thereof. That collaborative effort was called the Joint Highway Research Project (JHRP). In 1997 the collaborative venture was renamed as the Joint Transportation Research Program (JTRP) to reflect the state and national efforts to integrate the management and operation of various transportation modes.

The first studies of JHRP were concerned with Test Road No. 1—evaluation of the weathering characteristics of stabilized materials. After World War II, the JHRP program grew substantially and was regularly producing technical reports. Over 1,600 technical reports are now available, published as part of the JHRP and subsequently JTRP collaborative venture between Purdue University and what is now the Indiana Department of Transportation.

Free online access to all reports is provided through a unique collaboration between JTRP and Purdue Libraries. These are available at http://docs.lib.purdue.edu/jtrp.

Further information about JTRP and its current research program is available at http://www.purdue.edu/jtrp.

About This Report

An open access version of this publication is available online. See the URL in the citation below.

Kanakamedala, D., Seo, J., Varma, A. H., Connor, R. J., & Tarasova, A. (2023). *Shear and bearing capacity of corroded steel beam bridges and the effects on load rating* (Joint Transportation Research Program Publication No. FHWA/IN/JTRP-2023/11). West Lafayette, IN: Purdue University. https://doi.org/10.5703/1288284317634